DIRECT MONITORING OF METAL-CATALYZED REACTIONS USING ELECTROSPRAY IONIZATION MASS SPECTROMETRY

Thesis submitted at Charles University in Prague
in fulfillment of the requirements for
the PhD degree in Chemistry

by

Ing. Alexandra Tsybizova
Department of Organic Chemistry
Charles University in Prague, Faculty of Science

Supervisors: Dr. habil. Detlef Schröder; Prof. Mgr. Jana Roithová, Ph.D

Prague, October 2015

Contents

Frontispiece

"An original idea. That can't be too hard. The library must be full of them."

Stephen Fry

Declaration

The scientific work for the current thesis was performed at the Department of Physical-Organic Chemistry, Institute of Organic Chemistry and Biochemistry, AS CR, v.v.i., from January 2011 to March 2013. And from April 2013 to June 2015 at the Department of Organic Chemistry, Charles University in Prague.

I hereby declare that I have developed this thesis independently. All sentences or passages quoted in this project dissertation from other people's work have been specifically acknowledged by clear cross referencing to author, work and page(s). I understand that failure to do this amounts to plagiarism and will be considered grounds for failure in this module and the degree examination as a whole. While discussing the results in the current dissertation, self plagiarism was avoided to the maximum possible extend.

The current dissertation work has not been used for the acquisition of any other academic qualification.

Name: Alexandra Tsybizova

Signed:

Date:

Acknowledgment

The preparation of this dissertation thesis would not have been possible without the involvement of many people.

First I would like to warmly thank both of my supervisors - Dr. Detlef Schröder and Prof. Jana Roithová. Both of them provided a great source of inspiration and admiration for me. I am very grateful for the opportunity not only to learn and expand my knowledge, but also for the ability to test and freely share my ideas, even those that did not necessarily lead to the successful solutions. I would also like to thank Drs Schröder and Roithová for their unique ability to boost my optimism, at the most dark moments of my research, when it seemed that the project reached the dead end.

Loosing Detlef suddenly and unexpectedly on August 22, 2012 in the age of 49 was a great shock and tragedy for all who knew him. I believe that his untimely passing was a great loss to the scientific community as a whole, and I still terribly miss him, bursting with ideas, optimism and generosity.

Secondly, I want to thank my collaborators, who contributed to the projects discussed below: Tibor András Rokob and Lubomír Rulíšek for the theoretical calculations that were done for the Ni-PhPy project; Andrew Gray for his calculations for the C-H activation project; Bradford L. Ryland and Shannon S. Stahl for the EPR measurements for the $Cu(OAc)_2$ speciation; Adam Henke and Jiři Šrogl for the synthesis of related compounds and fruitful discussion during the investigation copper catalyzed aerobic cross coupling of thiol esters and arylboronic acids. The discussion of the obtained results would not have been complete without their contribution. I would also like to thank Anna Březinová for the GC-MS measurements of the purity of the phenylpyridine samples for the Ni-PhPy project.

Thirdly, many thanks to my former and current group mates: Christopher Shaffer, Divya Agrawal, Ágnes Rokobné Révész, Ján Tarábek, Anton Škríba, Jakub Hývl and

many others from both Detlef's and Jana's group for the constant readiness to help, and a friendly atmosphere. Andrew Gray I cannot only praise as an excellent research partner, being ready to test all of my crazy ideas, but also as a good friend with whom I am happy to co-author a research paper. I would also like to thank him for reading the current dissertation, as well as his valuable comments during its preparation. Special thanks to Eric Andris, whose awesome Python programs made the extraction of the data from spectra series (CID, kinetics) a lot more easier and less time consuming.

I would also like to thank my family and especially my husband for the constant support and belief in my abilities.

Last, but not least, I am grateful for the financial support provided from the following organizations and facilities:

- Academy of Sciences of the Czech Republic (RVO 61388963)
- the European Research Council (AdG HORIZOMS)
- the Grant Agency of the Czech Republic (207/11/0338, 207/12/0846 and No. 14-20077S)
- The results from CLIO were obtained with funding from the European Union´s Seventh Framework Programme (FP7/2007-2013) under the grant agreement No. 226716. CLIO staff, particularly Philippe Maître and Vincent Steinmetz, are acknowledged for their help and assistance

Abstract

The current dissertation thesis is focused on the investigation of metal-catalyzed reactions using electrospray ionization mass spectrometry as the primary research technique. However, other gas-phase methods such as tandem mass spectrometry, infrared multiphoton dissociation spectroscopy and quantum chemical calculations have also been involved to unravel and support the findings and proposals. As organometallic chemistry is a very broad and complicated topic, this thesis is only focused on a few projects. The first of them is dedicated to copper acetate speciation in organic solvents, the second - to the mechanistic investigation of copper catalyzed aerobic cross coupling of thiol esters and arylboronic acids, the third project studied coordination and bond activation of nickel(II) - phenylpyridine complexes and carboxylate assisted C-H activation reactions were investigated last.

Předkládaná dizertační práce je zaměřena na studium reakcí katalyzovaných kovy s použitím hmotnostní spektrometrie spojené s elektrosprejovou ionizací představující základní metodu výzkumu. Nicméně další metody jako tandemová hmotnostní spektrometrie, infračervená multifotonová disociační spektroskopie a kvantově chemické výpočty byly použity pro dořešení a podporu výsledků a návrhů. Organokovová chemie zahrnuje širokou škálu často velmi komplikovaných témat, tato práce je zaměřena na řešení pouze několika z nich. První část dizertační práce se věnuje studiu chování acetátu mědi v organických rozpouštědlech, druhá výzkumu mědí katalyzovaného aerobního cross couplingu thiolesterů a arylboronových kyselin, třetí studiu koordinace a vazebné aktivace nikl(II) - fenylpyridiniových komplexů a poslední výzkumu karboxylátem asistované C-H aktivace.

Parts of the results of this thesis have been published in:

- A. Tsybizova, B. L. Ryland, N. Tsierkezos, S. S. Stahl, J. Roithová, D. Schröder, *Speciation Behavior of Copper(II) Acetate in Simple Organic Solvents – Revealing the Effect of Trace Water*, Eur. J. Inorg. Chem., **2014**, 1407 - 1412.

- A. Tsybizova, D. Schröder, J. Roithová, A. Henke, J. Šrogl, *Gas-phase studies of copper catalyzed aerobic cross coupling of thiol esters and arylboronic acids*, J. Phys. Org. Chem., **2014**, 27, 198 – 203.

- A. Tsybizova, L. Rulíšek, D. Schröder, T. A. Rokob, *Coordination and Bond Activation in Complexes of Regioisomeric Phenylpyridines with the Nickel(II) Chloride Cation in the Gas Phase*, J. Phys. Chem. A., **2012**, 117, 1171 - 1180.

- A. Gray, A. Tsybizova, J. Roithová, *Carboxylate-Assisted C-H Activation of Phenylpyridines with Copper, Palladium and Ruthenium: A Mass Spectrometry and DFT Study*, Chem. Sci., **2015**, doi: 10.1039/C5SC01729G.

Chapter 1

Literature overview and aims of the present work

1.1 Metal catalysis in contemporary organic synthesis

The discovery of cross-coupling reactions has brought about the breakthrough of organometallic chemistry, which was recently acknowledged by award of the Nobel Prize in Chemistry (2010)[1–4]. These reactions have dramatically changed the synthetic approach to produce many natural compounds, supramolecular materials or polymers, and many well-known organic molecules; in the past their synthesis required many more steps than nowadays[5].

Therefore the mechanistic investigation of metal-catalyzed reactions has become a "hot topic" in contemporary physical organic chemistry, as their mechanisms greatly differ from what is considered as classical mechanistic schemes (*e.g.* Ad_E or S_N2). The first difference is the presence of the catalytic cycle and recovery of the metal catalyst. The second is the formation of organometallic complexes that are sometimes difficult to characterize and study. Many of them are unstable at standard conditions and require careful handling (*e.g.* under an atmosphere of inert gas). The situation is also complicated by the constant growth of various catalytic species that may behave differently in the catalytic cycle.

The rational design of catalytic complexes represents a popular challenge as many catalytic species are difficult and expensive to synthesize. Such design allows evaluation of the possible properties and estimation of catalytic activity[6].

1.2 Reaction mixture monitoring and ESI-MS

Reaction mixture monitoring is widely used for mechanistic investigations of new reactions. It has a wide potential allowing for kinetic studies, establishment of reaction end points and modification of the synthetic procedure (improve yields, reduce catalyst loading and by-product formation, make the reaction more environmentally friendly, *etc.*). Among many available techniques nuclear magnetic resonance spectroscopy, infrared spectroscopy and mass spectrometry are used frequently.

Electrospray ionization mass spectrometry (ESI-MS) is very popular for reaction monitoring. An ideal reaction for ESI-MS studies would proceed at room temperature, in a polar volatile solvent (*e.g.* acetonitrile, methanol, or water), in ambient atmosphere and would contain ionic reaction intermediates for easy detection and characterization. Organometallic reactions commonly fulfill most of these requirements and therefore are popular for investigations with ESI-MS. ESI is also a soft method for ion transfer from solution to the gas phase[7–9], and has been called the "major tool for the investigation of reaction mechanisms"[10–12]. Moreover, mass spectrometry allows for the advantageous investigation of both the intermediates properties in greater detail, and the thermodynamic and kinetic properties of elemental reaction steps[13,14].

In principle, there are two ways to investigate a reaction mixture using mass spectrometry: on-line and off-line monitoring. Off-line monitoring indicates that the reaction mechanism is being investigated in many steps, requiring the analysis of various differently prepared mixtures (with different amounts, concentrations or numbers of reagents in the mixture, as well as the use of different solvents). These condition changes, ideally, allow for the generation of different reaction intermediates that can be characterized by tandem mass spectrometry.

On the other hand, an on-line approach requires the determination of reaction mixture composition over time, and can be done either by repetitive sampling from an investigated reaction mixture at fixed time intervals, or by the direct connection of a reactor to the ionization source. The latter option can be achieved under atmospheric pressure[15,16] (see Figure 1.1a), and also using a glovebox - to maintain special reaction conditions (see Figure 1.1b)[17]. It should be kept in mind that continuous flow monitoring methods are not suitable for heterogeneous reactions, because they can cause capillary blockage and lead to signal loss. On the other hand, repetitive sampling from the reaction mixture allows

these difficulties to be overcome[18]. The combination of recently developed paper-spray ionization with MS is also worth mentioning as it provides a convenient way for on-line monitoring[19, 20].

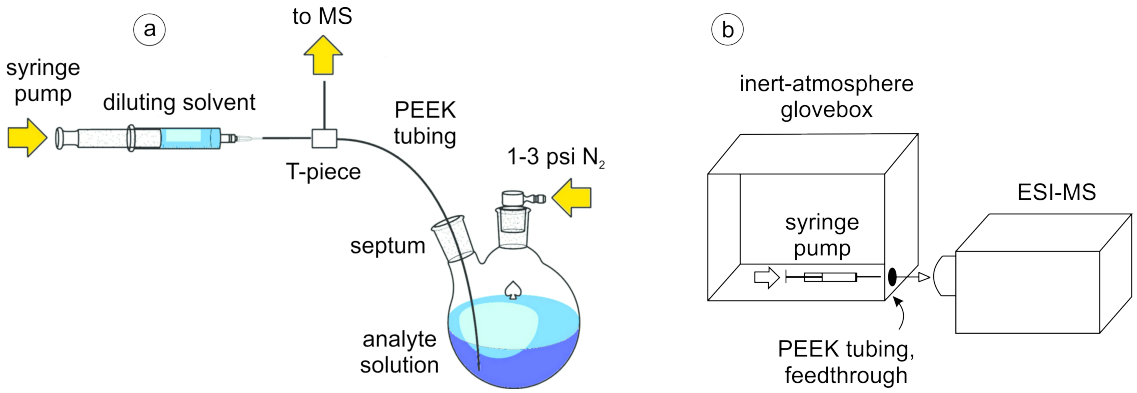

Figure 1.1: a) Continuous pressurized sample infusion set-up with on-line sample dilution *via* a syringe pump (reprinted from [16], copyright (2012) with permission from Elsevier); b) inert-atmosphere glovebox situated next to the ESI mass spectrometer. Syringe pump for sample infusion is located inside the glovebox; the PEEK tubing passes through a standard glovebox feedthrough sealed with O-rings. Adapted from ref. [17].

1.3 ESI-MS as a tool for mechanistic investigations and catalysis research

There are many approaches for the gas-phase analysis of a catalytic reaction[21]. ESI-MS investigation of metal-catalyzed reactions is often facilitated by the formation of metal intermediates that are either charged or can easily be charged during the catalytic course. However, the identification of active catalytic species in the reaction mixture is always a challenging task as mechanistic considerations can often predict the presence of several active species. Moreover, as was demonstrated by Halpern[22], the most abundant complex in solution does not necessarily need to participate in the catalytic cycle, and might, in fact, represent a dead end. However, ESI-MS can help to recognize activity levels of various detected species, selectively "fish out" important intermediates, isolate them in the gas phase and subject them to more detailed investigation.

"Fishing" for reactive intermediates was first elegantly introduced by C. Adlhart and P. Chen in 2000 in their publication devoted to the investigation of ring-opening metathesis polymerization (ROMP)[23]. To this end, Adlhart and Chen applied ESI-MS on-line monitoring of a reaction mixture, containing norbornene and a neutral methathesis catalyst

$(Cy_3P)_2Cl_2Ru{=}CHPh$, and introduced charged-tagged norbornens (see Scheme 1.1) for easier detection of reacting intermediates. These steps allowed the ROMP process to be followed up to oligomers with $n > 30$.

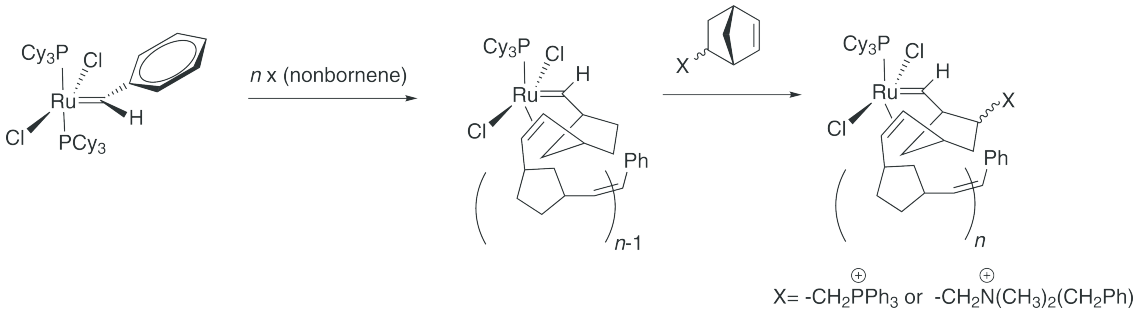

Scheme 1.1: Ring-opening metathesis polymerization (ROMP), catalyzed by the neutral complex $(Cy_3P)_2Cl_2Ru{=}CHPh$ (Cy = cyclohexyl) *via* a monophosphine active complex.

Introduction of a charged tag has become an important tool for ESI-MS investigations[24–38]. As ESI-MS preferentially samples ionic species, the components in the reaction mixture that are not easily chargeable (*e.g.* by protonation) might escape detection. Therefore a remote group bearing a charge (for example, trimethylamonium or a sulphonic group) can be artificially introduced to either substrate or catalyst molecule[39,40]. It is very important that the "tag" stays unchanged during the reaction and does not influence its course. Moreover, the use of a charged molecule only as a co-substrate (as shown by Adlhart and Chen) can be beneficial as adding charge to the major reactant may result in formation of multiply charged species thus complicating the analysis. Another simple method of forced ionization is the addition of traces of alkali salts to the samples, which leads to the formation of corresponding alkali cation adducts[41].

An example of the successful incorporation of a charged tag to a catalyst molecule was demonstrated in 2010 by Vikse *et al.,* whose studies were focused on the investigation of the Sonogashira cross coupling reaction[40]. In contrast to the previous studies, the introduction of an anionic phosphine ligand enabled investigation of the reaction in negative ion mode and detection of anionic reaction intermediates (Scheme 1.2). This method, developed in McIndoe's group, also allows organometallic compounds sensitive to air and hydrolysis to be studied by ESI-MS as the mass spectrometer is connected directly to glovebox[17].

Recently, another group have successfully applied ESI-MS for the investigation of such fragile metallic compounds as organocuprates[42].

Advanced tools in mass spectrometry bring additional prospects for mechanistic investigations in the gas phase. Thus, ESI-MS coupled to tandem mass spectrometry not

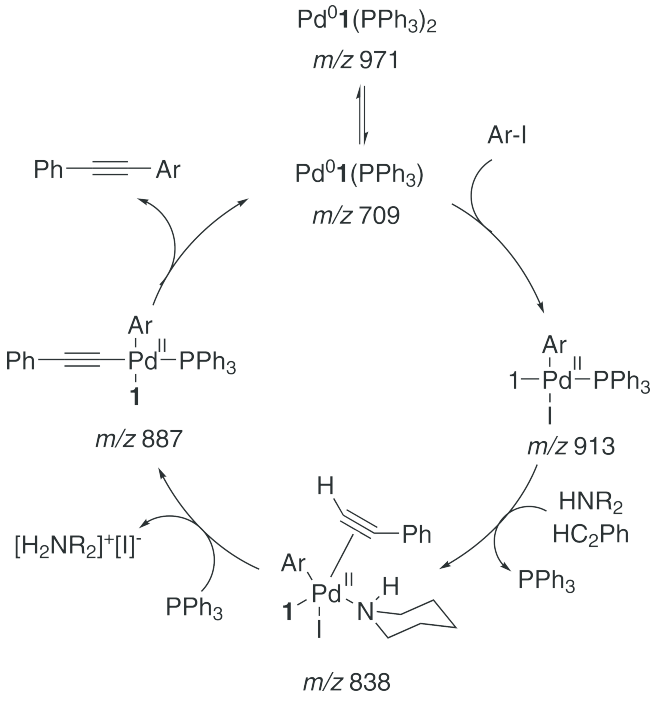

Scheme 1.2: Mechanistic scheme showing intermediates directly observed by negative ion mode ESI-MS. **1** represents negatively charged phosphine ligand: $[PPh_2(m\text{-}C_6H_4SO_3)]^-$.

only provides structural information, but also allows for the reactivity investigation of the mass-selected species *via* ion-molecule reactions in a collision cell. This can eliminate solution-phase effects from the solvent, counterions or pH[43, 44].

For example, in recent studies on the mechanism of a cobalt-catalyzed Diels-Alder reaction, Fiebig and co-workers investigated intermediates using tandem mass spectrometry[45]. In brief, it was shown that the catalyst $CoBr_2$(dppe) is reduced *in situ* by Zn/ZnI_2 to form the reactive catalytic cobalt(I) species $[Co(dppe)]^+$. The reactivity of these species with isoprene and phenylacetylene was further tested in the collision cell. It was shown that the central solution-phase intermediate $[Co(dppe)(isoprene)(phenylacetylene)]^+$ could also be generated in the collision cell *via* ion-molecule reactions. CID of $[Co(dppe)(isoprene)(phenylacetylene)]^+$ showed the elimination of a product molecule and thus the occurrence of a collision induced Diels-Alder reaction (Scheme 1.3).

Particularly remarkable is the progress achieved in the spectroscopy of gaseous ions, especially infrared multiphoton dissociation (IRMPD) spectroscopy[46–51] . As a representative example, Scheme 1.4 shows the mechanism of naphthol coupling as revealed by the combination of ESI-MS, and tandem mass spectrometry[52, 53]. Two intermediate complexes assigned as $[(\mathbf{1}\text{-H})Cu(TMEDA)]^+$ and $[(\mathbf{1}\text{-H})_2Cu_2Cl(TMEDA)_2]^+$ were revealed by ESI-MS and subjected to further analysis. Previous studies on the same reaction suggested

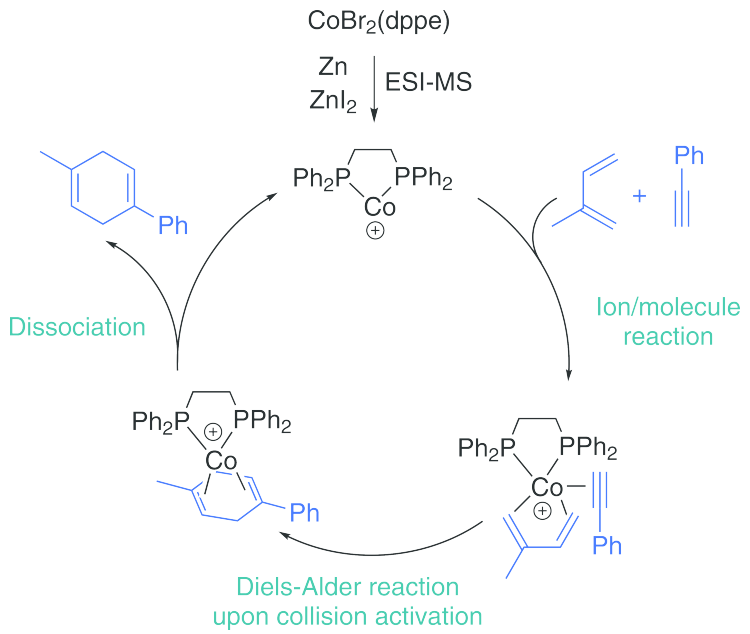

Scheme 1.3: Cobalt-catalyzed Diels–Alder reaction of phenylacetylene and isoprene.

that mononuclear species were the key intermediates in the catalytic cycle. Behaving as carbon-centered radicals these intermediates could couple to the second naphthol molecule to yield binol **2**. Accordingly, the reactivity of the observed mononuclear complex [(**1**-H)Cu(TMEDA)]$^+$ was tested in the collision cell with CH_3–S–S–CH_3 and CH_3–Se–Se–CH_3. If [(**1**-H)Cu(TMEDA)]$^+$ behaved as a C-centered radical, homogeneous cleavage of the S-S or Se-Se bond would be expected, however no reaction was observed. Therefore, the [(**1**-H)Cu(TMEDA)]$^+$ complex would not be capable of reacting with a second naphtole molecule.

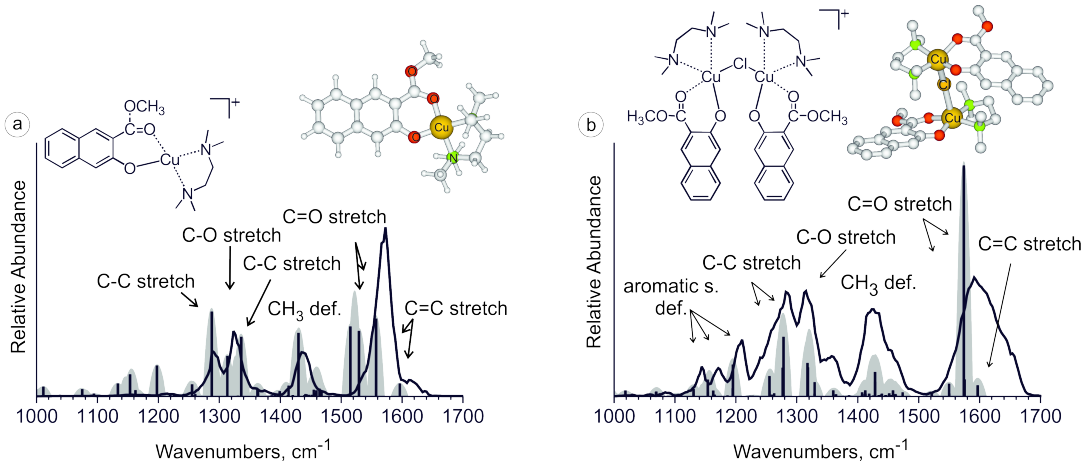

Figure 1.2: IRMPD spectra (black lines) of a) [(**1**-H)Cu(TMEDA)]$^+$ and b) [(**1**-H)$_2$Cu$_2$Cl(TMEDA)$_2$]$^+$ compared with the theoretical IR spectra (black bars and gray areas). Adapted from ref. [53].

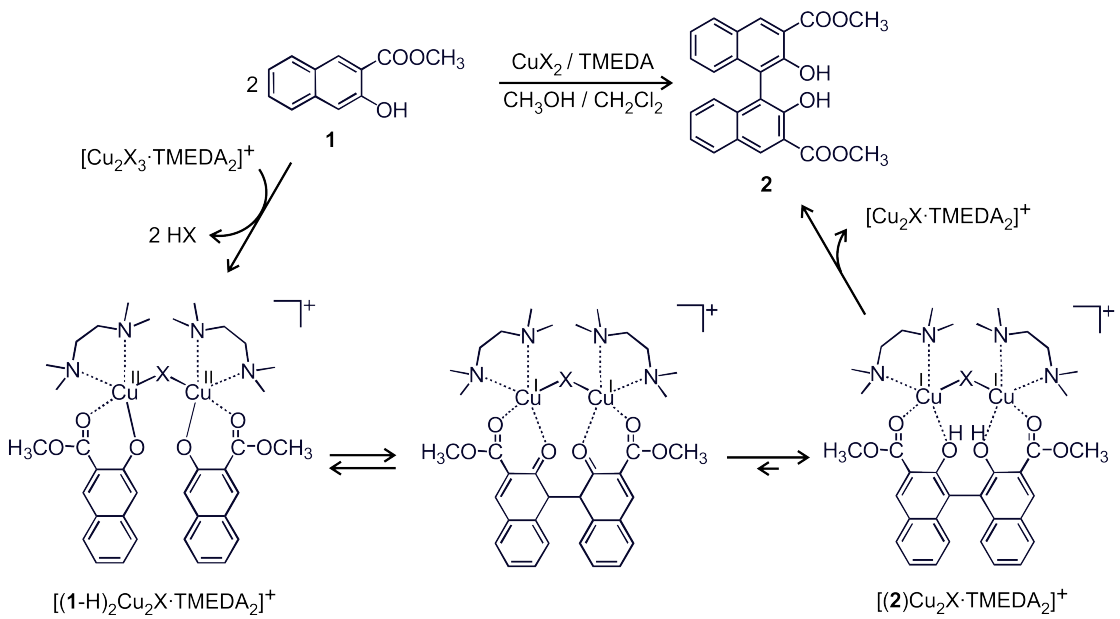

Scheme 1.4: Mechanism of naphthol coupling mediated by a binuclear copper complex, where X stands for a counterion ($X = NO_3^-$, Cl^-, or Br^-). Adapted according to ref. [52].

The [(**1**-H)Cu(TMEDA)]$^+$cation structure was also checked by IRMPD spectroscopy[53]. Figure 1.2a shows the comparison of the experimental IRMPD spectrum and the theoretical IR spectrum of the most stable structure found for the corresponding complex. Careful analysis of the experimental bands revealed that the unpaired electron is localized at the copper(II) center and therefore the structure cannot represent a C-radical. These observations suggested that that the [(**1**-H)Cu(TMEDA)]$^+$ complex would not react with a second inactivated naphthol molecule to yield the binol **2**.

Therefore the investigation turned to the binuclear complex [(**1**-H)$_2$Cu$_2$Cl(TMEDA)$_2$]$^+$ as the potential key reaction intermediate. CID experiments on this complex revealed three fragmentation channels: i) dissociation into complexes [(**1**-H)Cu(TMEDA)]$^+$ and [(**1**-H)CuCl(TMEDA)]$^+$, ii) loss of the TMEDA ligand and iii) the elimination of the binol **2**. IRMPD studies on the complex [(**1**-H)$_2$Cu$_2$Cl(TMEDA)$_2$]$^+$ (Figure 1.2b) revealed that it contains two naphthoxo ligands, separated from each other. Therefore, elimination of binol **2** is a sign of a C-C coupling reaction that can be induced by collisional activation.

On the other hand, it is a well-known fact that sometimes complexes detected by ESI-MS represent artifacts and not species generated in solution[54]. Therefore, identification of species relevant to the solution phase catalysis is an important and challenging task. In 2012 Roithova *et al.* accounted for this correlation in the studies of gold(I)-mediated addition of methanol to alkynes (see Scheme 1.5)[55].

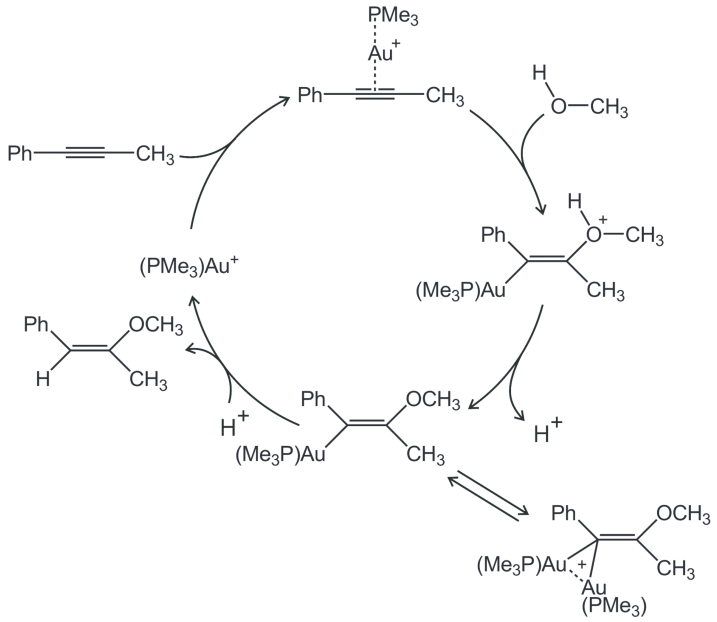

Scheme 1.5: The mechanism of methanol addition to alkynes, catalyzed by gold (I).

To this end, a reaction mixture containing 1-phenylpropyne and $AuCl(PMe_3)$ was investigated. ESI-MS revealed the formation of $[(PMe_3)_2Au_2(OCH_3)(PhCCMe)]^+$ cation (**X**) which could correspond to a possible intermediate (see Figure 1.3a). In order to prove the relevance of ion **X** to the condensed phase chemistry, the behavior of this ion was investigated in experiments with CD_3OD. Thus, 1-phenylpropyne was mixed with $AuCl(PMe_3)$ in CD_3OD, kept for one hour, diluted to a double volume by CH_3OH and immediately sprayed to the mass spectrometer. The spectra recorded at the very beginning of the experiment showed dominant abundance of the $[D_3]$-**X** complex, whereas after 20 minutes the statistically expected 1:1 ratio of the unlabeled **X** and the labeled $[D_3]$-**X** complexes was established (Figure 1.3).

The mass spectrum in Figure 1.3 also shows the generation of species **Y** (m/z 421) at minor abundances which corresponds to a complex between a (trimethylphosphino)gold cation and the product of methanol addition to 1-phenylpropyne. Thus intermediate **X** could formally be related to **Y** by replacement of H by $AuPMe_3$. Likewise, in the experiments with CD_3OD, only the fully deuterated version of **Y** was observed in the beginning (Figure 1.3c).

Therefore, the labeling experiments demonstrated that the ions **X** and **Y** are formed in the solution and thus are not ESI-MS artifacts. The experiment also allowed determination of the half-life of **X**, which was about 3.7 minutes at 25 °C in the reaction solution.

Subsequent IRMPD and DFT studies on the $[(PMe_3)_2Au_2(OCH_3)(PhCCMe)]^+$ cation

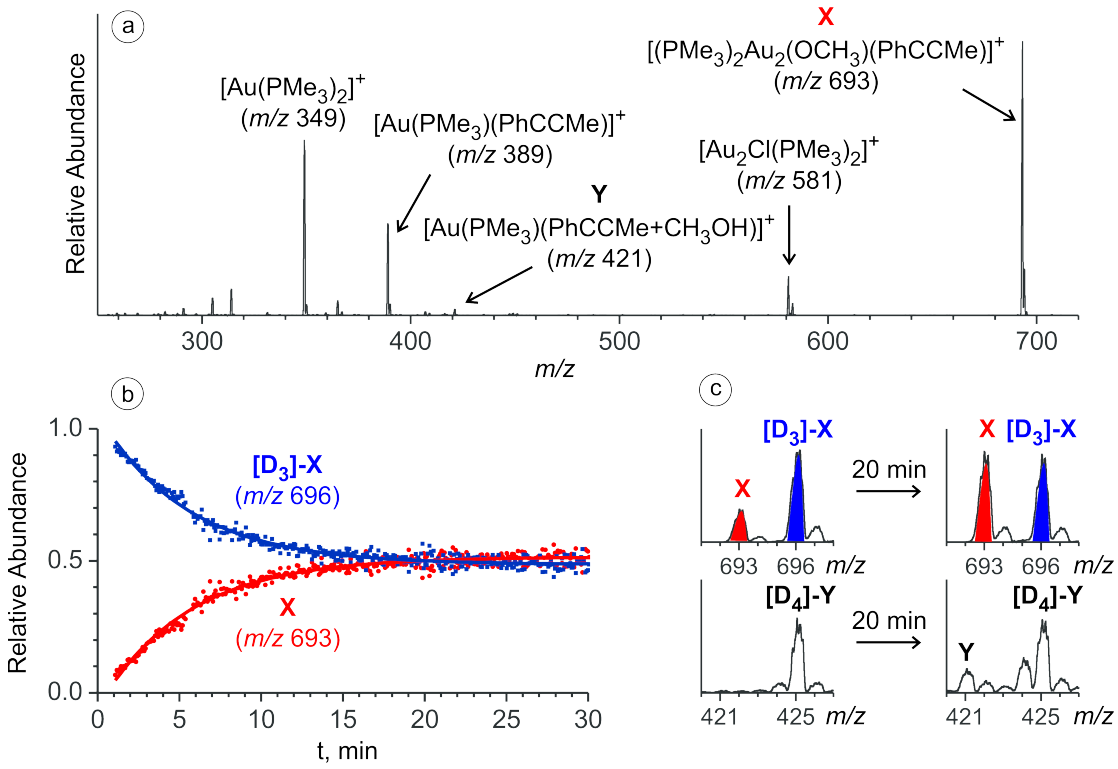

Figure 1.3: a) ESI-MS spectrum of a MeOH solution of 1-phenylpropyne with a gold catalyst. b) Time dependence of the relative abundances of $[D_3]$-**X** and **X** upon adding CH_3OH to a solution of 1-phenylpropyne in CD_3OD and the catalyst after 1 hour reaction time. c) The averaged spectra sections in the beginning and in the end of the experiment. The figure is adapted from ref. [55].

helped to reveal its structure and account for the reaction mechanism (Scheme 1.5) as well as the role of the diaurated complex.

1.4 Links between ESI-MS and solution

Nowadays, as more and more scientists use ESI-MS for the analysis of various reaction mixtures, the general question of whether the obtained mass spectrum has any correlation to the composition of an investigated solution is being passionately debated. The very first question that every solution chemist would have in mind is whether ESI-MS can, in fact, characterize, or at least predict solution properties[21,56,57]. Recently, an example fully illustrating this skepticism was published in Organometallics[58–60]. The discussion was concentrated on the mechanism of C-H bond activation of benzene catalyzed by Pt(II) diimine complexes.

It has been argued that either ESI-MS has a direct correlation, or no correlation at all.

In fact, neither extreme appears to be correct[61,62]. However, while interpreting the ESI-MS results it is very important to recognize the major changes occurring during transfer from solution to the gas phase and account for them.

First of all, changes in concentration, pH, solvation, *etc.* occur during ESI-MS, and an important factor is how a system would respond to these changes[63,64]. Secondly, ESI-MS samples charged species and therefore neutral compounds from the reaction mixture can only be detected if they undergo ionization (*e.g.* deprotonation or protonation, formation of alkali cation adducts, *etc.*, see examples in Section 1.3). Although this fact does not pose problems in detection of various species, especially after the introduction of charged tags, their sampling does not occur in a 1:1 ratio. In fact, the detection of neutral substrates can be discriminated by other ionic species existing in solution[65]. Similar discrimination effect can occur for different neutral substrates while being ionized. Thirdly, the resulting mass spectra can be substantially affected by electrochemical processes in ESI and the ionization conditions[66–68]. In addition, gas-phase reactions are often driven by systems with a limited (or even absent) solvation of the reactive centers. Therefore, these reactions might be irrelevant to the solution-phase equilibrium and even may not occur in solution[69–71].

The question of whether ESI-MS samples solution structures has been addressed by recent studies on *p*-hydroxybenzoic acid by a number of laboratories[72–75]. In solution, *p*-hydroxybenzoic acid is well-known to be deprotonated at the acid, whereas deprotonation of the phenol group is preferred in the gas phase (see Scheme 1.6)[76].

Thus, Tian and Kass showed a pronounced effect of the solvent on the resulting structure of the *p*-hydroxybenzoic acid anion observed with ESI-MS[72]. The study concluded that protic solvents allow tautomerization to the more stable gas-phase phenoxide structure while aprotic solvents preserve the solution structure, i.e. the carboxylate tautomer.

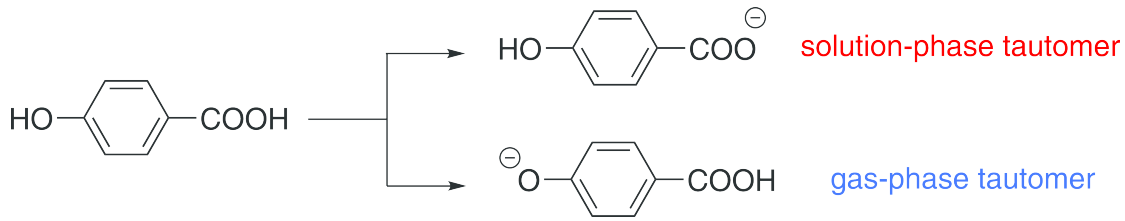

Scheme 1.6: Different tautomers of deprotonated *p*-hydroxybenzoic acid.

On the other hand, Steill and Oomens[73] recorded IRMPD spectra of *p*-hydroxybenzoic acid anions generated from protic and aprotic solvents, and confirmed the effect that solvent had on tautomer formation. However their assignment of the resulting anions was opposite

to that of Tian and Kass.

An explanation for this apparent controversy was found by Schröder *et al.*[75]. They used NMR to show that in both aprotic and protic solvents the carboxylate anion is formed. On the other hand, in the gas phase both tautomers exist and their distribution depends on the solvent used during ESI-MS experiments. Ion mobility mass spectrometry experiments allowed separation of the two tautomers. During the experiments with *p*-hydroxybenzoic acid dissolved in pure D_2O, H/D exchange was observed due to background H_2O present in the IMS cell. The H/D exchange was found to be more pronounced for the phenoxide tautomer than that of the carboxylate tautomer. Therefore the different populations of the two tautomers observed during ESI-MS experiments is the result of reversible protonation/deprotonation steps taking place within the ESI source. This can occur in a protic solvent (methanol, water) whereas this option does not exist for aprotic acetinotrile.

It is thus important for both gas-phase and synthetic chemists to work in parallel, in order to provide a unified view of the investigated problem. Thus, combination with different methods (infrared spectroscopy, NMR spectroscopy, crystallography, *etc.*) is often required for the full interpretation of ESI-MS results, providing a good base for the establishment of the reaction mechanism.

1.5 Aims and objectives of the current work

At present, mechanistic understanding of organometallic reactions is far from complete. Development of efficient on-line monitoring techniques for organometallic reactions is important. Ideally these techniques should provide rapid and accurate analysis of a reaction mixture, detection of reactive intermediates, and determination of kinetic data that are useful for fundamental mechanistic investigations as well as synthesis optimization and other areas of research.

The aim of the current dissertation work was the investigation of metal catalyzed reaction mechanisms with ESI-MS using suitable reaction monitoring methods. Therefore, several projects devoted to the investigation of different reactions and catalyst speciation were carried out.

As a pilot project, speciation of $Cu(OAc)_2$ in different organic solvents was studied under various conditions. Following that, a coupling reaction catalyzed by copper acetate

was investigated and monitored on-line, with a characterization of detected intermediates using tandem mass spectrometry.

As ion mobility mass spectrometry represents yet another dimension to gain structural and mechanistic information, the investigation of various Ni-PhPy complexes was performed.

Last, a carboxylate assisted C-H activation was studied. To this end, the metal complexes with to-be-activated substrate where C-H activation would proceed by the loss of acetic acid were generated. This enabled us to demonstrate an experimental proof of the C-H activation step, and by a combination of the IRMPD experiments with other mass-spectrometric techniques (energy resolved collision induced dissociation), we were able to determine the energy barriers for C-H activation.

Chapter 2

Methods and instrumentation

This dissertation covers research that was done using a wide range of techniques, both experimental and theoretical. Existing literature provides a great depth of information, regarding these methods[11,50,77–83]. Therefore, this chapter will only briefly summarize the most important aspects.

2.1 Electrospray ionization

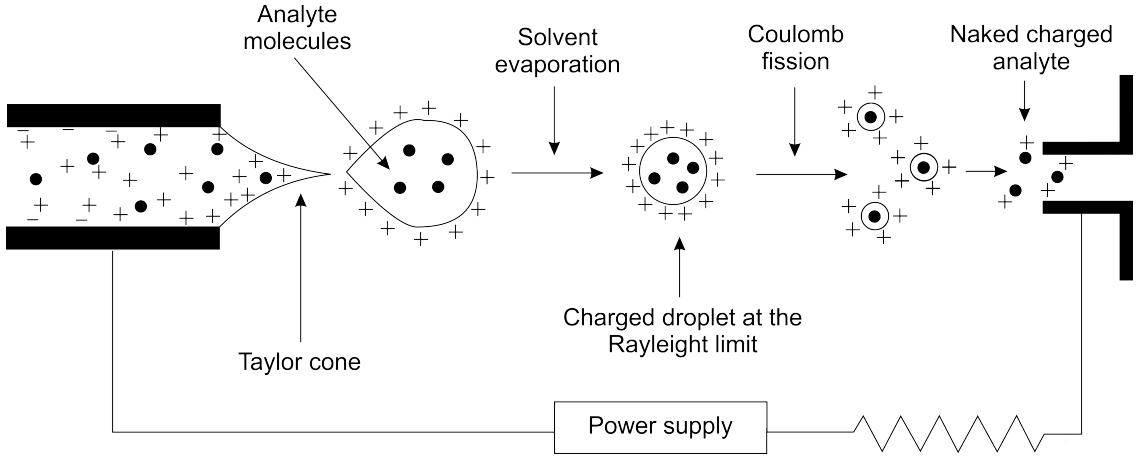

Figure 2.1: Schematic representation of the CRM for the ESI process. Adapted from ref. [84].

Electrospray ionization (ESI) is probably the most widely used ionization method in mass spectrometry[83]. Since its introduction by Fenn[7,9] in 1984, its use has grown rapidly, especially for the analysis of macromolecules that do not usually survive hard ionization conditions. There are two major theories that explain ion formation during ESI: the ion evaporation model (IEM) and the charge residue model (CRM).

In the CRM the process of ion formation can be divided into 3 major steps (Figure 2.1): i) formation of charged droplets (aerosol) from the solution exiting of the electrospray capillary, ii) shrinkage of the charged droplets due to the solvent evaporation, and finally iii) release of the naked ions into the gas phase. The investigated solution is transferred to the electrospray capillary, which has a high voltage (usually 3–5 kV) applied to it. At the edge of the capillary tip the liquid becomes charged and forms a cone shape (Taylor cone). The droplets then burst away from each other, creating a highly charged aerosol. Then, charged droplets are led into the evaporation chamber, where the solvent from the droplets is evaporated with assistance of a gas (usually nitrogen). When charges are pushed close together they repel each other (Coulombic repulsion) dividing the droplets into smaller pieces. The process of the gradual shrinking/repulsion is repeated until the point when no solvent is left.

The major difference of the IEM when compared with the CRM is that the final ion is produced by desorption rather than by solvent evaporation from the droplet[85,86]. There is evidence that smaller ions prefer to be delivered to the gas phase by the ion evaporation model, while larger ions as, for example, proteins, are liberated by the charge residue model[86–88].

It should be taken into the account that ESI conditions can dramatically affect the speciation of the investigated mixture. Thus, typical ESI-MS operational conditions that were optimized for the investigation of large multiply charged biomolecules are of limited use for organometallic complexes. An example of such an effect was shown by Schröder *et al.* in studies of $[Cu(urea)]^+$ complexes[89]. At low capillary voltages the multimeric clusters were preferred, whereas high voltages caused cluster breakage (so-called source fragmentation) leading to the formation of monomers.

2.2 Collision induced dissociation

2.2.1 Basic principles

Collision induced dissociation (CID) is a mass spectrometry technique that induces fragmentation of molecular ions in the gas phase. Conventionally, the ions are accelerated by some electrical potential to increase their kinetic energy and then allowed to collide with molecules of a noble gas (often helium, argon or xenon). During the collision process some of the kinetic energy is converted into internal energy which can result in bond breakage

and the fragmentation of the molecular ion into smaller fragments. These fragment ions can then be analyzed by tandem mass spectrometry.

The process of CID under single-collision conditions can be explained by the Lindemann-Hinshelwood mechanism shown in equations 2.1–2.2[90,91].

$$(AB^+) + N \rightleftharpoons (AB^+) * + N \tag{2.1}$$

$$(AB^+) * \rightarrow A^+ + B \tag{2.2}$$

In the first step the parent ion (AB^+) undergoes a collision with a noble gas (N) and becomes energetically excited. In the second step, the excited ion (AB^+)* dissociates into charged and neutral fragments. For the majority of dissociation pathways, the dissociation reaction is intrinsically endothermic as there is no activation barrier for the reverse process. The threshold energy, also called appearance energy (AE), can be converted into a bond dissociation energy (BDE).

Measurements of energy-resolved CID cross-sections are widely used for the extraction of the threshold energy and have been originally employed for small ions[92]. Later, the method was extended for larger organometallic complexes involved in homogeneous catalysis[93–97].

Pioneering work in modeling energy-resolved CID curves was done by P. Armentrout and co-workers that resulted in creation of the CRUNCH program[98]. Although CRUNCH allows very accurate values to be obtained for the threshold energy, and is considered as "the current state-of-the-art in deconvolution of energy-resolved CID cross sections"[99], it requires the vibrational frequencies for the reactant ion as well as those for the transition state to be calculated. This makes the estimation of threshold energies a rather complicated and time-consuming process.

As an alternative to CRUNCH that can be used on larger organometallic complexes, Chen *et al.* developed the L-CID approach[99]. In comparison to CRUNCH, L-CID is easier to use as it substitutes the set of initial vibrational rotational parameters with an effective frequency thus reducing the amount of input parameters.

Although accurate thermochemical data are important for the investigation of gas-phase reactions and explanation of their mechanisms, special equipment is required for their collection, applicable for use with either L-CID or CRUNCH[99,100]. When less accurate ex-

perimental data are treated with either L-CID or CRUNCH programs, only qualitative conclusions can be drawn. Therefore, in the current dissertation thesis, a phenomenological approach developed in Schröder's group was used for the determination of activation energies (see Section 2.3)[101]. This method also allows for qualitative comparison of the obtained energies, however is is much simpler in terms of both experimental setup and the treatment the obtained data.

2.2.2 Thermodynamic *vs.* kinetic control in CID

As shown in Section 2.2.1, CID experiments can provide accurate bond dissociation and/or activation energies, however the data will strongly depend on whether thermodynamic or kinetic control is operative[102,103].

The question of which type of control is present can be addressed by estimation of the activation entropy ($\triangle S^{\ddagger}$) for the activated parent ion ($(AB^{+})^{*}$)[104]. Thus, a fairly positive $\triangle S^{\ddagger}$ indicates that ion dissociation occurs *via* a so-called "loose" transition state. This is the case for the majority of gas-phase reactions and is represented by simple bond cleavage with a monotonically rising energy profile (see Figure 2.2a) . On the other hand, the transition state for rearrangement reactions requiring formation of new bonds is "tight", with a much lover value of $\triangle S^{\ddagger}$ compared to that for dissociation. Therefore, fragmentation, occurring *via* a tight transition state is thermostatically favored, but needs a longer time to proceed, whereas simple dissociation processes are quicker. Thus, the appearance (or threshold) energy obtained from the experiment is always the highest energy along the reaction coordinate for simple dissociation, and describes the actual activation barrier in the case of a tight transition state. In general, simple bond cleavages tend to have higher activation energy thresholds than rearrangements, where bond formation in the transition state decreases the energetic cost of a simultaneous bond rupture.

However, while considering the thermodynamic picture with the potential energy profiles for loose *vs.* tight transition states (see Figure 2.2b), kinetic aspects should also be included. In this context it is important to consider unimolecular dissociation reactions from a statistical point of view which can be done with Rice-Ramsperger-Kassel-Marcus (RRKM) theory. In RRKM theory the microcanonical rate constant $k(E)$ is described as a ratio of the sum of states of the transition state $W^{\neq}(E-E_0)$ with an energy less or equal to $(E-E_0)$ over the total density of states of the reactant ion $\rho(E)$ (Equation 2.3).

$$k(E) = \frac{W^{\neq}(E - E_0)}{h\rho(E)} \tag{2.3}$$

When the activation energy for a reaction is exceeded, the rate constant increases rapidly with increasing internal energy. Since a larger number of rotational states is accessible at the loose transition state, in comparison to the tight transition state, the rate constant for a rearrangement reaction will increase much slower (dashed curve in Figure 2.2b).

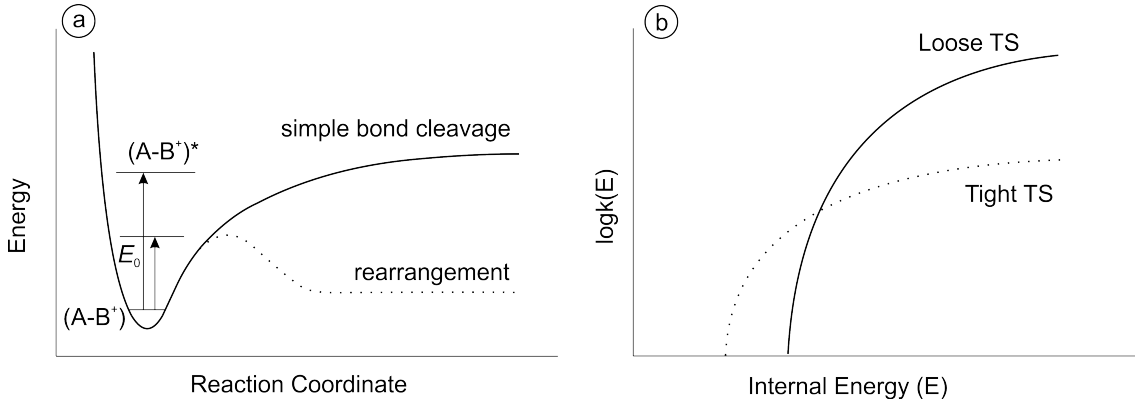

Figure 2.2: a) Potential energy profile for reaction over a loose (simple bond cleavage) or a tight (rearrangement) transition state[105]; b) hypothetical dependencies of log *k(E) vs. E* for simple bond cleavage (*via* a loose transition state), and a rearrangement reaction (*via* a tight transition state)[106].

Some of the investigated fragmentation reactions can produce two competitive channels: fragmentation occurring *via* a tight transition state (TS_2 in Figure 2.3) and a dissociation *via* a loose transition state (TS_1 in Figure 2.3, for further examples see Sections 4.3 and 4.4). Clearly, at low internal energies only the lower activation barrier of the tight transition state will be overcome, so the rate constant $k_2(E)$ plotted versus the internal energy of the activated complex starts rising at a lower internal energy E value (as shown in Figure 2.2b). However, at higher internal energies the situation changes and the rate constant for a reaction over a loose transition state ($k_1(E)$) exceeds the rate constant for the tight transition state reaction $k_2(E)$ because of the larger number of available quantum states. This will lead to larger thresholds for a fragmentation channel occurring *via* a loose transition state.

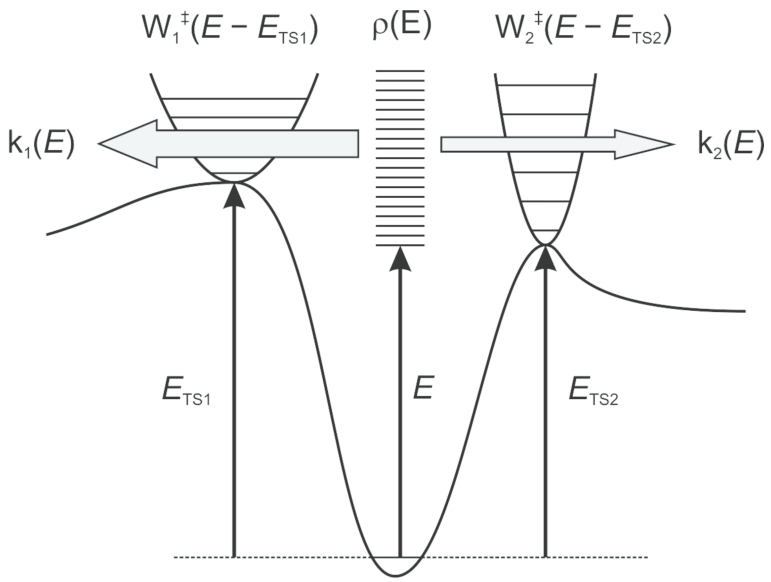

Figure 2.3: Competitive dissociation over a tight *vs.* loose transition state. Adapted from ref. [107].

2.3 Quadrupole ion trap mass spectrometer and determination of activation energies

The ESI quadrupole ion trap (QIT) mass spectrometer represents the combination of two Nobel Prize winning technologies: electrospray ionization and the quadrupole ion trap[9,108,109].

Most of the experiments for this dissertation were performed on a Finnigan LCQ Classic ion trap mass spectrometer (Figure 2.4) bearing a conventional ESI source that consisted of a spray unit connected to a syringe pump (typical applied flow rates: 0.3–0.7 $mL \cdot h^{-1}$). Nitrogen was used as a sheath and, when required, auxiliary gas. After the ESI the ions are directed into a heated transfer capillary, usually kept in the range 100–200 °C, and then through the first set of lenses that determined the ionization conditions (hard or soft by varying the degree of collisional activation in the medium-pressure regime)[89,110]. After exiting from the lenses the ions travel through two transfer octopoles and end in a Paul ion trap[109,111]. The ions are stored in the ion trap in the presence of the bath gas (usual He, 10^{-3} mbar) and ejected from the ion trap to an electron multiplier for detection.

It should be mentioned in passing that IT-MS experiments are usually affected by the presence of solvent molecules (acetonitrile, water, *etc.*) in the ion trap and their ability to attach to the investigated ion. This happens due to the relatively short distance between the inlet system and the trap.

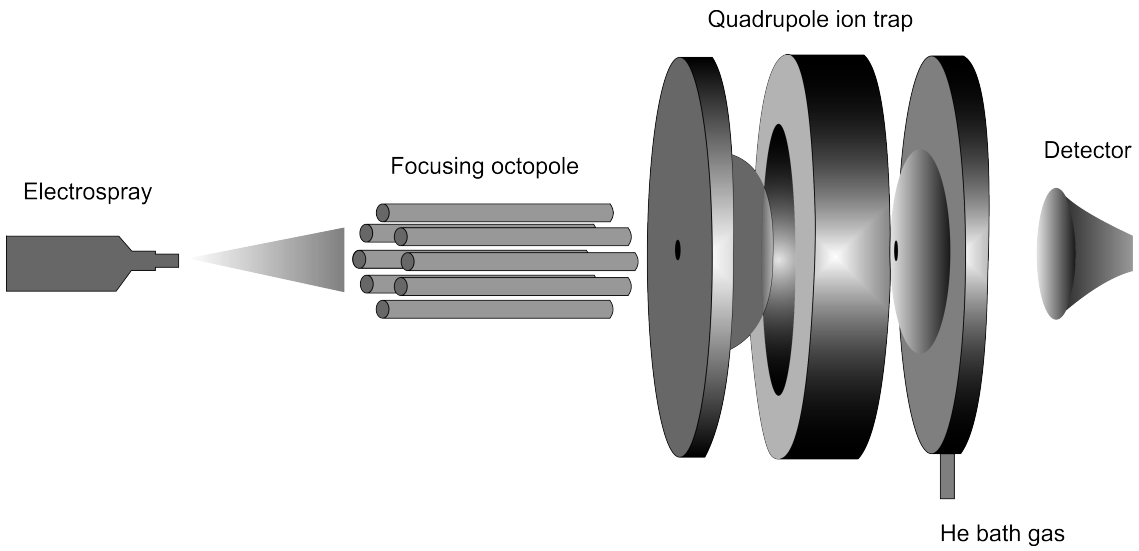

Figure 2.4: Simplified schematic diagram of the ESI-QIT mass spectrometer. The figure is adapted from ref. [112].

The instrumental setup of IT-MS also allows tandem mass spectrometric experiments to be performed. Tandem mass spectrometry, also known as MS/MS or MS^2, involves multiple steps of mass spectrometry selection, with some form of fragmentation occurring in between the stages. Fragmentation of the mass-selected ions in the Finnigan LCQ IT-MS is induced by resonance excitation processes that are achieved by the application of a supplementary RF voltage to the end caps of the trap. This increases the kinetic energy of the ions and induces collisions between the ions stored in the trap and the helium buffer gas. During the collision process, the kinetic energy of the ion can be partially transformed into internal energy which, when large enough, results in ion fragmentation. The product ions are then recorded by scanning the RF voltage to perform a second mass-analysis scan. A unique feature of the ion trap instruments is the ability to perform MS^n experiments (where $n > 2$). This means that an ion can be fragmented, and the resulting fragments further isolated and analyzed, helping to obtain structural information about complex molecules.

As collisional activation of the stored ions in an ion trap is induced by their RF-excitation, the ions undergo multiple collisions with the helium buffer gas present in the trap. Hence, CID experiments are easy to perform in IT-MS, but their quantitative analysis is difficult and cannot be performed by either CRUNCH or L-CID approaches[113,114].

It was shown that the RF voltage needed to induce an optimal amount of fragmentation is linearly dependent on the m/z of the mass-selected ion (Figure 2.5). Finnigan IT

mass spectrometers use an empirical approach called normalized collision energy (NCE) to compensate for this mass dependency. Here, the peak-to-peak voltage is scaled as $V_{pp} = NCE/30 \cdot (a \cdot \frac{m}{z} + b)$, where a and b are variable parameters[115].

However the use of NCEs to determine the appearance energies (AEs) of fragment ions is disadvantageous as it gives little information about real energetic demands for fragmentation. Therefore a calibration method was desired that would transform the manufacturer's NCEs into an approximate energy scale. Thus in 2010 the group of Detlef Schröder developed a method that allowed for this conversion[101].

Briefly, a series of benzylpyridinium salts was used as calibrants. A correlation was established between their phenomenological AEs determined with LCQ and the theoretically calculated activation energies. The fragmentation of benzylpyridinium salts is well-studied, both computationally and experimentally[116,117], as they were frequently used as "thermometer ions" for the evaluation of internal energy distributions[118–121]. During CID experiments most of the benzylpyridinium salts fragment with the loss of the neutral pyridine molecule and the formation of a benzylium ion.

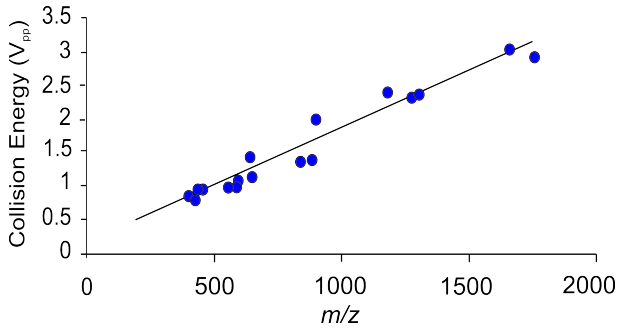

Figure 2.5: NCE technology in Finnigan instruments. The figure was adapted from ref. [115].

The energy dependent CID experiments result in a breakdown curve with a sigmoid shape. Quantitative analysis of this shape allows determination of the appearance energy of the ion. Then, an approach suggested by Bouchoux *et al.* can be used to model experimentally obtained curves[122]. The modeling is performed with sigmoid functions of the type $I_i(E) = a_i/(1 + e^{(E_{1/2,i}-E)b_i})$ using a least-squares criterion. For the parent ion M, the dependence could be rewritten as:

$$I_M(E) = 1 - [a_i/(1 + e^{(E_{1/2,i}-E)b_i})] \tag{2.4}$$

where a_i stands for the branching ratio of a particular product ion ($\sum a_i = 1$), $E_{1/2}$

is the energy at which the sigmoid function has reached half of its maximum, E is the collision energy and b (in eV^{-1}) describes the rise of the sigmoid curve and thus the phenomenological energy dependence. The phenomenological AEs are then derived from a linear extrapolation of the rise of the sigmoid curve at $E_{1/2}$ to the baseline.

An example of a calibration obtained by the described method is shown in Figure 2.6. For this calibration energy-resolved CID experiments were performed for four benzylpyridinium ions (2,5-dimethyl-, 3,5-dimethyl-, *o*-methyl- and pentamethyl-). The obtained curves were modeled with the above mentioned sigmoid functions and the AEs of the fragment ions were obtained (in NCE, Figure 2.6a–d). Then the experimental NCE values were plotted against calculated AE values for the corresponding ions (Figure 2.6e). The resulting linear dependence was then used for the conversion of the experimentally relevant AEs. Note that the line is forced through the origin.

As was shown by Zins *et al.*[101], the addition of an adjustable abscissa does not significantly increase the quality of the fit. Moreover, the obtained conversion factor strongly depend on the instrument used and also sensitive to the condition changes of the IT-MS. In this respect, a single-parameter fit is considered to be more convenient and robust for a rapid re-calibration.

In conclusion, the family of closely related benzylpyridinium ions showed a good correlation between the experimental AEs with the calculated values. However, it is important not to overestimate this approach, because both the assumption of a sigmoid behavior and the use of a linear conversion factor are phenomenological approaches to ion dissociation, which is fairly more complex.

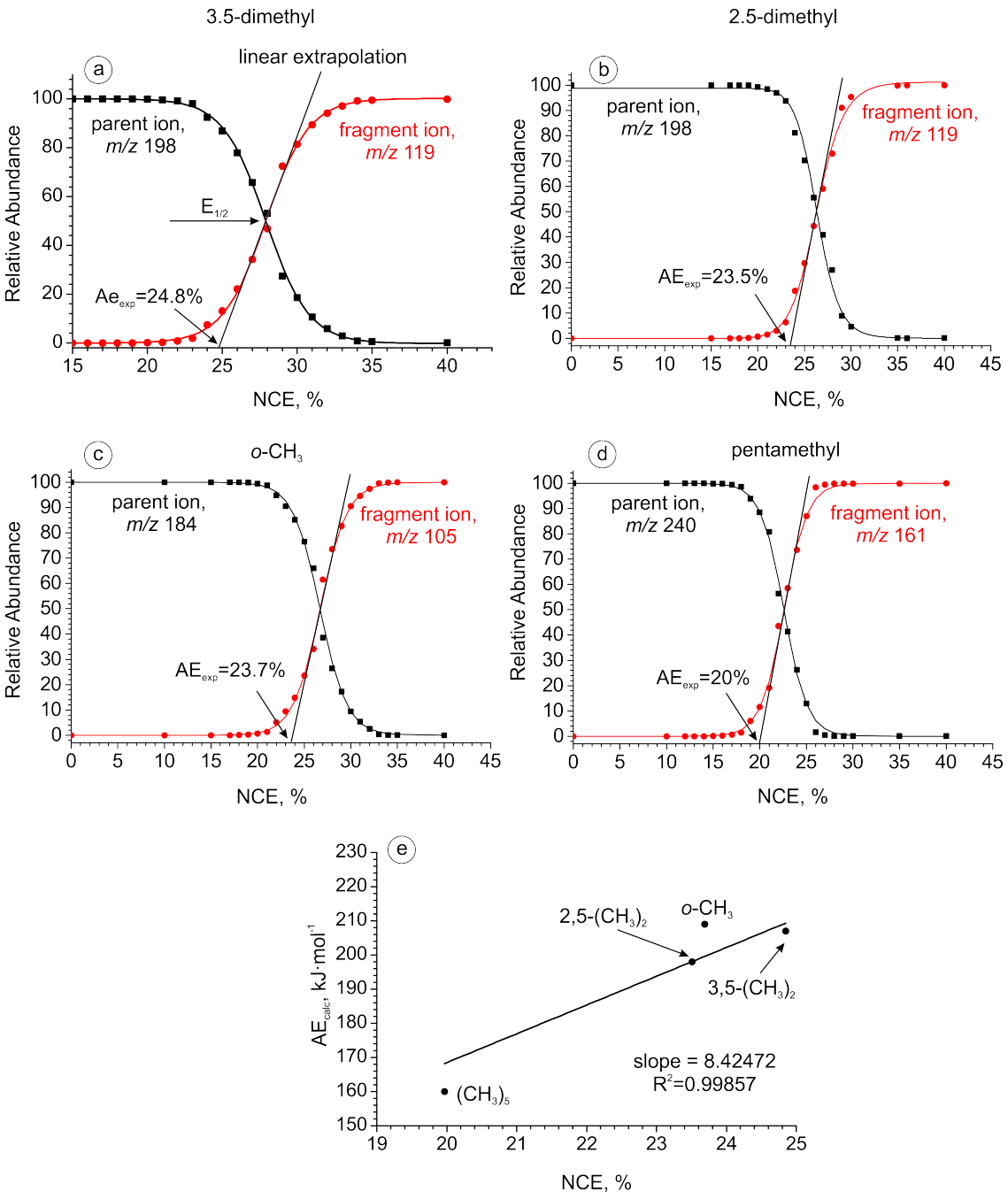

Figure 2.6: a) Breakdown diagrams of mass-selected a) [3,5-dimethylC_6H_3-CH_2-NC_5H_5]$^+$; b) [2,5-dimethylC_6H_3-CH_2-NC_5H_5]$^+$; c) [*o*-CH_3-C_6H_4-CH_2-NC_5H_5]$^+$ and d) [$C_6(CH_3)_5$-CH_2-NC_5H_5]$^+$ as a function of the relative collision energy. The dots represent the experimental data; the solid lines - the sigmoid functions used for analysis. e) Calibration plot of the characteristic experimental parameters AE_{exp} versus the computed AE_{calc} values. The correlation line is forced to cross the origin.

2.4 Ion mobility mass spectrometry

In early 60's McDaniel and co-workers introduced the idea of gaseous ion separation in a drift tube, by attaching a low-field ion mobility drift cell to a sector mass spectrometer. At that time it was done for the investigation of ion-molecule reactions[123]. However the potential of such separation was not fully realized until it was demonstrated for protein conformers by Clemmer *et al.*[124].

Ion mobility spectrometry (IMS) separates ions in accordance with their shape, and is often called "chromatography in the gas phase"[125,126]. During this analysis, the investigated ions are directed into a chamber with a weak electric field, filled with an inert gas. While traversing the chamber, the ions reduce their speed by undergoing a number of collisions with the neutral gas molecules. Larger ions undergo more collisions and therefore require more time to elute from the chamber than the smaller ions.

The result of coupling IMS with mass spectrometry is often called ion mobility mass spectrometry (IM-MS). These two analytical methods perfectly complement one another and therefore IM-MS has become a rapidly developing technique in analytical chemistry. Although IM-MS is mostly used for the analysis of complex biological mixtures, the separation of small molecules is also possible[127]. For example, IM-MS of the *p*-hydroxybenzoic acid solution is capable of tautomer separation in the gas phase[75]. The IM-MS results discussed in this dissertation were obtained with a SYNAPT G2 mass spectrometer (WATERS, Manchester, U.K.), equipped with an ESI source (see Figure 2.7).

The instrument consists of four main regions: ion generation, ion selection, ion mobility separation and ion mass analysis. The ions are generated in the ESI source. Its geometry and design are considerably different than those of ion sources employing a heated transfer capillary (*e.g.* LCQ instrument). The ESI source in Synapt G2 instrument has so-called Z-spray geometry, where an electrospray is placed orthogonally to a sampling cone. The voltage applied to a sampling cone attracts appropriately charged ions with a velocity that allows them to come into the mass spectrometer. The desolvation of ions is facilitated by heated nebulizing gas (N_2).

The ions, entering the vacuated region, are being transferred to the quadrupole analyzer (capable of detecting ions up to 32000 m/z), which can be used as a mass filter. Behind the quadrupole, linear ion trap filled with argon is situated, where the selected ions are collected. When the ion mobility mode is switched on, the ions are emitted from linear

ion trap in a single pulse to the ion mobility cell filled with ∼2 mbar of nitrogen. After the mobility cell, the ions pass a transfer cell and end up in the reflectron time-of-flight mass spectrometer. The absolute values of the arrival times (t_a) in the SYNAPT G2 depend on the voltage and pressure settings. Therefore, any comparison between different arrival times should be done under identical conditions[128]. Also, different options exist for energizing the ions in the SYNAPT instrument[129]. As such, the ionization conditions (soft to hard) can be modified by changing the cone voltage (U_C) in the ion source. Larger cone voltages can sometimes induce source fragmentation[68,89].

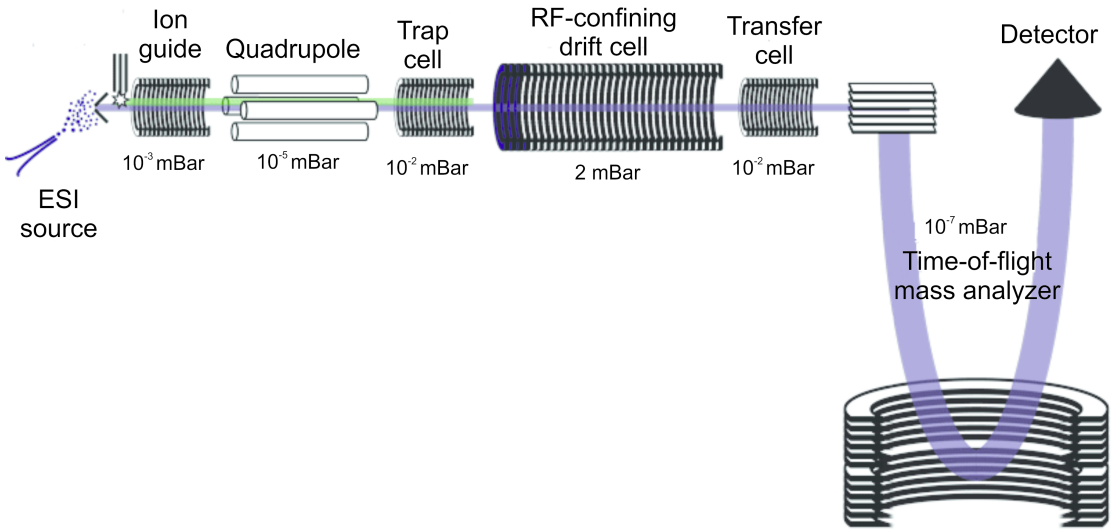

Figure 2.7: General scheme describing the SYNAPT G2 ion mobility mass spectrometer. The scheme is adapted from ref. [130].

2.5 Infrared multiphoton dissociation spectroscopy

Ion spectroscopy represents yet another dimension for ion structure investigations. The basic principle of such studies lies in the comparison of experimentally obtained infrared or ultraviolet ion spectra with theoretical spectra of different possible isomeric structures of the investigated ion. Therefore the exact structure of the experimentally observed ion can be determined.

The spectra discussed in this dissertation were achieved with multiple photon absorption; ion fragmentation was induced by the sequential absorption of several IR photons (Figure 2.8). The method is therefore called infrared multiphoton dissociation spectroscopy (IRMPD). As the experimental spectra are multiphotonic in nature, they do not always

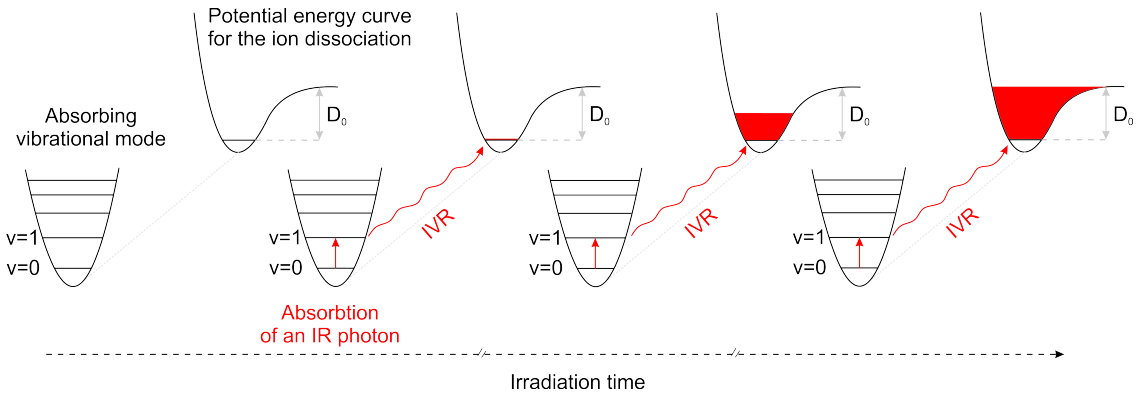

Figure 2.8: Sequential excitation–relaxation cycles during infrared multiphoton dissociation spectroscopy. This figure is adapted from ref. [51].

match with the calculated IR spectra[131,132].

Sequential processes of photon absorption are best achieved with free-electron lasers (FELs, on the order of 40 MeV). In a FELs an accelerated beam of electrons travels through a periodic magnetic field (undulator) that forces electrons to oscillate around the axis. This results in emission of light from the electron beam, which is stored in an optical cavity and can again interact with the electrons. This interaction leads to the growth of the intensity of emitted light and to the modulation of its electronic density.

Changing the energy of the electron beam and the parameters of the undulator produces a wide range of wavelengths. The IRMPD spectra for this dissertation were obtained at CLIO (Centre Laser Infrarouge Orsay, France), which is operating in the finger-print region (800–1800 cm^{-1}).

Chapter 3

Experimental details

Instrument control and data analysis for the Finnigan LCQ Classic ion trap mass spectrometer were performed with Xcalibur software version 2.0.7 (Thermo Fisher Scientific). For ion isolation in MS^n ($n \geqslant 2$) experiments, where possible, the isolation width was adjusted to select a single nominal mass and the lightest isotope (*e.g.* ^{1}H, ^{12}C, ^{32}S, ^{63}Cu). We found an isolation width of 1-2 amu to be sufficient for that purpose. The whole isotopic range (typically, m/z 10–15) for a selected ion was used when the mass-selection of a single isotope did not provide an intensity sufficient for further MS^n experiments. Instrument control and data analysis for SYNAPT G2 instrument were performed with MassLynx software version 4.1.

All of the mass spectra were acquired for $\geqslant 2$ min with a scan duration of 1 s. These accumulated spectra were exported from Xcalibur and MassLynx software into an Excel sheet for further analysis. Identification of peaks was usually done by comparison of experimental and theoretical m/z ratios as well as by creation of isotope distribution model for an ion of interest in the Xcalibur and MassLynx software.

It is important to note that speciation of any spraying solution is instrument dependent. Thus, it is often impossible to obtain identical spectra for the same solution with two different instruments (also within the same type), even when identical electrospray conditions are used. Therefore, all of the spectra within the same project were recorded with the same instrument. In addition, the speciation and distribution of abundances of the observed ions are dependent on how clean a particular instrument is. For example, dirt at the heated transfer capillary (*e.g.* resulting from the adsorption of salts from spraying solutions) may affect the abundance distribution, and in fact may lead to the irreproducibility of the previously obtained spectra.

3.1 Copper acetate speciation

3.1.1 Chemicals

Preparation of copper(II) d^3-acetate monohydrate was done according to the literature[133]. Briefly, $Cu(OH)_2 \cdot CuCO_3$ (prepared by precipitation of aqueous $CuSO_4 \cdot 5H_2O$ with Na_2CO_3; 1.125 g; 5.088 mmol) was suspended in 20 mL of water with subsequent dropwise addition of d^4-acetic acid. Then, the reaction mixture was stirred at room temperature for 30 minutes, filtered and precipitated by adding dropwise into 500 mL of acetone. The resulting blue-green precipitate was collected by filtration, washed with acetone (100 mL) and dried under reduced pressure. Copper(II) d^3-acetate was obtained in 66% yield (1.380 g).

Copper(II) acetate as well as the solvents were purchased from Sigma-Aldrich and used without further purification. Distilled water was used in all of the experiments.

3.1.2 Preparation of the spraying solutions

For the initial ESI-MS experiments separate 10^{-3} M solutions of $Cu(OAc)_2$ in methanol and acetonitrile were prepared. We found that while acetonitrile solutions with lower concentrations of $Cu(OAc)_2$ (*e.g.* 10^{-4} M) were sufficient, dilute methanol solutions produced unsatisfactory spectra. For example, ESI-MS of a 10^{-4} M $Cu(OAc)_2$ solution in methanol resulted in the large abundance of peaks most likely arising from impurities accompanying the $Cu(OAc)_2$ salt (see Figure 3.1). In addition, we were not able to detect any peaks that had a characteristic Cu-isotope pattern.

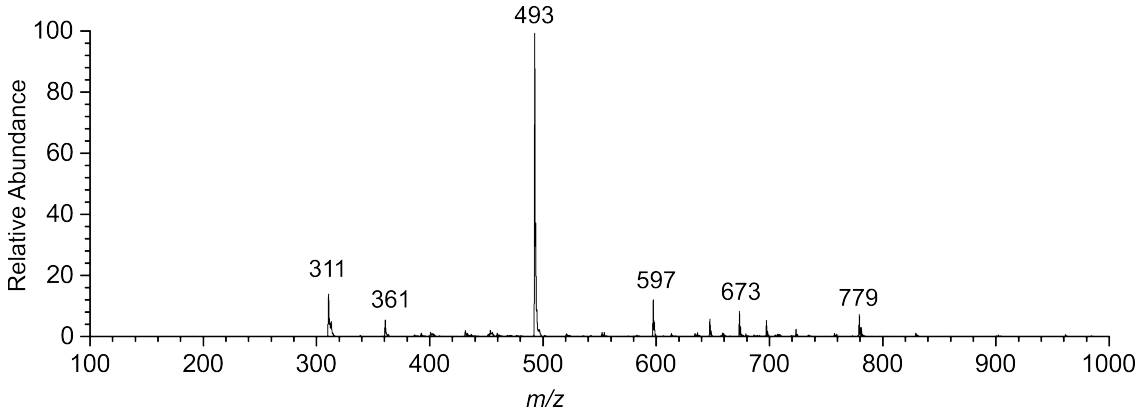

Figure 3.1: ESI-MS of a methanolic solution of $Cu(OAc)_2$ (10^{-4} M) in a positive ion mode.

During the concentration series analysis, the measurements started with spraying the

most dilute solutions and continued towards higher concentrations. The inlet system was properly cleaned in-between measurements with pure methanol/acetonitrile.

In all of the working solutions prepared for the investigation of the water effect, the concentration of $Cu(OAc)_2$ was 10^{-3} M. In order to avoid memory effects, the investigation started with the analysis of a $Cu(OAc)_2$ solution in pure methanol/acetonitrile and continued in small steps to the investigation of higher water contents. The inlet system was again thoroughly cleaned in-between measurements with pure methanol/acetonitrile.

The solubility of $Cu(OAc)_2$ was determined for 11 methanolic solutions with different amount of added water (in vol%): 0% , 0.5%, 1%, 1.5%, 2%, 2.5%, 3%, 5%, 7%, 10% and 15%. The method for all 10 samples was the following: first, the supersaturated solution of a $Cu(OAc)_2$ in the corresponding solvent (pure methanol or a mixture $MeOH/H_2O$, 2.5 mL) was prepared (a large excess of $Cu(OAc)_2$ was put into the solvent and then sonicated for 1 hour). Afterwards the solution was filtrated and the solvent evaporated under reduced pressure. The mass of the dry residue was recorded.

For the experiments with deuterated copper acetate, a 10^{-3} M solution of $Cu(CD_3COO)_2$ in MeOH was prepared.

3.1.3 ESI-MS experiments

The mass spectrometric experiments were performed with a Finnigan LCQ ion-trap mass spectrometer equipped with an ESI source. Nitrogen was used as the nebulizing gas, and samples were introduced into the ESI source *via* a silica capillary (100 µm, internal diameter) at a flow rate of 2 $\mu L \cdot min^{-1}$. The operating conditions were set as follows: spray voltage 4.5 kV, capillary voltage 0 V, heated capillary temperature 200 °C, tube lens offset 0 V, sheath and auxiliary gas flow rate 30 and 10 arbitrary units, respectively. Under these conditions, the ionization in ESI is relatively soft, such that quasi-molecular ions, as well as their aggregates with solvents, can be observed. Slightly softer conditions can still be achieved, however they may cause the observed abundances of cluster ions to be highly dependent on the voltage settings. Thus the selected conditions are a compromise between the softness of the ionization process and achieving a sufficient reproducibility and sensitivity for the sampling of all the copper species described in Section 4.1. For further characterization, dissociation of the mass-selected ions was achieved by collisional activation *via* RF excitation using the helium buffer gas present in the ion trap as a collision partner. Mass spectra were recorded from m/z 50 to 2000 in positive- as well as

in negative-ion mode.

In order to support the assignments made for the various species observed with the ion trap mass spectrometer, additional exploratory high resolution MS experiments were performed with a Waters SYNAPT G2 ion mobility instrument. The spectra on the SYNAPT G2 were recorded with cone voltages (U_C) of 20 V, which represented relatively mild conditions. The samples were introduced with a flow rate 0.5 $mL \cdot h^{-1}$. Other parameters were set as follows: electrospray capillary voltage 3.5 kV, desolvation gas temperature 150 °C, extraction cone voltage 4 V. Accurate masses were determined *via* internal calibration with spiked reference compounds with known mass-to-charge ratios. In most cases, the obtained differences are below ± 0.002 amu (Table 3.1) and thus fully support the assignments made on the basis of the IT-MS experiments. The only exception is the somewhat larger deviation for the ion at *m/z* 699 assigned as $[Cu_4(OAc)_6(OCH_3)_3]^-$.

Table 3.1: Measured and calculated masses of complexes discussed in Section 4.1.

	calculated	experimental	Δm, milliamu
$[Cu(CH_3CN)]^+$	103.9561	103.9565	-0.4
$[Cu(CH_3CN)(H_2O)]^+$	121.9667	121.9668	-0.1
$[Cu(CH_3CN)_2]^+$	144.9827	144.9827	0.0
$[CuOAc(CH_3OH)]^+$	153.9691	153.9692	-0.1
$[Cu(OAc)(CH_3CN)]^+$	162.9694	162.9695	-0.1
$[Cu(OAc)(CH_3OH)_2]^+$	185.9953	185.9946	0.7
$[NaCu(OAc)_2]^+$	203.9459	203.9460	-0.1
$[Cu_2(OAc)_2]^+$	243.8857	243.8871	-1.4
$[Cu_2(OAc)_3(CH_3CN)]^+$	343.9256	343.9262	-0.6
$[NaCu_2(OAc)_4]^+$	384.9021	384.9026	-0.5
$[Cu_3(OAc)_4(OCH_3)]^+$	455.8604	455.8606	-0.2
$[Cu_3(OAc)_5]^+$	483.8553	483.8551	0.2
$[NaCu_3(OAc)_6]+$	565.8583	565.8574	0.9
$[Cu_4(OAc)_4(OCH_3)_3]^+$	580.8267	580.8249	1.8
$[Cu_4(OAc)_5(OCH_3)_2]^+$	608.8216	608.8235	-1.9
$[Cu_4(OAc)_7]^+$	664.8115	664.8118	-0.3
$[Cu_5(OAc)_5(OCH_3)_4]^+$	733.7880	733.7861	1.9
$[NaCu_4(OAc)_8]^+$	746.8145	746.8145	0.0
$[Cu_5(OAc)_6(OCH_3)_3]^+$	761.7829	761.7839	-1.0
$[Cu_5(OAc)_9]^+$	845.7677	845.7680	-0.3
AcO^-	59.013295	59.0135	-0.2
$[Cu(OAc)_2]^-$	180.9562	180.9557	0.5
$[Cu(OAc)_3]^-$	239.9695	239.9696	-0.1
$[Cu_2(OAc)_4(OCH_3)]^-$	392.9308	392.9307	0.1
$[Cu_2(OAc)_5]^-$	420.9257	420.9260	-0.3
$[Cu_3(OAc)_5(OCH_3)_2]^-$	545.8920	545.8910	1.0
$[Cu_3(OAc)_6(OCH_3)]^-$	573.8870	573.8863	0.7
$[Cu_4(OAc)_6(OCH_3)_3]^-$	698.8533	698.8616	-8.3

3.1.4 EPR measurements

EPR spectra were recorded by our collaborators (Bradford L. Ryland and Shannon S. Stahl) on a Bruker EleXsys E500 spectrometer at 77 K under nonsaturating conditions. Spin quantitation was performed by baseline-corrected double integration of spectra relative to calibration curves of a $Cu(OTf)_2$ external standard.

3.2 Investigation of copper catalyzed aerobic cross coupling of thiol esters and arylboronic acids

3.2.1 Chemicals

The general procedure for the coupling of thiol esters with boronic acids was described previously[134]. S-(2-(benzylcarbamoyl)phenyl) benzothioate (thiol ester **1**), S-(2-(benzylcarbamoyl)phenyl) benzothioate (thiol ester **1**') and N-benzyl-2-mercaptobenzamidel (thiol **5**) were provided by our collaborators: Dr. Adam Henke and Dr. Jiři Šrogl.

Copper(II) acetate and methanol were purchased from Sigma-Aldrich and used without further purification.

3.2.2 Preparation of the spraying solutions

a) thiol ester **1** solution: ∼1 mg of thiol ester **1** was dissolved in 1 mL of methanol (solution A). A drop (∼10 µL) of solution A was taken, and dissolved in 1 mL of methanol (solution B). The obtained solution B was used in ESI-MS experiments.

b) 4-tolylboronic acid solution: the methanolic solution of 4-tolylboronic acid used for ESI-MS characterization was prepared similarly to solution B of thiol ester **1**.

c) mixture of 4-tolylboronic acid with $Cu(OAc)_2$: ∼0.5 mg of 4-tolylboronic acid was mixed with ∼0.5 mg of $Cu(OAc)_2$ in 1 mL of methanol (sonicated for 10 min). The obtained mixture was dissolved three fold and the resulting solution used in ESI-MS experiments.

d) mixture of thiol ester with $Cu(OAc)_2$: ∼1 mg of thiol ester **1** was mixed with ∼0.5 mg of $Cu(OAc)_2$ in methanol (sonicated for 10 min). The obtained mixture was diluted three fold and the resulting solution used in ESI-MS experiments.

e) mixture of all the reaction components in methanol: ∼1 mg of thiol ester **1** was mixed with ∼0.5 mg of $Cu(OAc)_2$ and ∼0.5 mg of 4-tolylboronic acid in 1 mL of methanol. The obtained mixture was diluted three fold and the resulting solution used in ESI-MS

experiments.

f) mixture of thiol ester **1'**, 4-tolylboronic acid and $Cu(OAc)_2$ in methanol: ~1 mg of thiol ester **1'** was mixed with ~0.5 mg of $Cu(OAc)_2$ and ~0.5 mg of 4-tolylboronic acid in 1 mL of methanol. The obtained mixture was diluted three fold and the resulting solution used in ESI-MS experiments.

g) mixture of thiol ester **1**, phenylboronic acid and $Cu(OAc)_2$ in methanol: ~1 mg of thiol ester **1** was mixed with ~0.5 mg of $Cu(OAc)_2$ and ~0.5 mg of phenylboronic acid in 1 mL of methanol. The obtained mixture was diluted three fold and the resulting solution used in ESI-MS experiments.

h) mixture of thiol **5** and $Cu(OAc)_2$: ~1 mg of thiol **5** was mixed with ~0.5 mg of $Cu(OAc)_2$ in 1 mL of methanol. The obtained solution was diluted three fold and the resulting solution used in ESI-MS experiments.

i) mixture of thiol **5,** $Cu(OAc)_2$ and 4-tolylboronic acid: ~1 mg of thiol **5** was mixed with ~0.5 mg of $Cu(OAc)_2$ and ~0.5 mg of 4-tolylboronic acid in 1 mL of methanol. The obtained solution was diluted three fold and the resulting solution used in ESI-MS experiments.

j) for on-line monitoring experiments the reaction mixture was prepared by mixing thiol ester (0.0016 g, $4.6 \cdot 10^{-6}$ mol, 1.0 equiv) in a 10 mL vial equipped with a magnetic stirrer bar with a catalytic amount (5 mol%) of copper acetate and 4-tolylboronic acid (0.0014 g, $10.6 \cdot 10^{-6}$ mol, 2.5 equiv). 2 mL of dry dimethylformamide was added, and the mixture was stirred at a certain temperature (40, 50, 60 or 80 °C). After a given time from the beginning of the reaction, an aliquot (20 μL) of the reaction solution was taken, dissolved in 2 mL of MeOH, and sprayed into the mass spectrometer.

The catalyst ($Cu(OAc)_2$), 4-tolylboronic acid, phenylboronic acid and HPLC-grade solvents were purchased from Sigma Aldrich and used without further purification.

3.2.3 ESI-MS experiments

The reaction mixtures were studied using a Finnigan LCQ Classic ion-trap mass spectrometer equipped with an ESI ion source. The operation conditions were the following: spray voltage 4.5 kV; capillary voltage 0 V, capillary temperature 150 °C; tube lens offset 0 V, auxiliary gas flow rate 50 arbitrary units, sheath gas flow rate 30 arbitrary units. The samples were introduced at a flow rate of 0.7 $mL \cdot h^{-1}$. Mass spectra were recorded from m/z 50 to 1500.

The assignments of the complexes were further supported by high resolution measurements on a SYNAPT G2 mass spectrometer. The samples were introduced at a flow rate 0.5 mL·h^{-1}. Other parameters were set as follows: electrospray capillary voltage 3.5 kV, desolvation gas temperature 150 ^{o}C, sampling cone voltage 20 V, extraction cone voltage 4 V. Internal calibration with reference compounds of known mass-to-charge ratios allowed accurate masses to be determined. In most cases, the differences are below ± 0.0002 amu (Table 3.2), fully supporting the assignments made on the basis of the IT-MS experiments.

Table 3.2: Measured and calculated masses of complexes discussed in Section 4.2.

	calculated	experimental	Δm, milliamu
[(**1**)H]$^+$	348.1058	348.1059	-0.1
[(**1**)Na]$^+$	370.0878	370.0877	0.1
[(**1**)Cu]$^+$	410.0276	410.0273	0.3
[(**1**)$_2$Na]$^+$	717.1857	717.1854	0.3
[(**1**)$_2$Cu]$^+$	757.1256	757.1254	0.2
[(int)Cu]$^+$	304.9936	304.9942	-0.6
[(**1**)CuOAc]$^+$	469.0409	469.0409	0.0
[(**1**)$_2$CuOAc]$^+$	816.1389	816.1381	0.8
[(**1**)$_3$Ca]$^{2+}$	540.6283	540.6277	0.6
[(**4**)H]$^+$	334.1266	334.1248	1.8
[(**4**)Na]$^+$	356.1085	356.1095	-1.0
[(**4**)Cu]$^+$	396.0483	396.0485	-0.2
[(**4**)CuOAc]$^+$	455.0616	455.0614	0.2
[(**1**)(int)Cu]$^+$	652.0915	652.0910	0.5
[(**1**)(**4**)Cu]$^+$	743.1463	743.1457209	0.6
[(**1**)(**4**)Na]$^+$	703.2065	703.2075	-1.0

The empirical calibration scheme described in detail in Section 2.3 (with an excitation period of 20 ms and a trapping parameter (q_z) of 0.25) allowed conversion of the experimental AEs of the fragmentation pathways to an absolute energy scale.

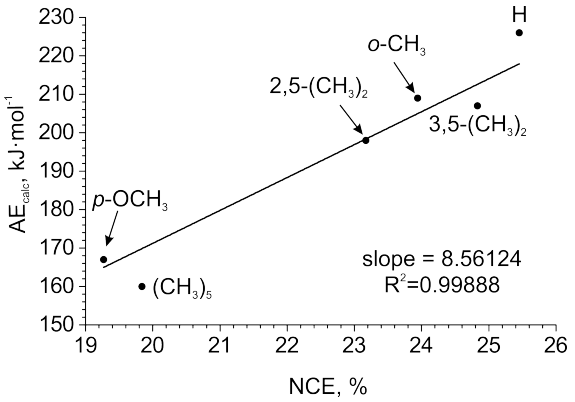

Figure 3.2: Calibration plot of the characteristic experimental parameters AE_{exp} versus the computed AE_{calc} values. The correlation line is forced through the origin.

To this end, for all of the CID experiments in Section 4.2 the calibration dependence shown in Figure 3.2 was used. The energy-resolved CID experiments were performed for six benzylpyridinium ions (2,5 dimethyl-, 3,5-dimethyl-, H-, *o*-methy-, pentamethyl- and *p*-methoxy-).

For accurate determination of AE values, at least three reproducible energy-resolved CID experiments were performed, and the final AE was taken as an average of these experiments.

3.3 Coordination and bond activation in complexes of regioisomeric phenylpyridines with nickel(II)

3.3.1 Chemicals

2-, 3-, and 4-PhPy, D_5-pyridine as well as the solvents were purchased from Sigma-Aldrich and used without further purification.

3.3.2 Preparation of the spraying solutions

For all mass spectrometric experiments (if not noted otherwise) dilute solutions (10^{-4} M) of nickel(II) chloride in water/methanol (1:1) in the presence of a three-fold excess of the respective phenylpyridine(s) were prepared.

For the generation of mixed complexes of the form $[NiCl(PhPy)(D_5\text{-}Py)]^+$ the following solution was used: to the 10^{-4} M solution of nickel(II) chloride in water/methanol (1:1), 3 equivalents of both phenylpyridine and D_5-Py were added.

3.3.3 ESI-MS experiments

Initial experiments for the characterization of the ions of interest were performed using a Finnigan LCQ Classic ion trap mass spectrometer. The ions of interest were generated by electrospray ionization of dilute solutions of nickel(II) chloride in water/methanol (1:1) in the presence of a three-fold excess of the respective phenylpyridine(s). The operation conditions were the following: spray voltage 4.5 kV; capillary voltage 0 V, capillary temperature 200 °C; tube lens offset 0 V, auxiliary gas flow rate 30 arbitrary units, sheath gas flow rate 10 arbitrary units. The samples were introduced at a flow rate of 0.5 $mL \cdot h^{-1}$.

The empirical calibration scheme described in detail in Section 2.3 (with an excitation period of 20 ms and a trapping parameter of $q_z = 0.25$) allowed conversion of the

experimental AEs to an absolute energy scale. For all of the CID experiments in Section 4.3 the calibration dependence shown in Figure 3.3 was used. The energy-resolved CID experiments were performed for six benzylpyridinium ions (2,5-dimethyl-, 3,5-dimethyl-, H-, *o*-methyl-, pentamethyl- and *p*-methoxy-).

For accurate determination of AE values, at least three reproducible energy-resolved CID experiments were performed, and the final AE was taken as an average of these experiments.

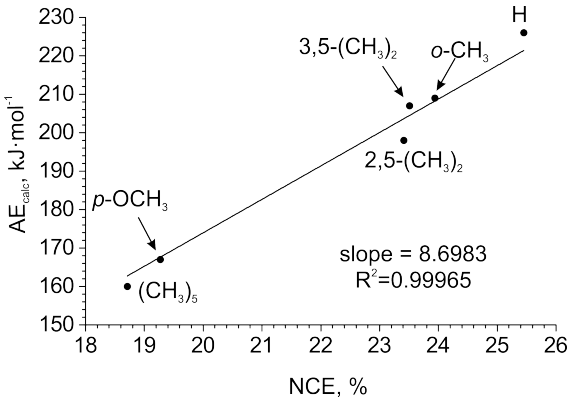

Figure 3.3: Calibration plot of the characteristic experimental parameters AE_{exp} versus the computed AE_{calc} values. The correlation line is forced through the origin.

3.3.4 Ion mobility measurements

The SYNAPT G2 mass spectrometer was used for ion mobility experiments. The investigated species were formed by ESI of the same $NiCl_2$-PhPy solutions that were used for initial ESI-MS experiments. The solutions were infused at a flow rate of 0.5 mL·h^{-1}; the desolvation gas temperature was kept at 200 °C, electrospray capillary voltage 2.5 kV, Extracting cone voltage was 4 V and sampling cone voltage is specified below for each experiment in Section 4.3.

3.3.5 Quantum chemical calculations

Density functional theory calculations were performed with the Gaussian 09 suite[135] and Turbomole 6.3[136]. Geometry optimizations were done at the B3LYP-D3/def2-SVP level[137–141], which includes version 3 of Grimme's empirical dispersion correction[142]. For all optimized structures, frequency analysis was performed at the same level of theory in order to assign them as genuine minima or transition structures on the potential energy surface (PES), as well as to calculate zero-point vibrational energies (ZPVEs). Subsequently,

single-point energy calculations were performed using the M06 functional[143] and the def2-TZVPP basis set[141], where no empirical dispersion is added because the functional itself accounts for dispersion in the vicinity of equilibrium geometries. The energies in the thesis refer to a temperature of 0 K in the gaseous state; singlet−triplet state splittings are adiabatic and include ZPVE. Singlet states were calculated with broken-symmetry[144] open-shell wave functions that were lower in energy than the closed-shell solutions.

3.4 Carboxylate assisted C-H activation of phenylpyridines with copper, palladium and ruthenium

3.4.1 Chemicals

All of the chemicals used in the experiments were purchased from Sigma Aldrich and used without further purification.

3.4.2 Preparation of the spraying solutions

For the initial MS experiments, 10^{-4} M stock solutions of the corresponding carboxylate salt (*e.g.* $Cu(OAc)_2$, $Pd(OAc)_2$) in acetonitrile were prepared. In the case of ruthenium carboxylate catalyzed C-H activation, the reactive catalytic species had to be generated *in situ* from the commercially available dimeric complex: $[(C_6H_6)RuCl_2]_2$. We therefore prepared a 10^{-4} M solution of the corresponding ruthenium dimer in acetonitrile, and added 1 equivalent of acetic acid and triethylamine.

For the investigation of carboxylate assisted C-H activation, 1 equivalent of 2-phenylpyridine was added to each of the stock solutions. It is very important that solutions containing 2-PhPy are freshly prepared (especially those used in energy-resolved CID measurements) so that the concentration of non-activated complexes allows for their easier detection and characterization.

The dependence of 2-phenylpyridine concentration on the formation of Ru-ions in the gas phase was studied with more concentrated solutions to allow for easier detection of ruthenium complexes. The catalytic solution was prepared as following: a 10^{-3} M solution of ruthenium dimer in acetonitrile was prepared, followed by addition of 1 equivalent of acetic acid and triethylamine.

For Hammett studies, 1 equivalent of 2-phenylpyridine and 1 equivalent of the corresponding benzoic acid were added to the stock solutions and the obtained mixtures were

used in MS experiments.

3.4.3 ESI-MS experiments

The experiments were performed on a Finnigan LCQ ion trap mass spectrometer equipped with an ESI source. The studied solutions were introduced to the ESI source through a fused-silica capillary by a syringe pump at a rate of 3 μL·min^{-1}. Nitrogen was used as a nebulizing and drying gas throughout the experiments. The operating conditions were set as follows: spray voltage 4.5 kV, capillary voltage 0 V, tube lens offset 0 V, heated capillary temperature 150 °C. Auxiliary gas flow and sheath gas flow rates were set at 5 arbitrary units each. All of the mass spectra were recorded from *m/z* 50 to *m/z* 1000. Collision-induced dissociation of mass selected precursor ions was achieved by RF-excitation of the ions within the ion trap where He was used as the buffer gas and collision partner.

The collision energy was optimized for each experiment and Schröder's calibration method allowed conversion of experimental *AE* values to an absolute energy scale. For the CID experiments that required an isolation width of 1 *m/z,* discussed in Section 4.4, the calibration dependence shown in Figure 3.4 was used. The energy-resolved CID experiments were performed for four benzylpyridinium ions (2,5-dimethyl-, 3,5-dimethyl-, *o*-methyl- and pentamethyl-).

For accurate determination of *AE* values, at least three reproducible energy-resolved CID experiments were performed, and the final *AE* was taken as an average of these experiments.

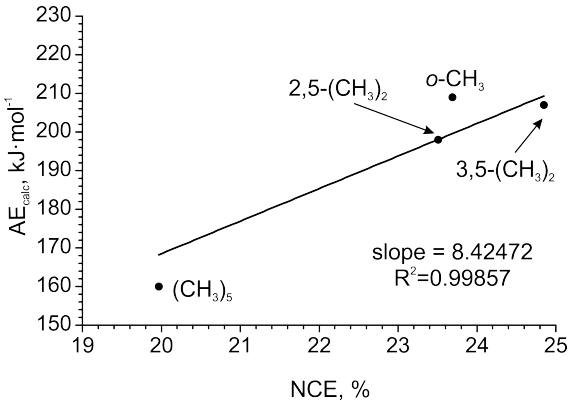

Figure 3.4: Calibration plot of the characteristic experimental parameters AE_{exp} versus the computed AE_{calc} values. The correlation line is forced through the origin.

For the estimation of *AE*s for palladium complexes a different calibration, performed

specifically for the case with isolation width 10 m/z was used (Figure 3.5)

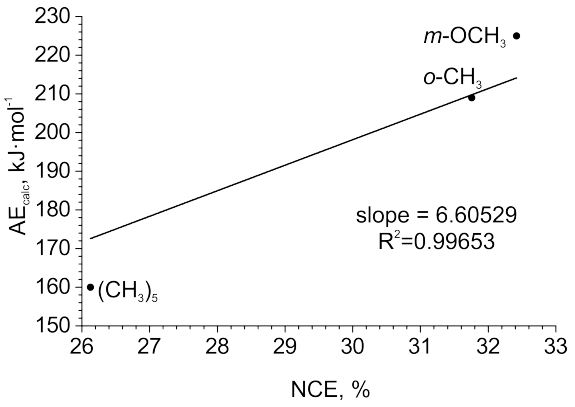

Figure 3.5: Calibration plot of the characteristic experimental parameters AE_{exp} versus the computed AE_{calc} values. The correlation line is forced through the origin.

3.4.4 Quantum chemical calculations

Density functional theory calculations were performed with the Gaussian 09 suite[135]. The B3LYP method was used for all calculations. Two different combinations of basis sets were applied. With the acetate counter ion, the cc-pVTZ basis set was used for O, N, C and H and where appropriate the cc-pVTZ-pp basis set was applied for the metals. With benzoate and 4-nitrobenzoate counter ions, the 6-31G* basis set was used for O, N, C and H and the SDD basis set was applied for Ru, Cu and Pd. All of the structures have been fully optimized and established as genuine minima or transition states on the appropriate potential energy surfaces as confirmed by analysis of the corresponding Hessian matrices. Frequency analysis also enabled calculation of thermochemical corrections and energies are subsequently reported as zero point energies. D2 and D3 versions of Grimme's dispersion[142,145] were also enabled for certain calculations. Corrections for the basis set superposition error were included for dissociations. The theoretical IR spectra were corrected with a scaling factor of 0.985. The geometries of all optimized structures can be found in the electronic supporting information attached to the current dissertation thesis.

3.4.5 IRMPD measurements

Infrared multiphoton dissociation (IRMPD) spectra were recorded on a Bruker Esquire 3000 ion trap mass spectrometer coupled to the free electron laser at CLIO (Centre Laser Infrarouge Orsay, France). The solutions used for IRMPD measurements were prepared in the same way as those used in the ESI-MS experiments described above. The ions of

interest were generated with an electrospray source, mass selected and stored in the ion trap. The free electron laser operating at 44 MeV electron energy provided light in the 900–2000 cm^{-1} range and with a spectral resolution (full width at half-maximum) in the range of 15–20 cm^{-1}. Fragmentation of the ions was induced by 5–10 laser macropulses of 8 µs directed into the ion trap. The IRMPD spectra are given by dependence of the fragmentation intensities on the wavelength of the IR light. At a given wavelength each point in a raw spectrum is obtained by the evaluation of four mass spectra and each mass spectrum is an average of five measurements. The IRMPD spectra are not corrected for the power of the free-electron laser, which dropped towards high wavenumbers (see Figure 3.6). Experimental spectra for the ions $[(C_6H_6)Ru(OAc)(2\text{-}PhPy)]^+$, $[Cu(OAc)(2\text{-}PhPy)_2]^+$ and $[Pd(OAc)(2\text{-}PhPy)_2]^+$ were recorded in the wavenumber range 900 cm^{-1} to 1800 cm^{-1}. As is routine practice, these are individually compared with theoretical IR spectra calculated by DFT calculations for multiple possible isomers. The comparison allowed identification of the isomer that was isolated and analyzed in the gas phase[51,53,146–148].

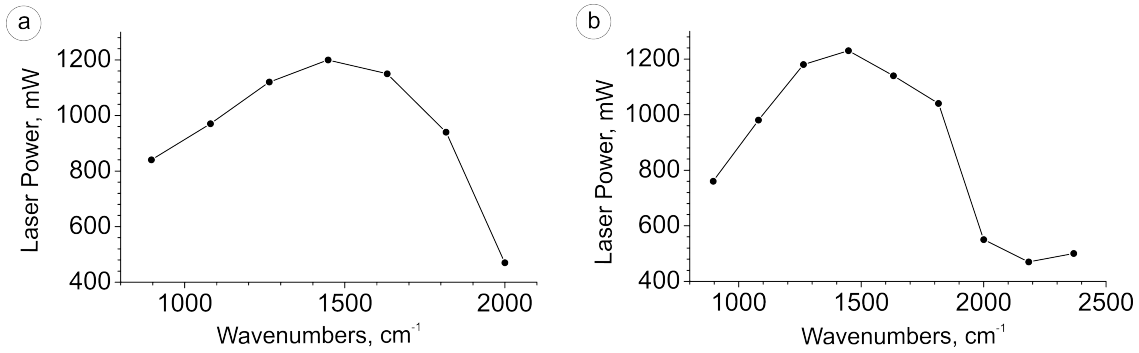

Figure 3.6: Dependence of the free electron laser power on the wavelength during measurement of the IRMPD spectra reported in this thesis shown in a) Figure 4.45a; b) Figure 4.46a and Figure 4.47a

Chapter 4

Results and discussion

This chapter describes results obtained while working towards the current dissertation thesis. Various metal catalyzed reactions and catalytic complexes were chiefly studied in the gas phase. The primary means of the investigation was ESI-MS which was combined with other research techniques (like IRMPD, DFT calculations and EPR spectroscopy). Catalytic species play a large role in the course of organometallic reactions, therefore, in parallel to monitoring by ESI-MS we investigated the behavior of catalytic complexes in more detail.

4.1 Copper acetate speciation

Copper(II) acetate is a cheap catalyst that is frequently used in organic synthesis. For example, it was found to be a cost efficient alternative to expensive palladium catalysts for some cross-coupling reactions[134]. While in the solid state it is present as a dimer $[Cu_2(OAc)_4(H_2O)_2]$ (also called the "paddle-wheel" structure)[149], in solution the situation is different. In aqueous solutions, due to complete hydrolysis of the salt, the solvatized ions $Cu^{2+}(H_2O)_n$ and $AcO^-(H_2O)_m$ are present[150]. Previous electron and chemical ionization mass spectrometry studies on $Cu(OAc)_2$ behavior in organic solvents showed that $Cu(OAc)_2$ prefers to form aggregates[151].

Therefore, prior to investigation of the mechanisms catalyzed by $Cu(OAc)_2$, we decided to study its ESI-MS behavior in methanol and acetonitrile – frequently used solvents in organic synthesis.

4.1.1 ESI-MS studies

We started with the analysis of a methanolic (10^{-3} M) solution of $Cu(OAc)_2$. The positive as well as negative mode ESI-MS experiments revealed the formation of clusters (Figure 4.1) with highest degree of clusterization noted with the positive ESI-MS.

The suggested peak assignments in Figure 4.1 are supported by the subsequent high-resolution MS measurements (on SYNAPT G2, see Section 3.1) and the experiments with deuterated copper acetate (see Figure 4.2). Both positive and negative mode spectra in Figure 4.1 show copper trimers to be the most abundant species.

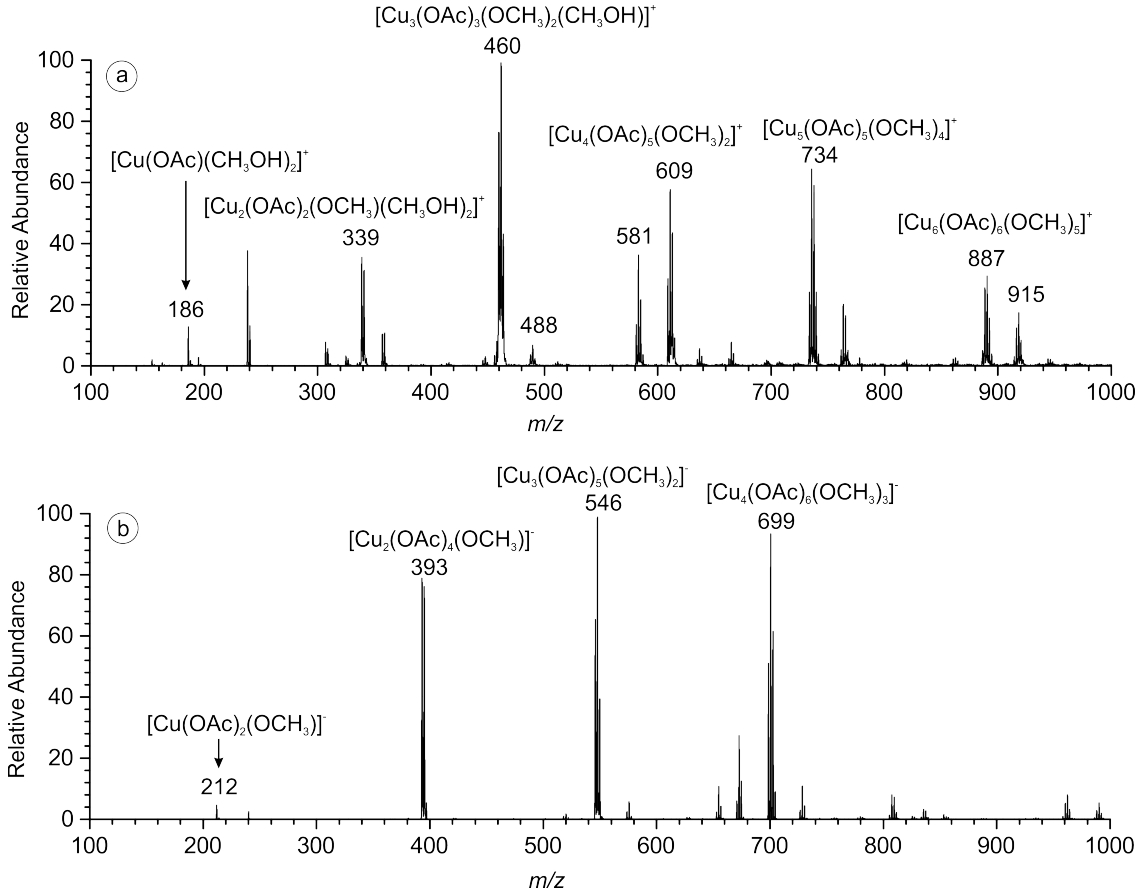

Figure 4.1: ESI mass spectra of a methanolic solution of $Cu(OAc)_2$ (10^{-3} M) in a) positive-ion mode and b) negative-ion mode. Note that the m/z ratios of ions are shown for the ^{63}Cu isotope.

The acetonitrile spectrum also demonstrated a significant clustering ability (Figure 4.3). However, in a big contrast to the methanolic solution, we have observed a large abundance of the monomer copper(I) species. Previous ESI-MS studies on copper salts have shown that the appearance of Cu(I) species while spraying Cu(II) solution can happen either due to reduction of Cu(II) already in solution, or within the electrospray course due

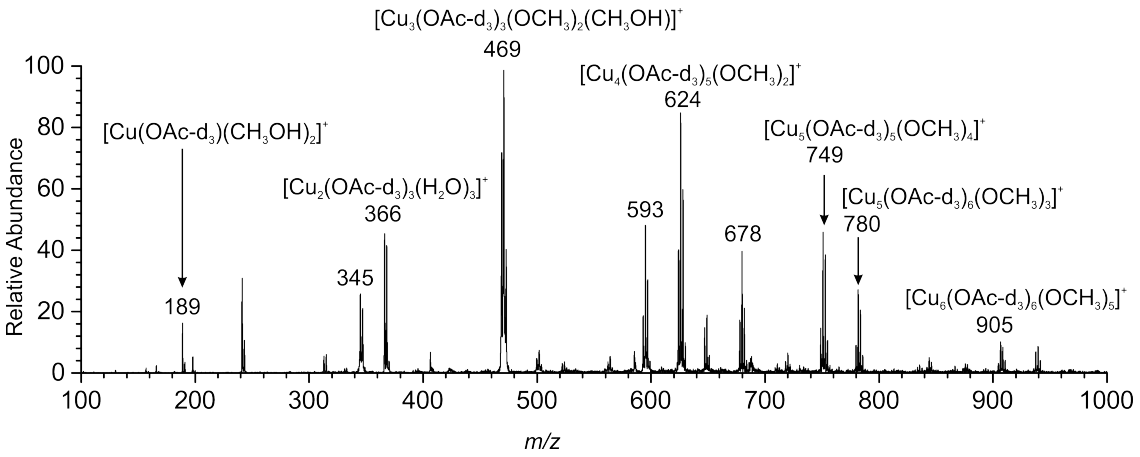

Figure 4.2: Positive ESI mass spectrum of a solution of $Cu(CD_3COO)_2$ (10^{-3} M) in pure methanol. Note that the m/z ratios of ions are shown for the ^{63}Cu isotope.

to the desolvation process[89,152,153]. We believe the latter option to be correct in this case. Thus, during the desolvation process a Cu(II) ion of the form $[Cu(OAc)(CH_3CN)_n]^+$ can lose an acetoxy radical to form a Cu(I) species.

Also, in the case of acetonitrile solutions we did not observed any replacement of the acetato ligands by deprotonated solvent ions (*i.e.* $-CH_2CN$ ligands); this is easily explained by the much lower acidity of acetonitrile compared with that of methanol.

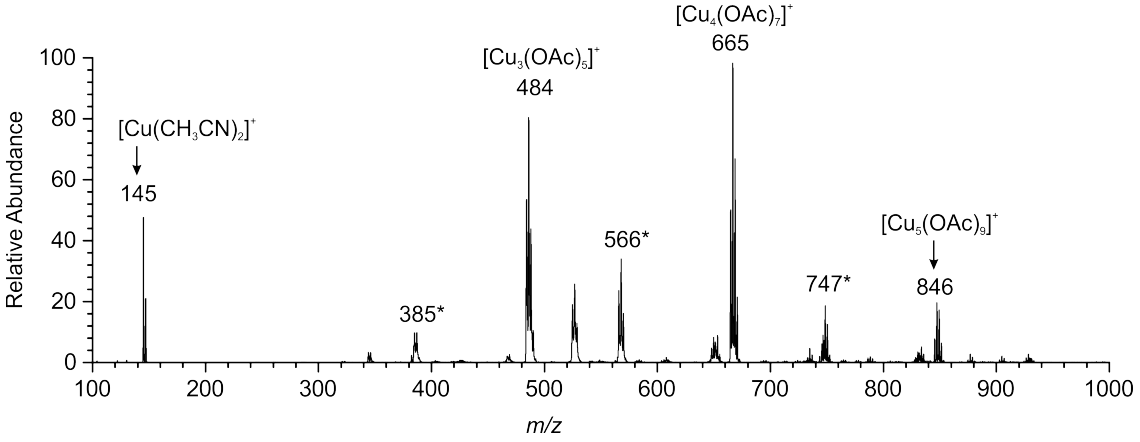

Figure 4.3: Positive-ion ESI mass spectrum of a $Cu(OAc)_2$ solution (2 mM) in acetonitrile. The signals marked with asterisks are due to a sodium contamination of acetonitrile and these correspond to the series sodiated copper(II) acetate clusters, $[Cu_n(OAc)_{2n}Na]^+$. Note that the m/z ratios of ions are shown for the ^{63}Cu isotope.

In order to better understand the process of cluster formation we have analyzed concentration series (Figure 4.4) for both solvents. Even with the limited number of points, we can clearly see a decrease in the abundance of mononuclear species (although more pronounced in the acetonitrile case) with an increase of concentration. In detail, Figure 4.4a shows

that the increasing concentration of salt leads to an increase in the abundances of hexa- and heptanuclear species, whereas the abundance of other multimers slowly decreases. In contrast, the acetonitrile case (Figure 4.4b) does not show an increasing abundance of the largest clusters (n=6).

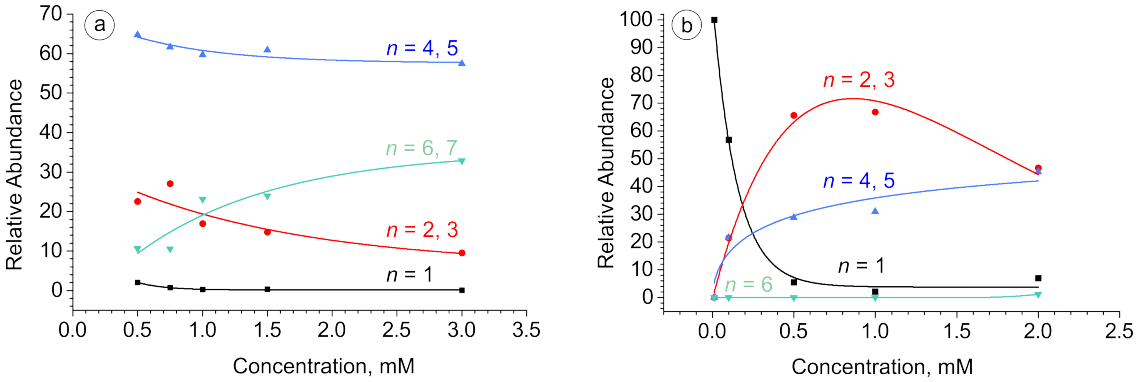

Figure 4.4: Normalized abundances of a) $[Cu_n(OAc)_{2n-1-m}(CH_3O)_m(CH_3OH)_o]^+$ and b) $[Cu_n(OAc)_{2n-1}(CH_3OH)_o]^+$ as a function of the solution concentration in pure a) methanol, b) acetonitrile; n, m and o are variable integers that define cluster size. For the sake of simplicity, the intensities for groups of clusters were summed.

Next, we have studied cluster degradation processes by CID. The clusters observed with ESI-MS of the methanolic $Cu(OAc)_2$ solution were subjected to MS^n analysis in order to establish a connection between various observed species. Figure 4.5 shows CID spectra recorded for some of the investigated clusters and the obtained data are summarized in Scheme 4.1.

Scheme 4.1 shows that two pathways are possible for the fragmentation of copper clusters: degradation or reduction. The question of which of these processes is going to prevail is strongly dependent on the cluster contents and size. Thus, the fragmentation of ions where the number of acetate ligands exceeds the number of methoxy ligands by two or more is dominated by the loss of neutral $Cu(OAc)_2$ (*e.g.* clusters with m/z 1040, and 762). For clusters where the number of acetate ligands is only larger by one, the elimination of $Cu(OAc)_2$ competes with the elimination of $(MeO)_2$ (*e.g.* m/z 609), which is probably formed by the reduction of two Cu(II) centers into Cu(I). The dominance of one of the competing channels depends on the cluster size. For the clusters with $n = 5$ or more, the loss of $Cu(OAc)_2$ prevails, whereas for the smaller clusters only the elimination of $(MeO)_2$ is observed. Therefore, the occurrence of either the reductive or degradation channel depends on the coordination at the copper atoms. The greater the number of acetate ligands (bidentate counterions), the more pronounced is the cluster degradation.

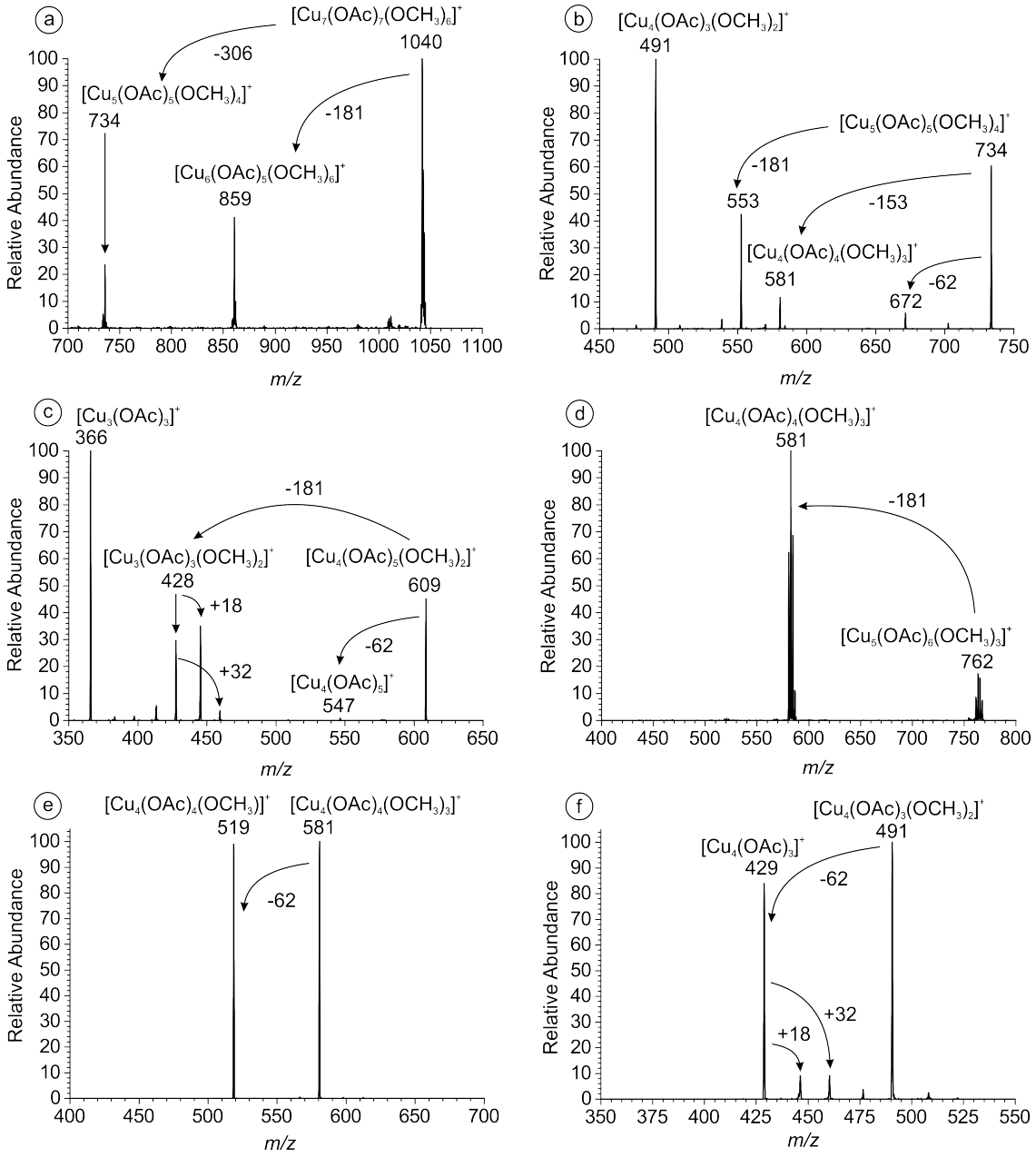

Figure 4.5: CID spectra of mass-selected ions: a) m/z 1040; b) m/z 734; c) m/z 609; d) m/z 762; e) m/z 581; f) m/z 491.

The reduction processes are feasible for the smaller clusters with the greater number of monodentate methoxy ligands. Of special notice is a sequential degradation/reduction process occurring during CID of large clusters. That is, formation of m/z 734 during CID of m/z 1040 most likely resulting from subsequent degradation of m/z 859; next, formation of m/z 366 during CID of m/z 609 resulting from subsequent reduction of m/z 428; formation of m/z 491 during CID of m/z 734 resulting subsequent degradation of m/z 553.

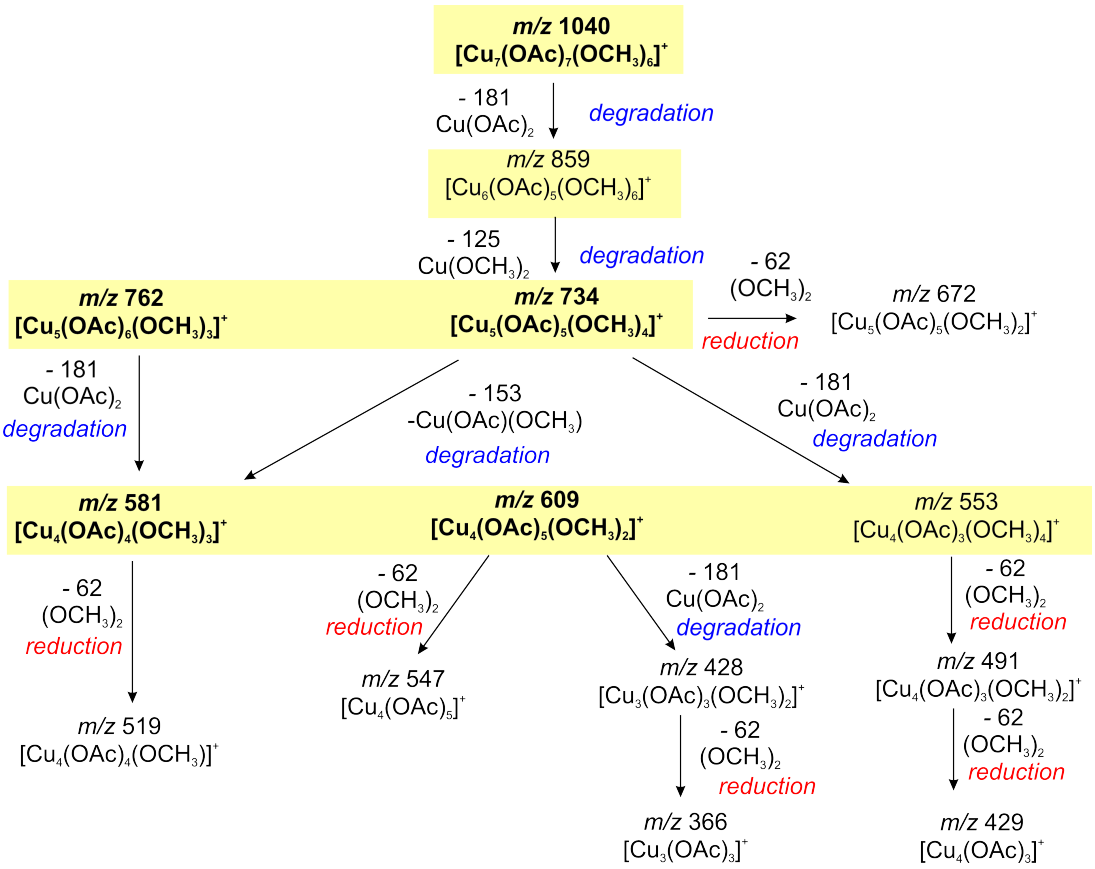

Scheme 4.1: Cluster degradation studied with CID.

During our experiments we experienced some difficulties with the reproducibility of our results. It turned out to be connected with small amount of moisture present in the inlet system of the mass spectrometer from previous experiments. To our surprise we have observed that small amounts of water dramatically increased the abundance of the mononuclear clusters, while at the same time, the abundance of larger clusters decreased. Figure 4.6 shows the comparison of the positive-ion mode spectra obtained for a pure methanolic $Cu(OAc)_2$ (10^{-3} M) solution, and a 10^{-3} M $Cu(OAc)_2$ solution with the addition of 0.5 vol% water. Therefore we decided to study this water effect in greater detail. To this end, we have prepared several mixtures of $Cu(OAc)_2$ in either methanol or acetonitrile with different amounts of water added to the solution.

While working with methanol solutions, we faced problems with signal assignments with larger amounts of added water. To this end, while at 2 vol% added water only a few peaks correspond to the impurities (*e.g.* at m/z 409 and 459, see Figure 4.7) , at 10 vol% added water - the majority of the peaks were from impurities. Thus, ions similar to those formed during the analysis of a 10^{-4} M solution of $Cu(OAc)_2$ in pure methanol

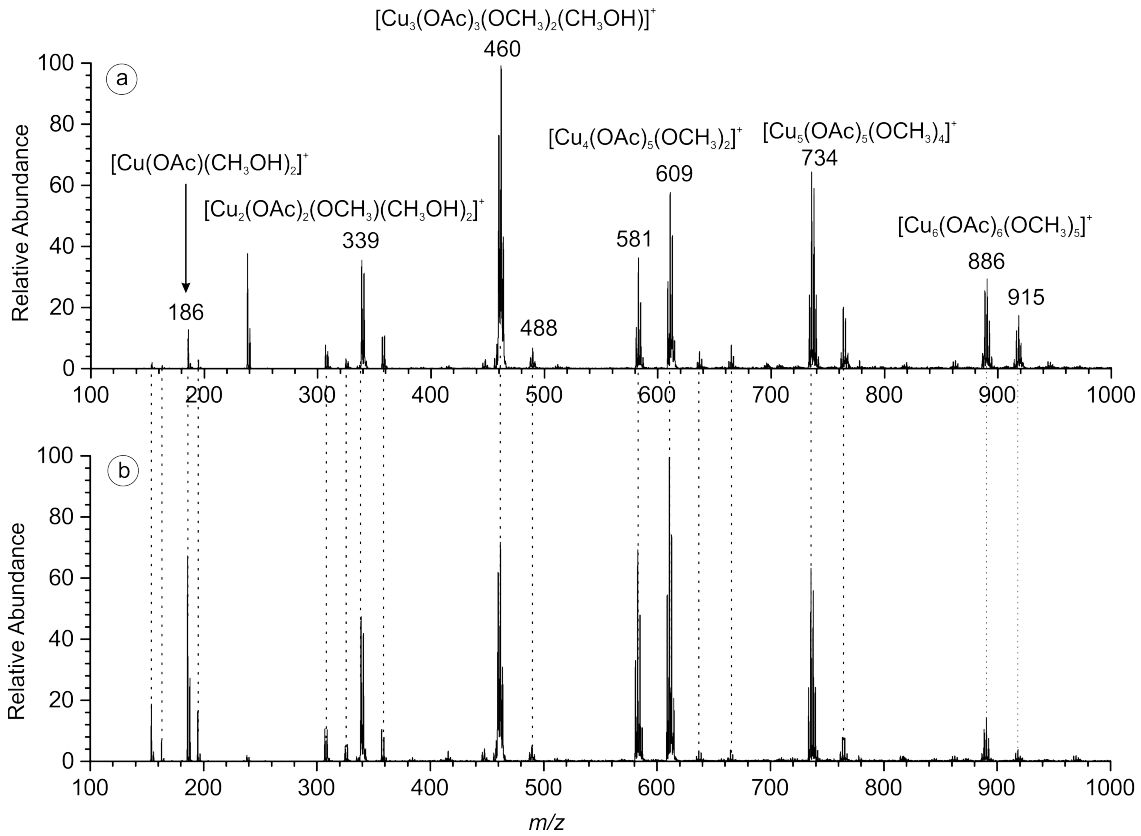

Figure 4.6: ESI mass spectra of a $Cu(OAc)_2$ (10^{-3} M) solution in a) pure methanol and b) after addition of 0.5 vol% of water to methanol. Note that the m/z ratios of ions are shown for ^{63}Cu isotope.

(see Figure 3.1) were formed (*e.g.* m/z 597 which was observed in both cases). This effect might be explained by the changes in solubility of $Cu(OAc)_2$ and its impurities in the methanol-water mixture. It is likely that with increasing amount of water, the solubility of the impurities increases which is reflected in their increased abundances.

The same effect was observed during analysis of acetonitrile solutions. Figure 4.8 shows the speciation of $Cu(OAc)_2$ in acetonitrile after the addition of 1 vol% and 3 vol% water, respectively.

We have therefore restricted ourselves to the quantitative analysis of those Cu-clusters that were present in the spectra with pure solvent (Figure 4.9). To this end, Figure 4.9a shows that in a pure methanol solution mononuclear species only correspond to a few percent of the total signal abundance. After the addition of 5 vol% of water the mononuclear species become the most abundant in the spectrum. A similar, although not as dramatic effect is observed for the acetonitrile solution (Figure 4.9b).

Interestingly enough, although we observed a few copper complexes bearing a water

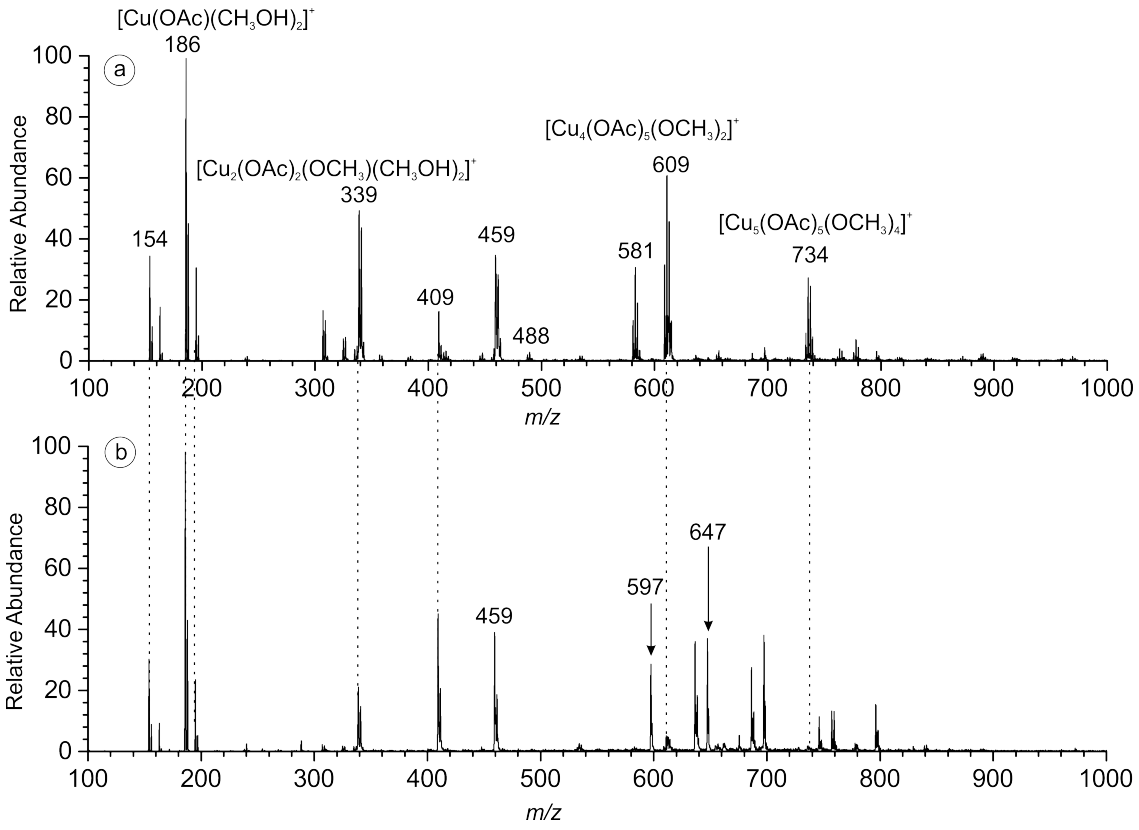

Figure 4.7: ESI mass spectra of a methanolic $Cu(OAc)_2$ (10^{-3} M) solution after a) addition of 2 vol% of water and b) addition of 10 vol% of water . Note that the m/z ratios of ions are shown for the ^{63}Cu isotope.

ligand while spraying the solutions from pure methanol or acetonotrile, we have not seen any increase in their appearance during analysis of the mixtures with higher water contents. This effect can be caused by the discrimination of $[CuL(H_2O)]^{n+}$ ions by other ionic species present in solution as was explained in Section 1.4.

Overall, the observed water effect can have at least two explanations: either cluster breakage happens in solution, or it is an artifact of the ESI-MS process. In order to distinguish between these options we have performed a series of solution-phase experiments.

4.1.2 Solubility determination of $Cu(OAc)_2$ in the methanol-water mixture with different amount of water

The solubility was determined for eleven solutions with different amounts of added water (Table 4.1). As $Cu(OAc)_2$ is hygroscopic, an elemental analysis of the samples (including the $Cu(OAc)_2$ starting material) was carried out, the percentage of absorbed water was determined and taken into account during the solubility calculations. The results

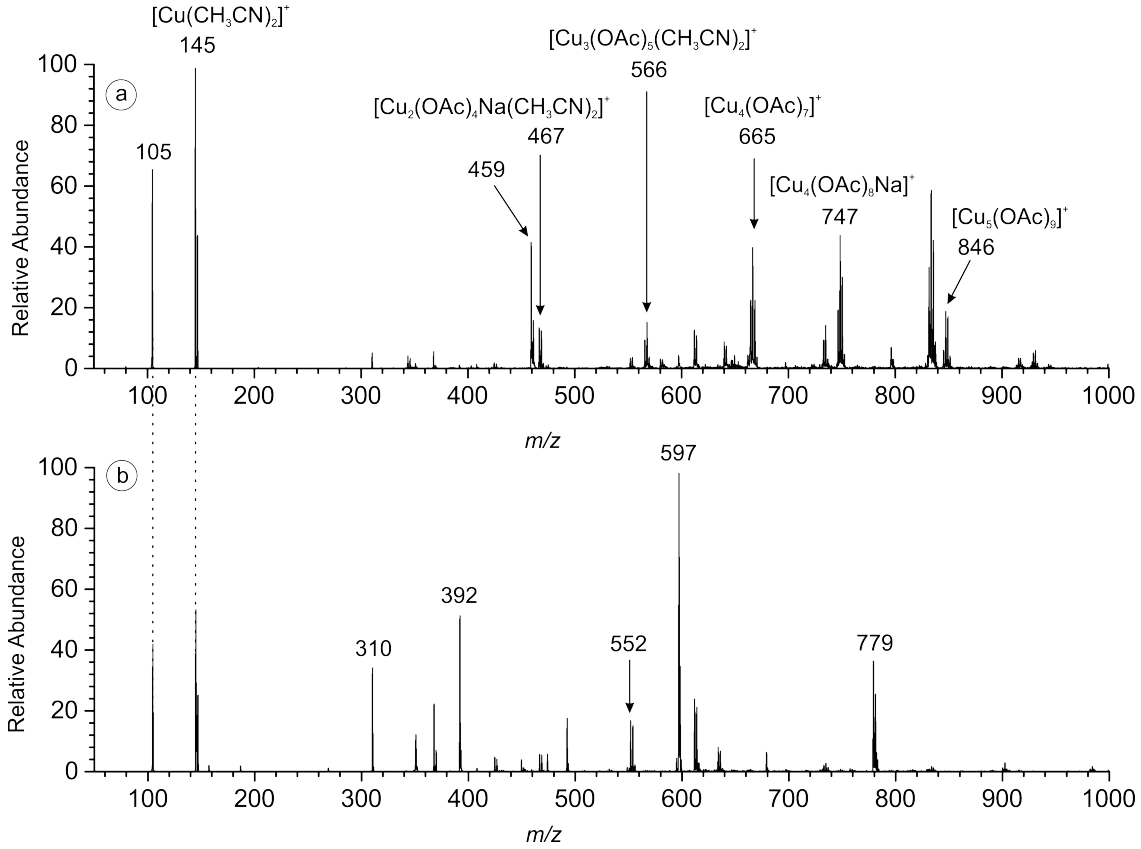

Figure 4.8: ESI mass spectra of a $Cu(OAc)_2$ (10^{-3} M) solution in acetonitrile after a) addition of 1 vol% of water and b) addition of 3 vol% of water . Note that the m/z ratios of ions are shown for the ^{63}Cu isotope.

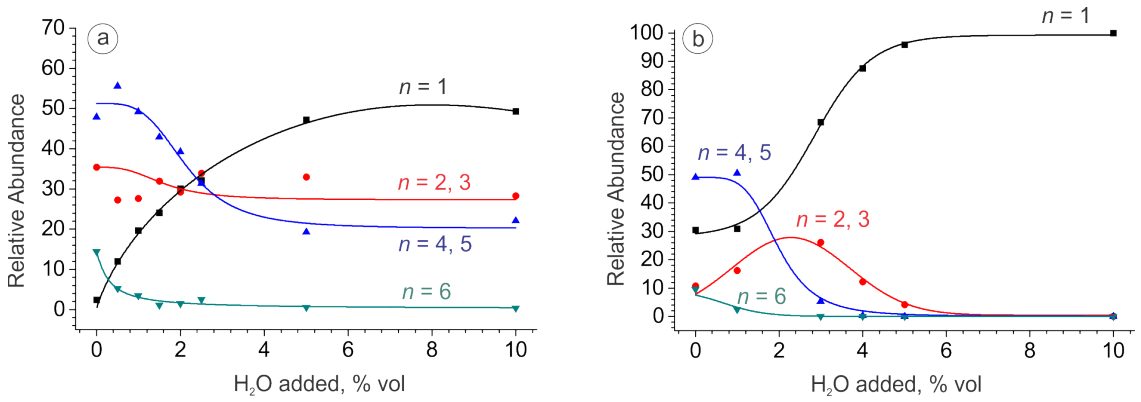

Figure 4.9: Normalized abundances of a) $[Cu_n(OAc)_{2n-1-m}(CH_3O)_m(CH_3OH)_o]^+$ and b) $[Cu_n(OAc)_{2n-1}(CH_3CN)_o]^+$ cations, where n, m and o are variable integers that define cluster size, as a function of the water content in the solution of $Cu(OAc)_2$ (1 mM) in a) methanol and b) acetonitrile.

are presented in Table 4.1 and Figure 4.10.

It can be seen that solubility of $Cu(OAc)_2$ in methanol increases with increasing amounts of water, added to the solution.

Table 4.1: Data for the solubility determination of $Cu(OAc)_2$ in the methanol-water mixture with the different amounts of water.

H_2O, %	$m_{dry\ residue}$, g	formula	$m_{Cu(OAc)_2}$	S, g/(100 mL)
0	0.06	$Cu(OAc)_2$. 0.5 H_2O	0.05	0.54
0.5	0.08	$Cu(OAc)_2$. H_2O	0.07	0.69
1	0.08	$Cu(OAc)_2$. H_2O	0.07	0.69
1.5	0.04	$Cu(OAc)_2$. H_2O	0.03	0.67
2	0.04	$Cu(OAc)_2$. H_2O	0.04	0.74
2.5	0.03	$Cu(OAc)_2$. H_2O	0.03	0.57
3	0.04	$Cu(OAc)_2$. H_2O	0.04	0.78
5	0.05	$Cu(OAc)_2$. H_2O	0.04	0.86
7	0.07	$Cu(OAc)_2$. H_2O	0.07	1.29
10	0.09	$Cu(OAc)_2$. H_2O	0.08	1.61
15	0.10	$Cu(OAc)_2$. H_2O	0.10	2.00

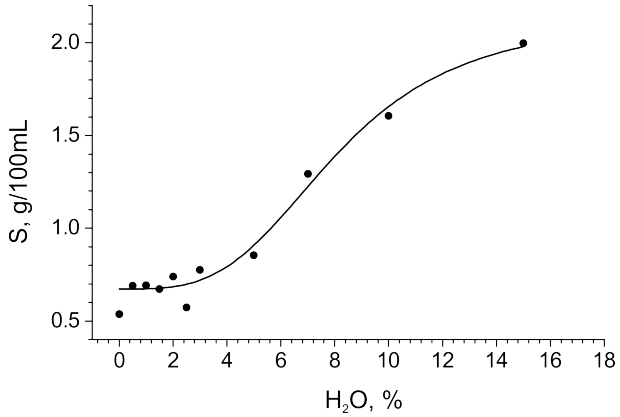

Figure 4.10: Dependence of the determined solubility for each sample on the amount of added H_2O.

4.1.3 EPR measurements

Additional EPR measurements were performed to complement our solubility studies. Figure 4.11 shows that the pure methanol solution of copper(II) acetate is almost EPR inactive, producing a small EPR signal. However, addition of water increases the signal, with the EPR parameters (A and g) remaining unchanged. This suggests that the signal growth corresponds to the concentration increase of monomers in the solution. The dependence of EPR signal growth on the amount of water is linear (Figure 4.11b) and shows that at 10 vol% of added water 80% of copper acetate become EPR active. These observations suggest that the mononuclear species are formed after the addition of water. We also assume that, similar to the solid paddle-wheel dimer, high order $[Cu(OAc)_2]_n$ species

exhibit antiferromagnetic properties when n is even, or produce a small EPR signal when n is odd. Therefore, these results support the hypothesis of water leading to cluster breakage in solution.

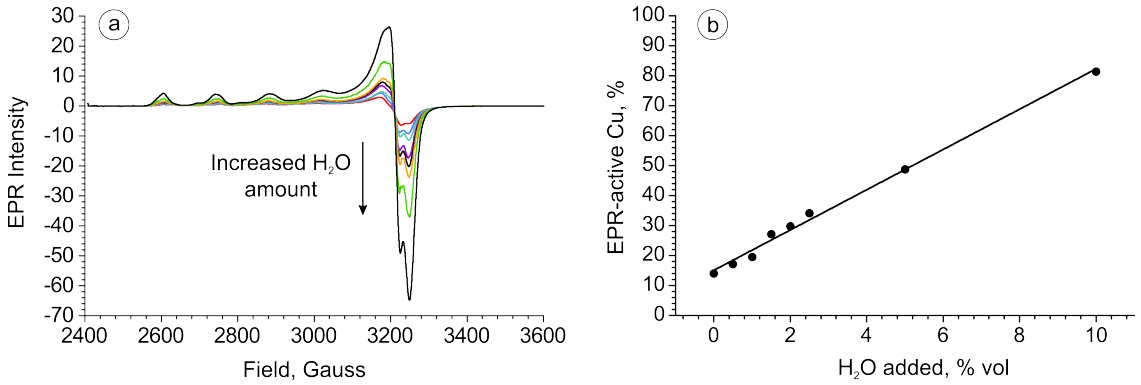

Figure 4.11: a) EPR spectra of $Cu(OAc)_2$ solutions, 3.75 mM in methanol with variable water content. b) Fraction of EPR-active Cu(II) species in $Cu(OAc)_2$ solutions in methanol with variable water content, obtained *via* double integration of spectra relative to an external standard.

Direct comparison of the EPR and ESI dependencies shows that they do not agree quantitatively. This is easily explained as ESI does not accurately sample concentration in the solution (as was explained in detail in Section 1.4). While obvious correlation exists between ESI mass spectra and solution properties, the match is not 1:1. We suggest that during the ESI process, methanol is preferentially evaporated from the droplets, (due to its lower boiling point) and the water concentration in the droplets increases. Thus, ESI-MS experiments reflect a somewhat larger water content than the one in the solution.

In general, the results show that the addition of small quantities of water significantly influences the speciation of copper(II) acetate in organic solvents. The speciation is shifted towards the formation of monomers, suppressing the formation of larger clusters. We believe that this finding is important for future mechanistic studies of various copper(II) acetate catalyzed reactions.

4.2 Investigation of copper catalyzed aerobic cross coupling of thiol esters and arylboronic acids

In 2007 Villalobos *et al.* found a convenient method for the synthesis of non-symmetrical ketones (Scheme 4.2a)[134]. The reaction is a modification of the Liebeskind–Šrogl coupling reaction[154]. All of the previous synthetic procedures based on the cross-coupling of thioor-

ganic compounds and boronic acids required the presence of a palladium catalyst and a stoichiometric amount of a Cu(I) salt[155–161]. However, the procedure suggested by Villalobos *et al.* only uses a copper catalyst, which makes the reaction much more financially appealing (Scheme 4.2a). The authors reasoning behind the procedure's design was that the second equivalent of boronic acid, added to the reaction mixture, would recover the copper catalyst from the Cu-SR intermediate, and therefore a second catalytic species would not be needed for the reaction to proceed. This was indeed the case, however a concrete mechanism of the reaction was not clear: the authors suggested several possible pathways, including transmetallation, ligand exchange, or the involvement of oxidated copper clusters[162].

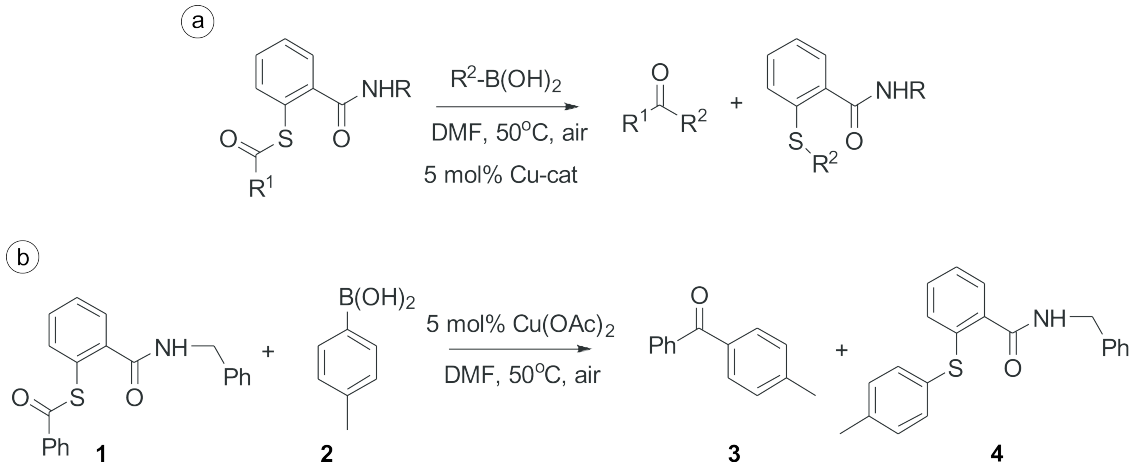

Scheme 4.2: a) Aerobic coupling of thiol esters and boronic acids and b) specific reaction investigated here.

Therefore we decided to investigate the mechanism using ESI-MS and tandem mass spectrometry, for the particular reaction described in Scheme 4.2b. We began with the off-line monitoring, investigating the reaction mixture in steps, starting from less complicated systems. Subsequent addition of the reagents and comparison of the spectra obtained for different mixtures allowed easier identification of reaction intermediates.

4.2.1 Off-line monitoring *via* ESI-MS

Accordingly, we investigated the behavior of thiol ester **1** solution in methanol with ESI-MS. The positive mass spectrum (Figure 4.12) shows a large abundance of singly charged sodiated complexes (m/z 370 and 717), and also signals of doubly charged magnesium, calcium and iron complexes (m/z 532.6, 540.7 and 548.5, respectively).

Next, we studied the behavior of 4-tolylboronic acid in methanol. Negative ESI mass

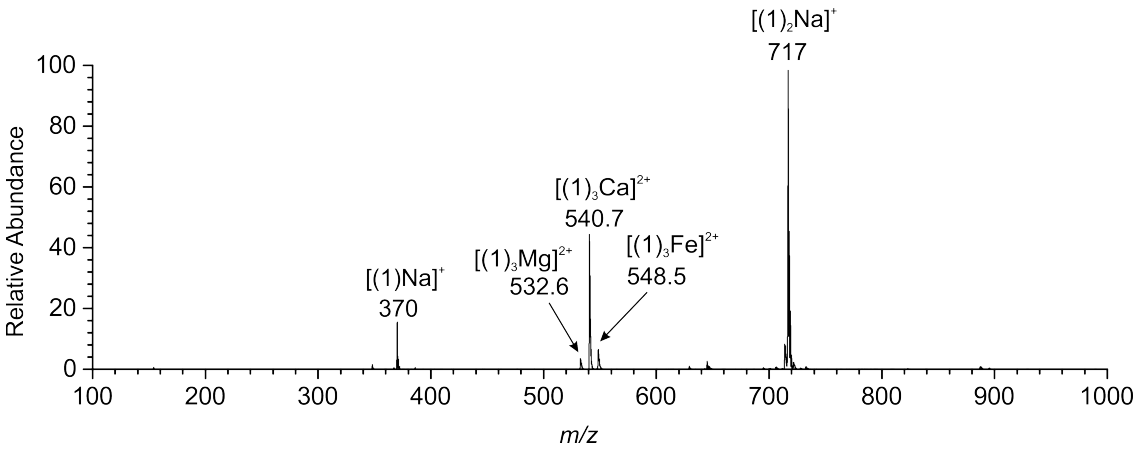

Figure 4.12: Positive-mode ESI-MS of the solution of thiol ester **1** in methanol.

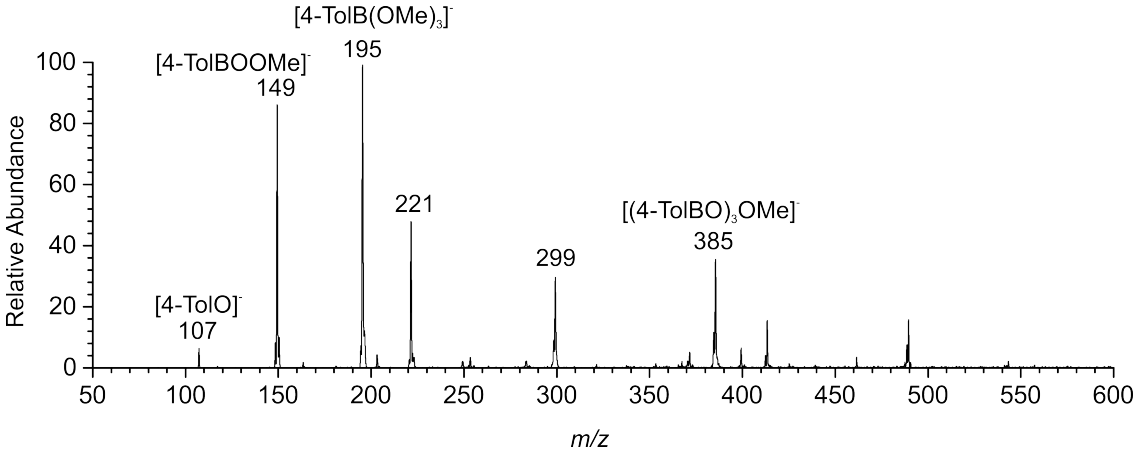

Figure 4.13: Negative-mode ESI-MS of 4-tolylboronic acid in methanol.

spectrum of the boronic acid solution shows the formation of 4-tolylboronic esters at *m/z* 149, 195 and 385 (Figure 4.13). Possible mechanisms for the ester anions formation are shown in Scheme 4.3. We have also observed the [4-TolO]$^-$ anion at *m/z* 107, which could be formed upon deborylation of an ester. Similar observations were reported by Wang *et al.*[163] in their detailed study of the ESI-MS behavior of different boronic acids. They have also accounted for the deborylation mechanism leading to the formation of [4-TolO]$^-$ anions. As the peaks at *m/z* 221 and 299 do not correspond to the isotope pattern associated with the boron atom, we consider them to be the result of impurities.

The mixture of 4-tolylboronic acid with $Cu(OAc)_2$ in methanol was also investigated. Neither positive nor negative ESI mass spectra show the formation of any species containing both boron and copper atoms. Most likely, it is caused by the fact that under these conditions boronic acid rapidly reacts with methanol leading to *p*-methylanisol as is shown for boronic esters (Scheme 4.4)[164]. We have also tested mixtures containing phenyl-

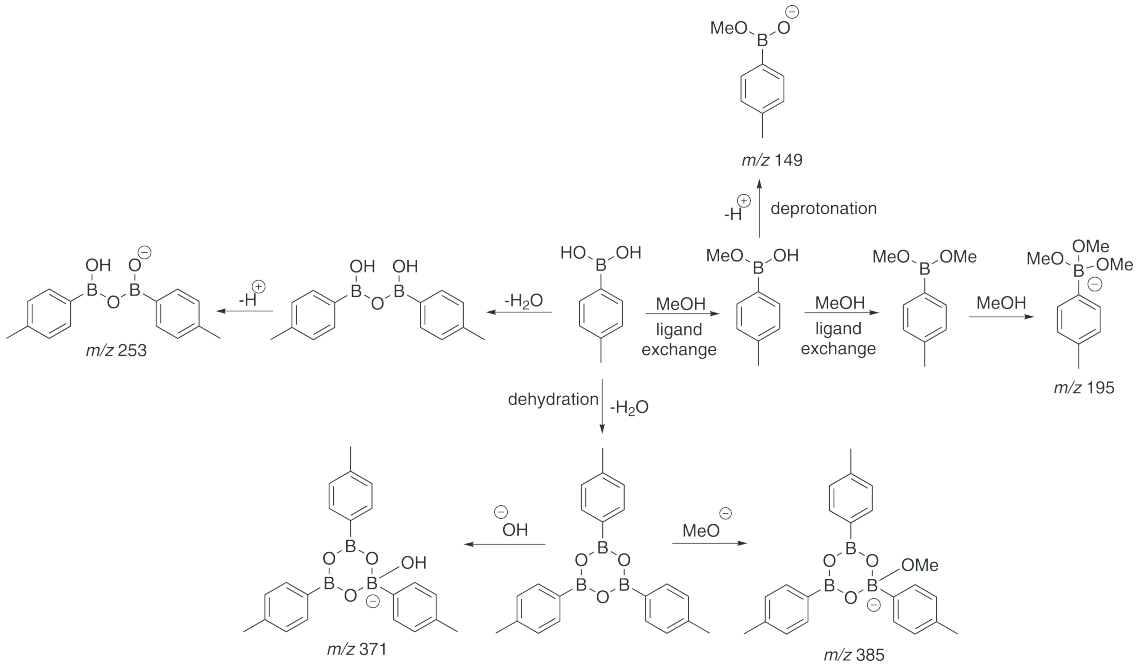

Scheme 4.3: The proposed formation mechanisms for some of the observed ions present in the negative ESI-MS of the 4-tolylboronic acid solution.

boronic acid and copper acetate. Nevertheless, in either case we could not successfully assign most of the observed peaks. High resolution MS measurements (performed on a SYNAPT G2 instrument) also have not helped with the peak assignments. This makes the $Cu(OAc)_2$ - boronic acid case an interesting one, and more studies should be carried out in order to understand the ESI-MS behavior of these mixtures. One potential study would implement the synthesis of a boronic acid bearing a charged tag. Another option would involve experiments carried out under inert gas atmosphere (glovebox coupled to a mass spectrometer).

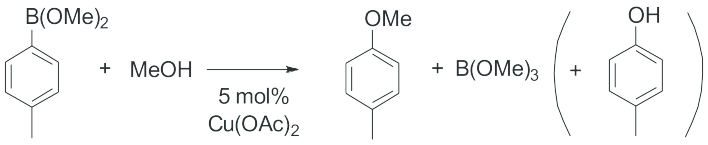

Scheme 4.4: Cu-catalyzed methoxylation of tolylboronic ester.

Next we analyzed the mixture of thiol ester **1** with $Cu(OAc)_2$. The spectrum in Figure 4.14a shows the formation of the complexes with both copper(I) and copper(II) species with the starting thiol ester **1** at m/z 410, 469 and 757. These complexes were subjected to MS/MS analysis for further characterization.

CID analysis of the complex at m/z 469 (Figure 4.15) showed the elimination of a mixed anhydride of benzoic and acetic acid (*e.g.* Ph-CO-O-CO-CH_3). The fragment ion at m/z

305 (assigned as $[(\text{int})\text{Cu}]^+$) was also observed in the source spectrum (see Figure 4.14). We found that the appearance energy for $[(\text{int})\text{Cu}]^+$ corresponds to 121 ± 3 kJ·mol^{-1}. The structure of the ion at m/z 305 was checked in MS^n experiments. MS^2 spectra of m/z 305 from the source spectrum were compared with MS^3 spectra of the fragment m/z 305 by activation of m/z 469. The spectra appeared to be identical. Also, the most pronounced fragmentation channel of m/z 305 is the elimination of a CO molecule (see Figure 4.16a). Therefore we suggest that the intermediate has a cyclic structure as shown in Figure 4.15.

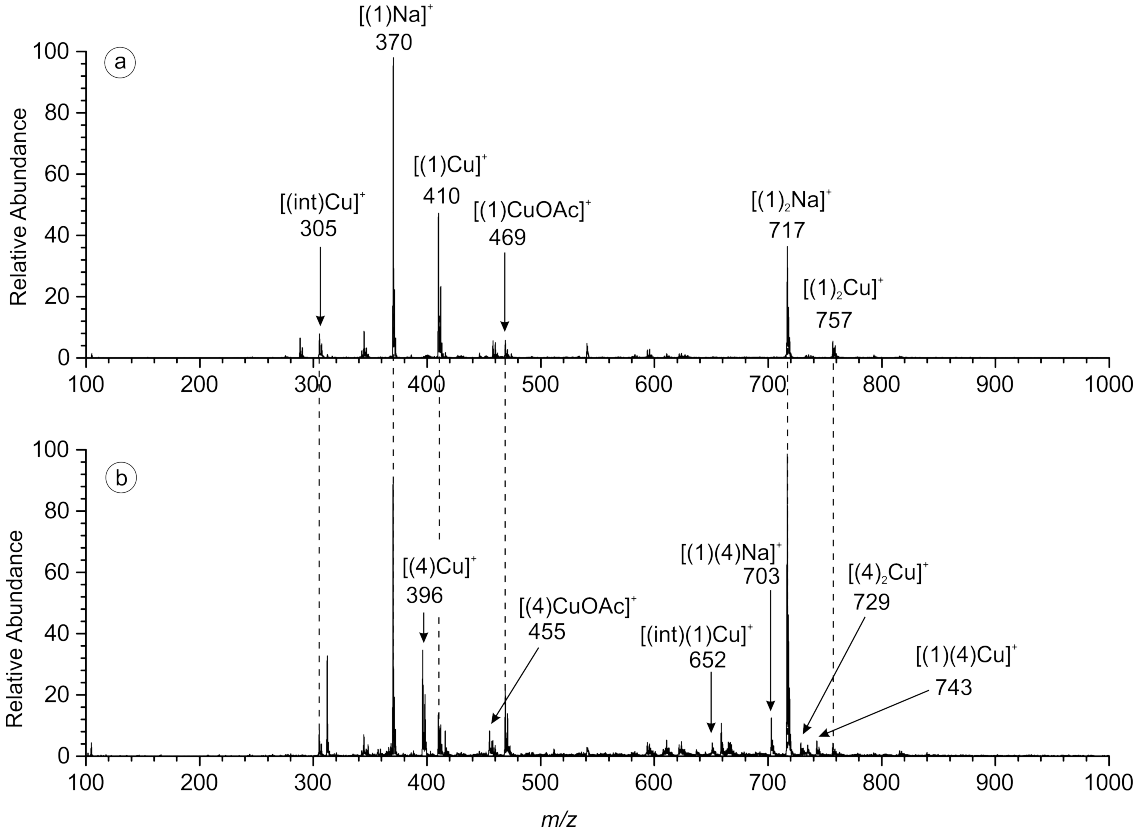

Figure 4.14: Positive mode ESI mass spectra of a) the mixture of thiol ester **1** and $Cu(OAc)_2$ in methanol; b) the mixture of thiol ester **1**, 4-tolylboronic acid and $Cu(OAc)_2$ in methanol, taken 1h after mixing the reagents at room temperature.

Next we have analyzed the mixture of all the reaction components (thiol ester **1**, 4-tolylboronic acid and $Cu(OAc)_2$) in methanol. In addition to the previously observed complexes with Cu(I/II) and the starting thiol **1**, Figure 4.14b shows the formation of the complexes of the product **4** with Cu(I/II) and sodiated complexes of **4**.

Although the signals containing product **4** were observed in the recorded spectra, we have not observed any complexes of ketone **3** in the mixture. Although ketone complexes are usually easily detectable with ESI-MS, we suppose that their absence can be explained

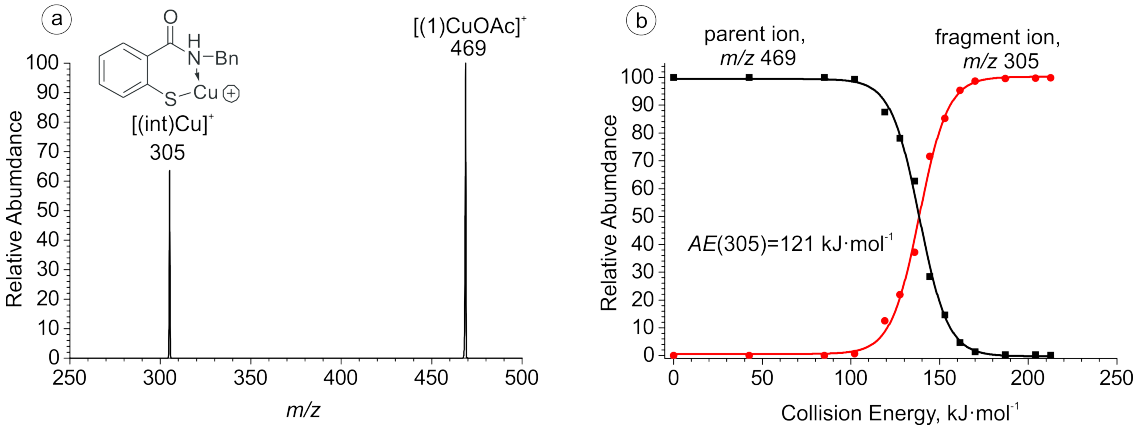

Figure 4.15: a) CID spectrum of the mass-selected m/z 469 and b) its breakdown curve.

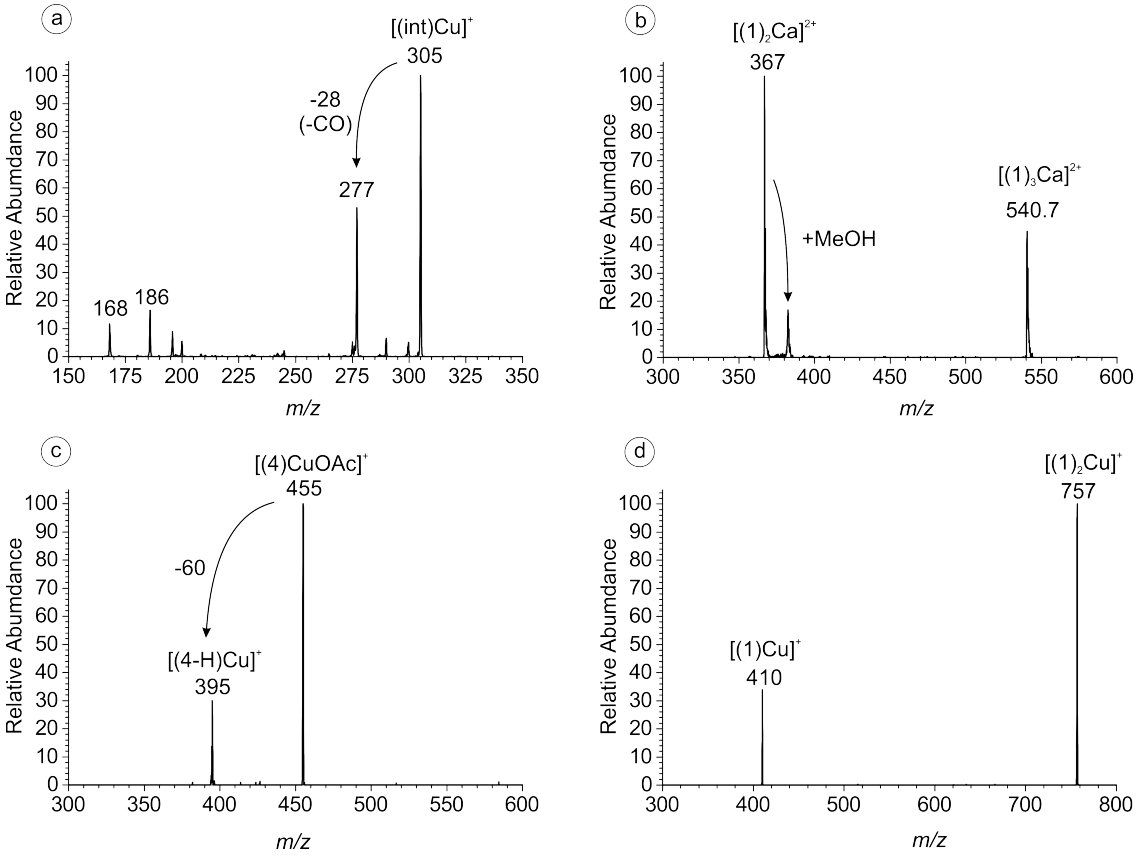

Figure 4.16: CID spectra of mass-selected ions: a) m/z 305, b) m/z 540.7, c) m/z 455 and d) m/z 757.

by the discrimination effect from the better ligand **4**.

Especially puzzling were the CID spectra obtained for Cu(I) complexes of the thiol ester **1** and product **4** (m/z 410 and 396, respectively). CID of m/z 410 showed the loss of 122, which could correspond to the elimination of benzoic acid. Therefore we suggested a fragmentation pathway shown in Figure 4.17 which explains the formation of ion at m/z

288. Although this fragmentation is interesting on its own we have not studied it in more detail (for example, the reactivity of m/z 288 could have been checked in ion-molecule reactions). It should also be noted that neither the structure of m/z 410, nor that of m/z 288 was confirmed by a complementary spectroscopic technique (*e.g.* IRMPD) and therefore should be considered as purely hypothetical.

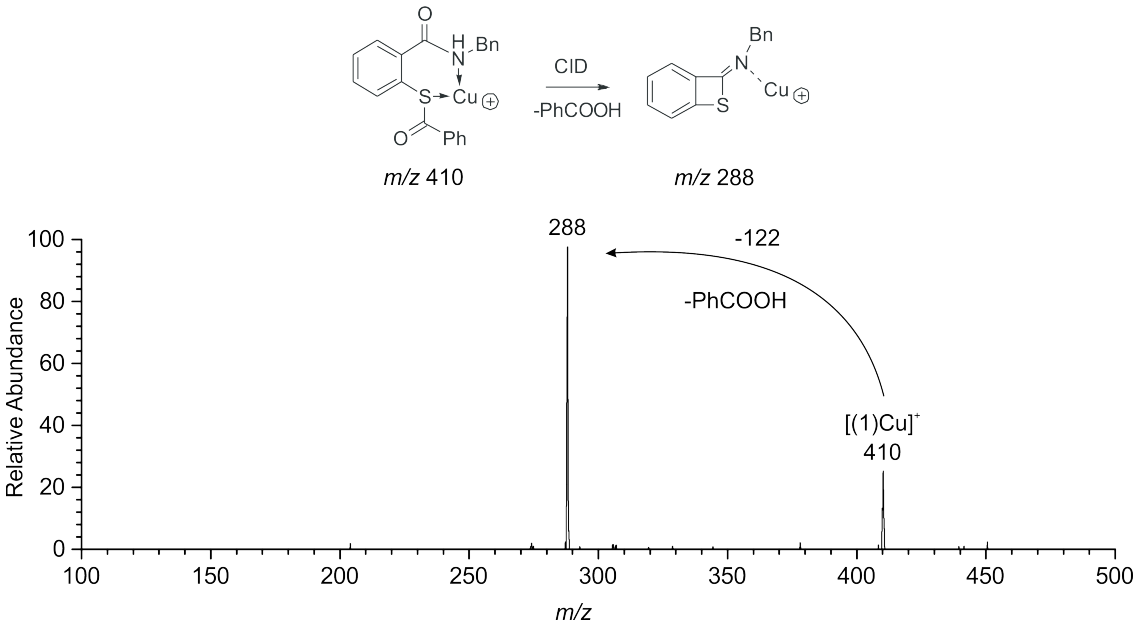

Figure 4.17: CID spectrum of the mass-selected m/z 410 and a possible scheme describing its fragmentation pathway.

Similarly, CID of m/z 396 also showed the formation of ion at m/z 288. In addition, the main fragmentation pathway led to the elimination of water molecule and formation of m/z 378. We suggest that these ions are created similarly to the m/z 410 case, and the hypothetical scheme together with CID spectrum of m/z 396 are shown in Figure 4.18.

In order to further support our assignments of various ions we have performed the experiments with the methyl-derivative of thiol ester **1** (further noted as **1**'). The spectrum of its mixture with 4-tolylboronic acid and $Cu(OAc)_2$ in methanol is shown in Figure 4.19. It can be seen that all of the peaks that contained thiol ester **1** moiety now lay 14 m/z higher.

We have also analyzed reaction mixture containing thiol ester **1**, phenylboronic acid and copper catalyst in methanol. Figure 4.20 shows the formation of product ion at m/z 382.

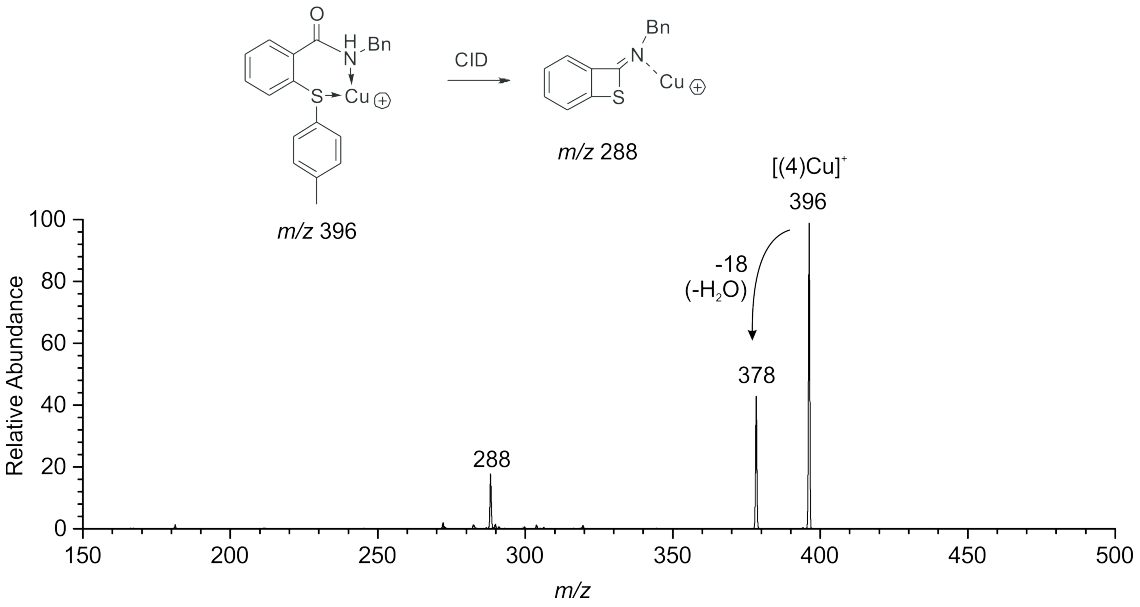

Figure 4.18: CID spectrum of the mass-selected m/z 396 and a possible scheme describing its fragmentation pathway.

4.2.2 Experiments with N-benzyl-2-mercaptobenzamide

In order to test the rationality as to whether the intermediate complex $[(\text{int})\text{Cu}]^+$ is participating in the reaction mechanism (possible pathway shown in Scheme 4.5), we have carried out experiments with N-benzyl-2-mercaptobenzamide (thiol **5**) in order to simulate the conditions for the formation of the complex at m/z 305.

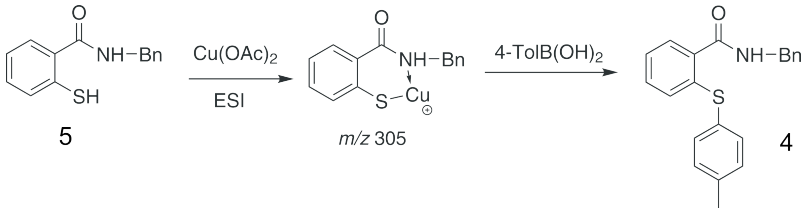

Scheme 4.5: Proposed reactivity scheme of **5** with 4-tolylboronic acid investigated here.

Figure 4.21a shows the positive ESI mass spectrum obtained for the mixture of **5** and copper acetate (1:1) in methanol. Although we have not observed the formation of the desired intermediate, we have detected the ion with m/z 304 which can be associated with the oxidated **5**-Cu complex. Nevertheless, the spectrum of the mixture of all three components (**5**, 4-tolylboronic acid and $Cu(OAc)_2$, Figure 4.21b) shows that product **4** is formed. Therefore we believe that the complex at m/z 305 is not formed during the course of the reaction and rather is produced during the ESI process.

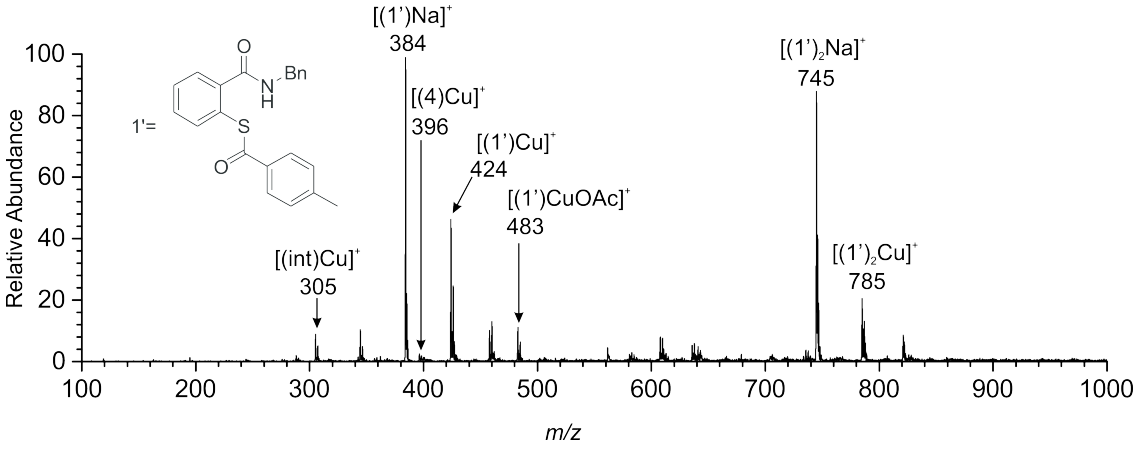

Figure 4.19: Positive-mode ESI mass spectrum of the mixture of thiol ester derivative (**1**'), 4-tolylboronic acid and $Cu(OAc)_2$ in MeOH.

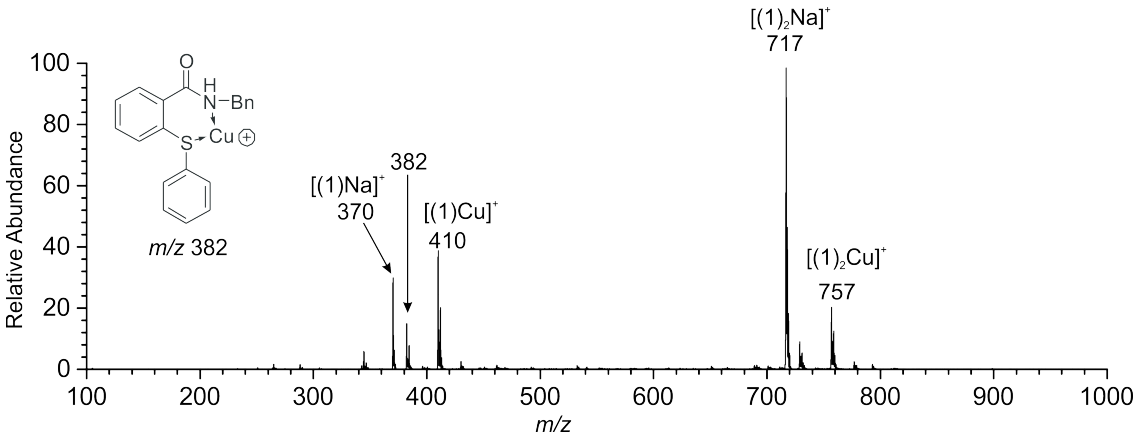

Figure 4.20: Positive-mode ESI mass spectrum of the mixture of thiol ester **1**, phenylboronic acid and $Cu(OAc)_2$ in MeOH.

4.2.3 On-line monitoring and kinetic studies

We next performed on-line monitoring of the reaction mixture under identical conditions as was used for synthesis (*e.g* 5 mol% of $Cu(OAc)_2$, 1 eq. of thiol ester **1**, 2.5 eq. of 4-tolylboronic acid, DMF). Monitoring was performed by repetitive sampling of portions of the reaction mixture at given time intervals. The small portions of the reaction mixture (20 μL) were diluted in MeOH (2 mL) and the resulting solutions sprayed into the mass spectrometer. Table 4.2 shows the intensity changes for the most abundant ions in the spectrum over time. The product complex could already be detected 15 minutes after the beginning of the reaction. Due to the small amounts of copper catalyst in the reaction mixture and the dominance of sodiated complexes, the detection of Cu complexes was very limited. Figure 4.22 shows examples of spectra obtained during monitoring procedure. We

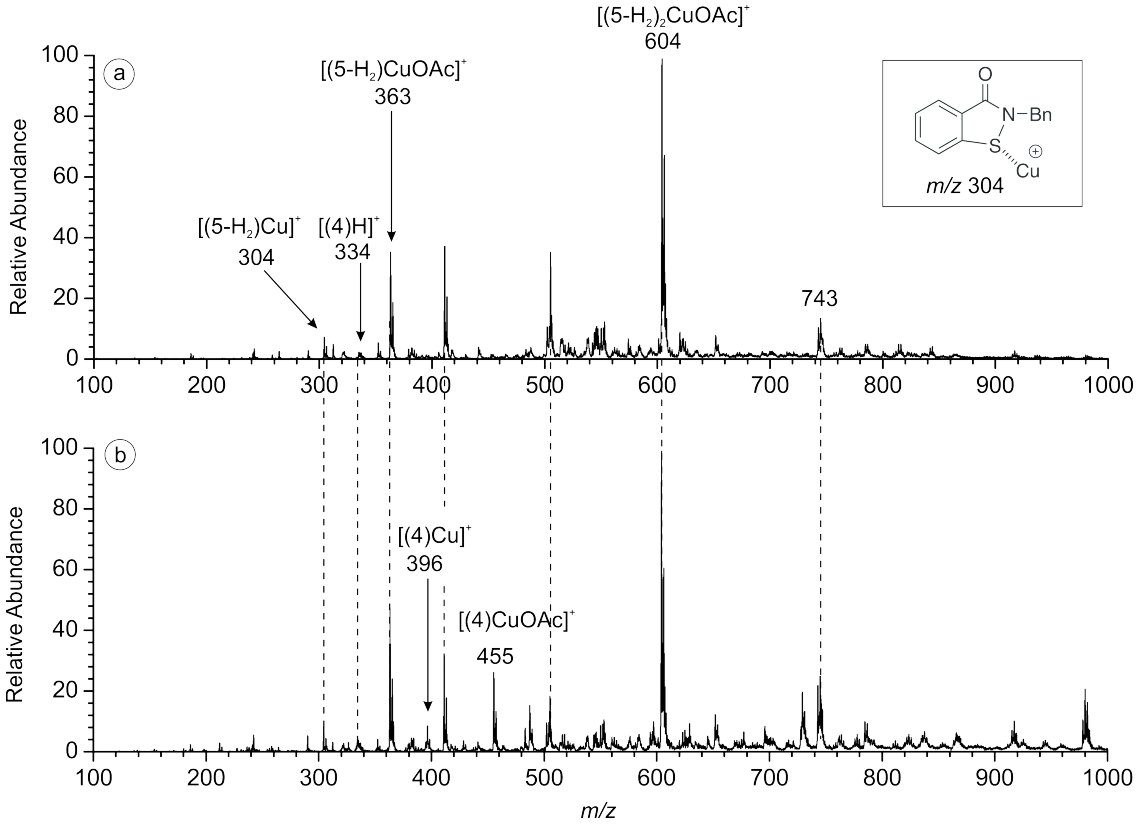

Figure 4.21: Positive-mode ESI mass spectra of a) the mixture of **5** and $Cu(OAc)_2$ in MeOH and b) the mixture of **5**, 4-tolylboronic acid and $Cu(OAc)_2$ in MeOH.

note in passing that only part of the observed peaks was possible to assign, leaving aside complexes formed within the range of m/z 400–680.

Table 4.2: Relative intensities of the major complexes observed in the reaction mixture performed in DMF at 50 °C.

Time, h	m/z 356	m/z 370	m/z 396	m/z 689	m/z 703	m/z 717
	$[(\mathbf{4})\mathrm{Na}]^+$	$[(\mathbf{1})\mathrm{Na}]^+$	$[(\mathbf{4})\mathrm{Cu}]^+$	$[(\mathbf{4})_2\mathrm{Na}]^+$	$[(\mathbf{1})(\mathbf{4})\mathrm{Na}]^+$	$[(\mathbf{1})_2\mathrm{Na}]^+$
0.3	0.3	19.6	0.0	0.6	10.5	69.0
0.5	0.6	14.3	0.4	1.4	13.1	70.2
1.0	0.7	10.3	0.3	2.6	21.4	64.7
2.0	0.9	7.9	0.4	7.8	31.3	51.7
3.3	1.7	7.7	1.1	11.3	38.2	40.0
5.3	2.0	5.0	0.0	21.2	43.9	27.9
6.7	3.3	5.7	0.0	26.6	42.3	22.1
8.2	3.7	5.6	0.0	32.2	42.0	16.5
23.0	4.7	0.7	0.0	71.9	20.8	1.9

On-line monitoring was performed at different temperatures (40, 50, 60 and 80 °C) re-

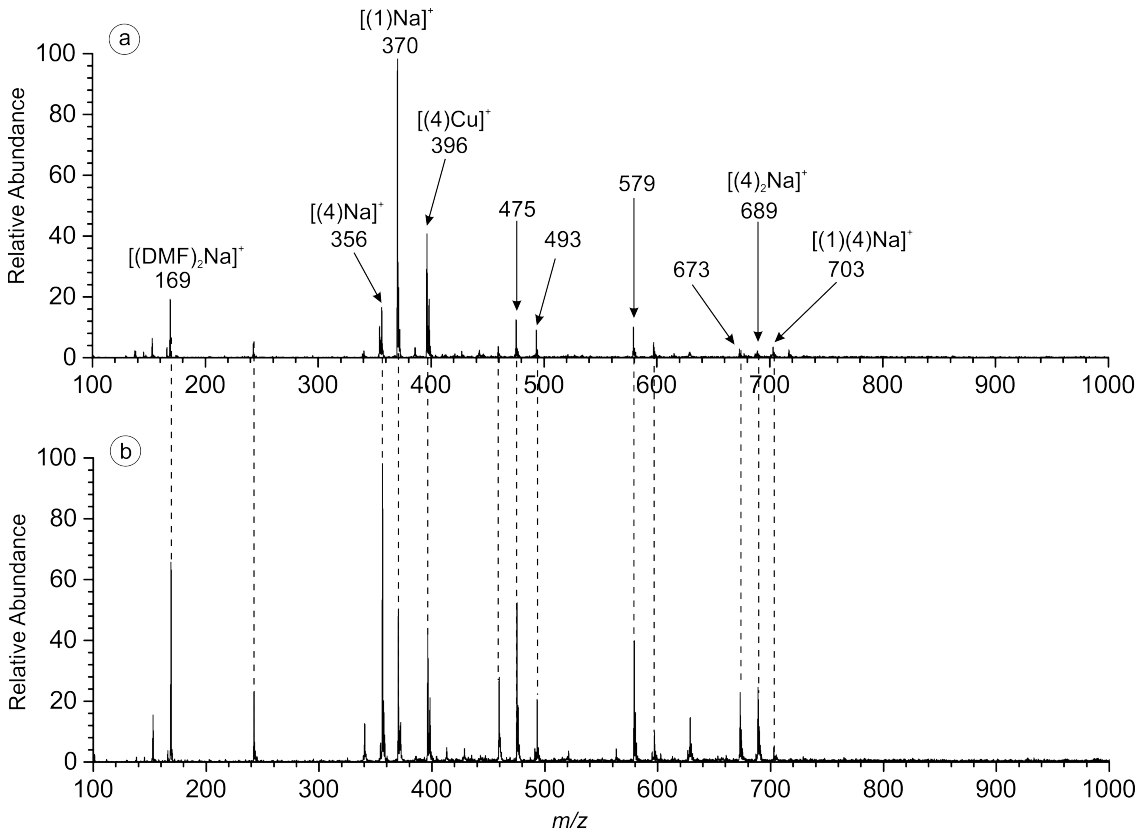

Figure 4.22: The ESI mass spectrum of the reaction mixture obtained a) 1,5 hours and b) 6 hours after the addition of Cu-catalyst to a solution of thiol ester **1** and 4-tolylboronic acid at 60 °C.

sulting in the creation of kinetic curves (see Figure 4.23). Fractional abundances of the reactant complexes were determined as the sum of the abundances of $[(\mathbf{1})\mathrm{Na}]^+$, $[(\mathbf{1})(\mathbf{4})\mathrm{Na}]^+$, and $[(\mathbf{1})_2\mathrm{Na}]^+$ divided by the sum of the abundances of all complexes in Table 4.2. Similarly, fractional abundances of the product complexes were determined as the sum of the abundances of $[(\mathbf{4})\mathrm{Na}]^+$, $[(\mathbf{1})(\mathbf{4})\mathrm{Na}]^+$ and $[(\mathbf{4})_2\mathrm{Na}]^+$ divided by the sum of the abundances of all complexes in Table 4.2.

Treating the reaction as pseudo first order gives the linear dependencies shown in Figure 4.24 (we note however that experiments at 60 and 80 °C showed linear dependence only during the first few hours), and the rate constant can be determined from the slope of the resulting lines. Linearization of the kinetic curves shown in Figure 4.23 was done with the equation 4.1. The final data obtained upon linearization are presented in Table 4.4. It can be seen that increasing the temperature of the reaction increases its rate. The temperature dependency of the rate constants can be further investigated using the Arrhenius and Eyring equations (4.2, 4.3) for the determination of thermodynamic parameters of the

reaction. Analysis of the Arrhenius equation gave us E_a = 81 ± 5 kJ·mol^{-1}. The Eyring equation gave an activation enthalpy of 76 ± 5 kJ·mol^{-1}, and an activation entropy -100 ± 5 J·mol^{-1}·K^{-1}. The Gibbs energy according to equation 4.4 was found to be 103 ± 5 kJ·mol^{-1} at 298 K.

$$\frac{dI}{dt} = k(T) \cdot [1]^n \cdot [2]^m \tag{4.1}$$

$$ln(k) = -\frac{E_a}{R} \cdot \frac{1}{T} + ln(A) \tag{4.2}$$

$$ln\frac{k}{T} = \frac{-\triangle H^{\ddagger}}{R} \cdot \frac{1}{T} + ln\frac{k_B}{h} + \frac{\triangle S^{\ddagger}}{R} \tag{4.3}$$

$$\triangle G^{\ddagger}(T) = \triangle H^{\ddagger} - \frac{T \cdot \triangle S^{\ddagger}}{1000} \tag{4.4}$$

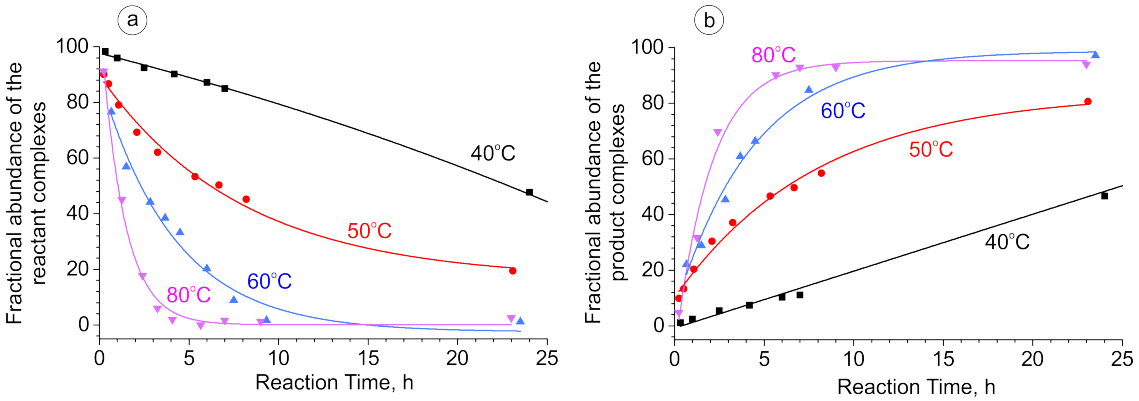

Figure 4.23: Dependence of the abundances of a) reagent and b) product complexes on the reaction time at different temperatures.

Table 4.3: Data obtained from linearization.

t, °C	T, K	1/T, K^{-1}	k, L·mol^{-1}·s^{-1}·10^5	ln(k)
40	313.15	0.0032	0.85	-11.39
50	323.15	0.0031	1.81	-9.40
60	333.15	0.0030	8.04	-9.02
80	353.15	0.0028	27.80	-8.23

In conclusion, although ESI-MS experiments did not resolve the mechanism of the investigated reaction, we profited from the formation of highly abundant sodiated complexes. These species allowed us to follow the kinetics of the investigated reaction. The kinetic

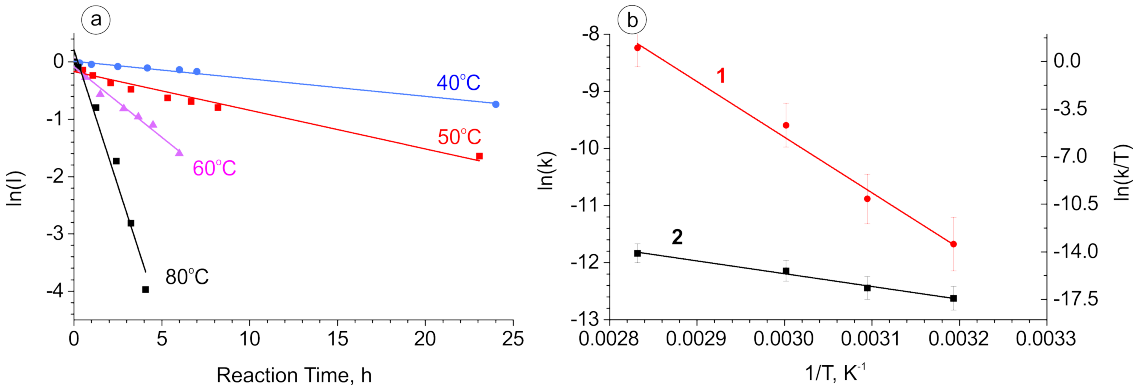

Figure 4.24: a) Logarithmic plot of the abundance of reactant complexes in dependence of the reaction time at different temperatures; b) Arrhenius (1) and Eyring (2) plots for thiol ester **1** coupling with 4-tolylboronic acid. The resulting values were determined from two independent measurements (I represents the sum of the abundances of $[(\mathbf{1})\mathrm{Na}]^+$, $[(\mathbf{1})(\mathbf{4})\mathrm{Na}]^+$, and $[(\mathbf{1})_2\mathrm{Na}]^+$ divided by the sum of the abundances of all complexes in Table 4.2).

experiments enabled determination of the rate constants and thermodynamic parameters.

4.3 Coordination and bond activation in complexes of regioisomeric phenylpyridines with nickel(II)

Pyridine derivatives are a common class ligands in organometallic chemistry. Thus, phenylpyridine (PhPy) isomers, especially 2-phenylpyridine, are frequently used in the mechanistic studies of metal-catalyzed C-H activation[165–174].

It was shown that a metal catalyst can coordinate to the nitrogen atom of 2-phenylpyridine and facilitate activation of the C-H bond in the position 2' of the phenyl ring (so-called directed C-H activation)[175,176]. The mechanism of directed C-H activation was extensively studied in solution and was shown to be strongly dependent on the nature of metal catalyst, its ligands, substrate and solvent[177]. The general mechanism of directed cyclometalation is described in Scheme 4.6. The reaction starts with the coordination of an atom Y with a lone electron pair to a metal atom. The cyclization proceeds *via* agostic interactions and C-H activation resulting in bidentate coordination of a metal with the carbon and Y atoms[178].

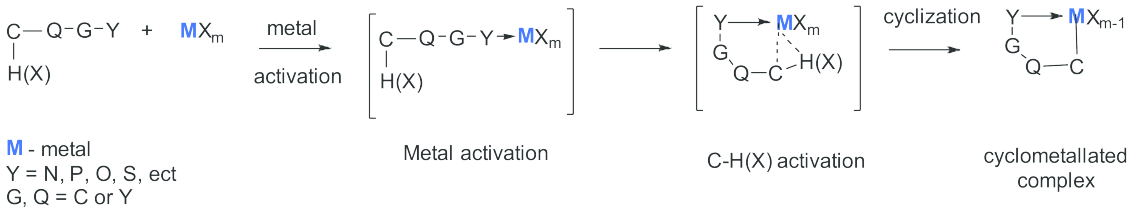

Scheme 4.6: General mechanistic scheme for cyclometalation reactions.

In order to account for other PhPy regioisomers, we have theoretically compared the bond dissociation energies of the phenyl- C-H bonds of 2- 3- and 4-PhPy (Scheme 4.7). It can be seen that the C-H bond in the 2' position of 2-PhPy is only by a small extent weaker than those in the 3- and 4- regioisomers. Therefore, it cannot be considered "pre-activated" in the 2-PhPy molecule. However, once the metal is coordinated to the nitrogen atom, the metal is in close proximity to the 2' position of the phenyl ring, making the C-H bond in this position easily activated.

In this project we decided to investigate dilute mixtures of 2,- 3- and 4-phenylpyridines with nickel(II) chloride in methanol/water (1:1) by means of ESI-MS, IMS and tandem mass spectrometry.

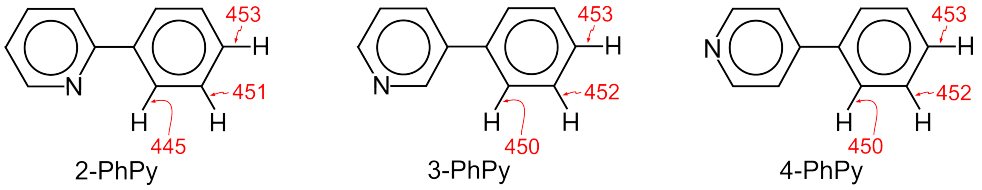

Scheme 4.7: Computed C—H bond dissociation energies (M06/def2-TZVPP//B3LYP-D3/def2-SVP, in kJ·mol^{-1} at 0 K) of the phenyl substituent in 2-PhPy, 3-PhPy and 4-PhPy.

4.3.1 ESI-MS studies

Positive ESI mass spectra revealed the formation of two types of nickel complex: dications $[Ni(PhPy)_n]^{2+}$ and monocations $[Ni(PhPy)_m]^+$, where n and m are dependent on the electrospray conditions[67,68,89,179]. A typical mass spectrum obtained for such a solution is shown in Figure 4.25.

For all of the investigated phenylpyridines, the major signal observed at m/z 156 corresponds to the protonated phenylpyridine ($[PhPyH]^+$). For clarity, further discussion is focused on the spectra recorded within the range 200 - 700 m/z. When this is taken into account, the major signal for the 2-PhPy solution appears at m/z 367 ($[Ni(2\text{-}PhPy)_2\text{-}H]^+$, Table 4.4). On the other hand, this activated complex is absent in the case of both 3- and

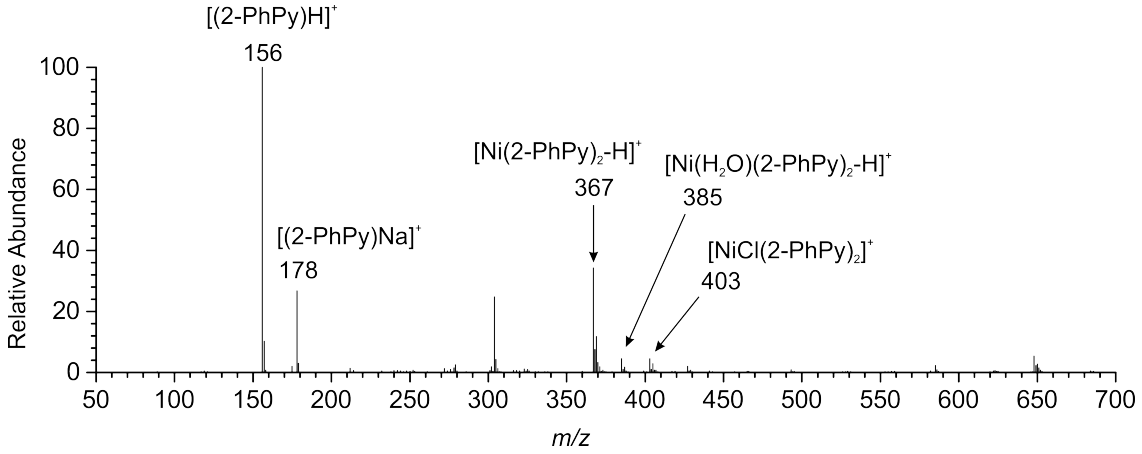

Figure 4.25: Positive ESI-MS of the solution of $NiCl_2$ and 2-PhPy in $MeOH/H_2O$ recorded with a cone voltage $U_C = 10$ V.

4-PhPy solutions. These observations suggest a strong preference for the C-H activation of 2-PhPy. For 3- and 4-PhPy a dication at m/z 339 is the most abundant ion, whereas it is hardly seen in the case of 2-PhPy due to large steric demands.

Table 4.4: Relative intensities of the major nickel complexes in the ESI mass spectra of $NiCl_2$- PhPy solutions with the isomeric PhPys ($\sim 3\times10^{-4}$ M) in water/methanol (1:1). The column $[Ni(PhPy)_3]^{2+}$ includes a signal for $[Ni(H_2O)(PhPy)_3]^{2+}$, which is formed by association of the $[Ni(PhPy)_3]^{2+}$ dication with water.

	$[Ni(PhPy)_3]^{2+}$	$[Ni(PhPy)_4]^{2+}$	$[Ni(PhPy)_2$- $H]^+$	$[NiCl(PhPy)_2]^+$	$[NiCl(PhPy)_3]^+$
	m/z 261.5	m/z 339	m/z 367	m/z 403	m/z 558
2-PhPy	2	<1	100	30	2
3-PhPy	2	100	<0.1	<1	6
4-PhPy	12	100	<0.1	3	10

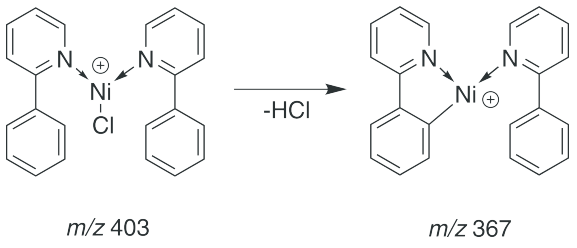

Scheme 4.8: C-H activation reaction we study here.

As is implied in Scheme 4.8, the ion at m/z 403 might be the precursor for the activated complex $[Ni(2\text{-}PhPy)_2\text{-}H]^+$. In order to test this possibility we have isolated the corresponding ion in the collision cell and subjected it to the CID experiments. Figure 4.26 shows that two fragmentation channels are present for the ion at m/z 403: either

elimination of HCl (which corresponds to collision induced C-H activation) or elimination of the neutral 2-PhPy ligand. We experimentally found that the HCl elimination channel, although being the minor one, requires 160 ± 5 kJ·mol^{-1} of energy, whereas the elimination of 2-PhPy needs about 10 kJ·mol^{-1} more.

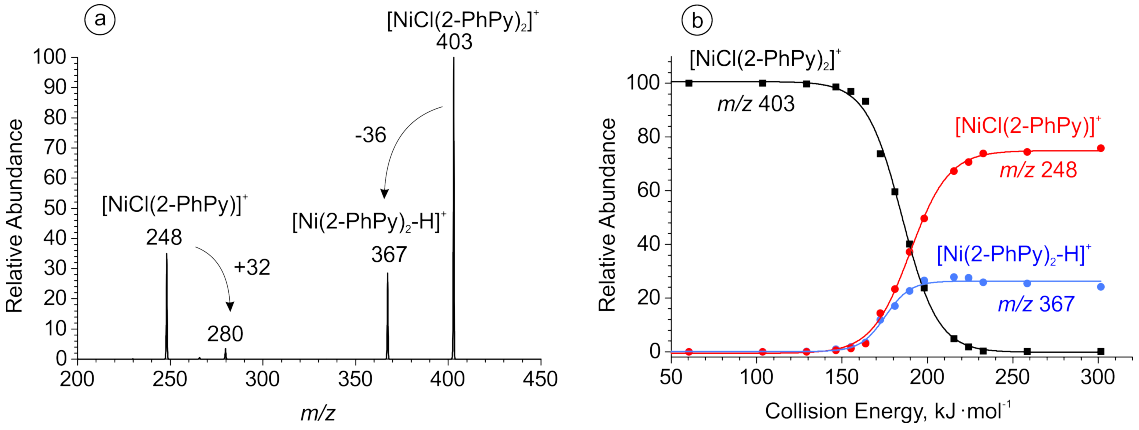

Figure 4.26: a) CID spectrum of the mass-selected [NiCl(2-PhPy)$_2$]$^+$ (m/z = 403) leading to two fragmentation channels: the loss of HCl (product ion with m/z = 367) and 2-PhPy (product ion with m/z = 248); b) its breakdown curve.

The AEs of both losses are significantly lower in energy for the case of 2-PhPy, consistent with the observations described in Table 4.4. The smaller ligand binding energy for the 2-PhPy complex is associated with bigger steric hindrance and thus with more facile C-H activation channel.

Table 4.5: Fragment ions appearance energies (in kJ·mol^{-1}) and relative fragment intensities upon CID of mass-selected m/z 403 and m/z 332.

	[NiCl(PhPy)$_2$]$^+$		[NiCl(PhPy)(D$_5$-Py)]$^+$			
	-HCl	-PhPy	-HCl	-DCl	-(D$_5$-Py)	-PhPy
2-PhPy	160 (27%)	170 (73%)	160 (6%)	-	160 (94%)	-
3-PhPy	215 (13%)	215 (87%)	200 (4%)	205 (1%)	205 (91%)	205 (4%)
4-PhPy	220 (5%)	230 (95%)	200 (1%)	215 (<1%)	205 (98%)	215 (1%)

Likewise, mixed complexes of the form [NiCl(PhPy)(D$_5$-Py)]$^+$were generated in the gas phase and their CID behavior was compared to that of the [NiCl(PhPy)$_2$]$^+$ complexes. As an example, the CID spectrum obtained for [NiCl(2-PhPy)(D$_5$-Py)]$^+$and its breakdown curve is shown in Figure 4.27

The ligand loss AEs were again found to be the smallest in case of 2-PhPy complexes. In all of the mixed complexes the elimination of the perdeuterated pyridine ligand prevails. As the PhPy ligand has an extra coordination site to the nickel atom (benzene ring), in

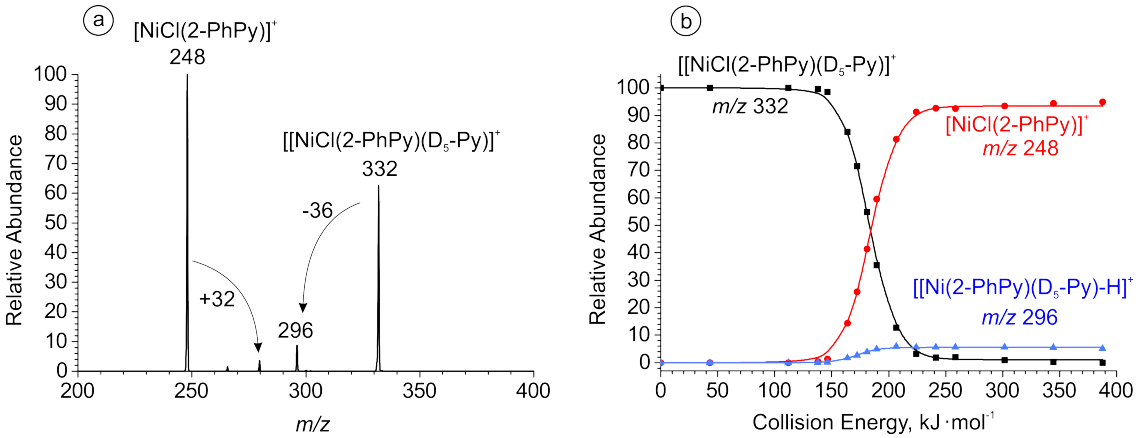

Figure 4.27: a) CID spectrum of the mass-selected $[NiCl(2\text{-}PhPy)(D_5\text{-}Py)]^+$ (m/z = 332) leading to two fragmentation channels: the loss of HCl (product ion with m/z = 296) and D_5-Py (product ion with m/z = 248); b) its breakdown curve.

contrast to Py ligand (which is coordinated only with a N-atom), elimination of PhPy occurs only in small amounts. C-H bond activation, on the other hand, is largely suppressed for the mixed pyridinium complexes, which suggests that the barrier associated with the formation of HCl is close to the binding energy of D_5-Py. Furthermore, for the mixed complexes, significant amounts of DCl elimination are observed. While in the case of 2-PhPy we selectively observe HCl elimination, the corresponding loss for 3- and 4-PhPy complexes is consistent with larger thresholds for these channels. The modeled breakdown curves for all of the investigated complexes can be found in Appendix A, Section 6.2.

4.3.2 Ion mobility studies

In the next step, we studied the above mentioned ions by ion mobility mass spectrometry. Initially, we were interested whether the mobilities of isomeric Ni-complexes would be different. An example of a typical mobilogram obtained for the ion at m/z 403 from the 1:1 mixture of 2- and 3-PhPy is shown in Figure 4.28a. At low cone voltage (U_C = 20 V) all three features (*e.g.* $[NiCl(2\text{-}PhPy)_2]^+$, $[NiCl(2\text{-}PhPy)(3\text{-}PhPy)]^+$, and $[NiCl(3\text{-}PhPy)_2]^+$) are detectable and observed in an approximately 1:2:1 ratio. This is expected from the 1:1 concentration ratio of the isomers. When the cone voltage is increased, $[NiCl(2\text{-}PhPy)_2]^+$ starts to disappear first, followed by the depletion of the mixed $[NiCl(2\text{-}PhPy)(3\text{-}PhPy)]^+$ ion. This observation is in agreement with the predicted steric effects in the complexes: in the case of 2-PhPy the energy of the ligand binding is lower than for the 3-PhPy (Table 4.5), therefore at higher cone voltages it eliminates easier.

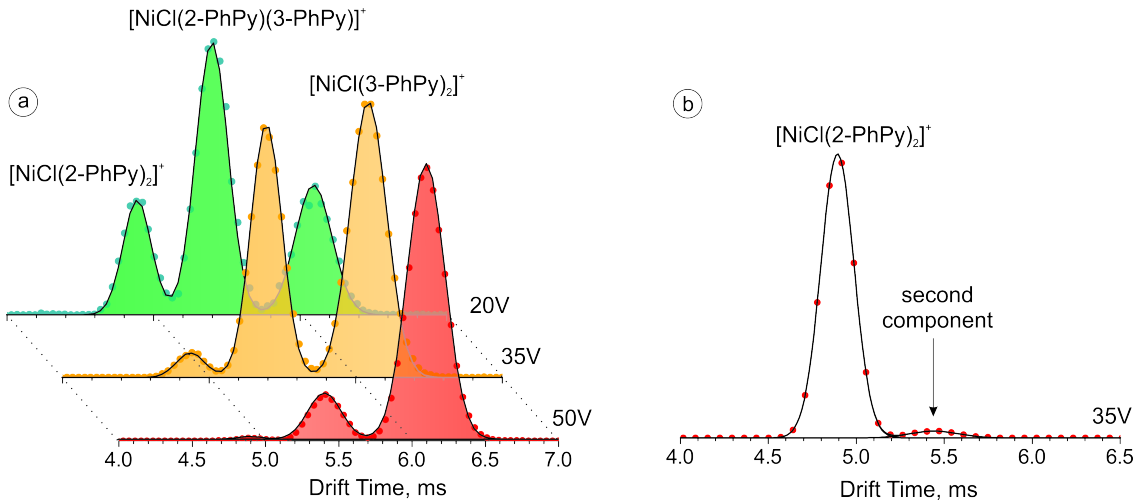

Figure 4.28: a) Arrival time distributions of the mass-selected complex $[NiCl(PhPy)_2]^+$ (m/z = 403) generated upon ESI of a methanolic solution of $NiCl_2$ in the presence of a 1:1 mixture of 2- and 3-PhPy at cone voltages of U_C = 20, 35, and 50 V; b) arrival time distribution of the mass-selected complex $[NiCl(2\text{-}PhPy)_2]^+$ (m/z = 403) generated with a cone voltage of U_C = 35 V. The second component appears at about 5.45 ms. The dots represent the experimental data, black lines - modeled Gaussian curves.

We have compared the arrival times of various complexes generated by ESI-MS and summarized the obtained data in Table 4.6. It should be noted that the meaning of the absolute arrival times that can be determined in a SYNAPT is limited, because they strongly depend on the settings (gas pressure, voltage, *etc.*) of the mobility unit. Therefore, they only can be compared for the species measured under identical conditions.

Table 4.6: Arrival times (in ms) of the ions generated upon ESI of various $NiCl_2$ - PhPy solutions.

	m/z	2-PhPy	3-PhPy	4-PhPy
$[NiCl(PhPy)]^+$	248	2.98	3.80	3.80
$[NiCl(PhPy)_2\text{-}H]^+$	367	4.83	5.32	5.97
$[NiCl(PhPy)_2]^+$	403	4.94	6.08	6.35
$[NiCl(PhPy)_3]^+$	558	*a*	8.90	9.77
$[Ni(PhPy)_3]^{2+}$	261.5	*a*	3.09	3.20
$[Ni(PhPy)_4]^{2+}$	339	*a*	3.74	4.07

[a]The species did not survive mobility sampling.

Naturally, the data in Table 4.6 show that the more compact ions have lower arrival times. Namely, the observed arrival times are drastically smaller for dications, increase with the number of ligands and are also smaller for ions containing 2-PhPy. Thus the arrival times of the isomeric complexes confirm the differences in ligand coordination to

the cationic metal center, and can be a measure of the structural properties of gaseous ions.

When we looked closely at the arrival time distributions of the isolated ions, we faced a challenge in the interpretation of the second feature on the mobilogram for the $[NiCl(PhPy)_2]^+$ cation (Figure 4.28b). In addition to the major component with an arrival time t_a = 4.94 ms, we have observed a second component arriving at approximately 5.45 ms. A careful check of the exact masses for both species revealed that both of them correspond to the same structure of $[NiCl(PhPy)_2]^+$. We have therefore decided to study more closely the properties of the second component on mobilogram at Figure 4.28b. Figure 4.29 shows the dependence of the second component's intensity, as it appears on mobilogram, on the cone voltage. It can be seen that increasing cone voltage leads to an increase in the abundance of the second component at the mobilogram of the $[NiCl(PhPy)_2]^+$ cation.

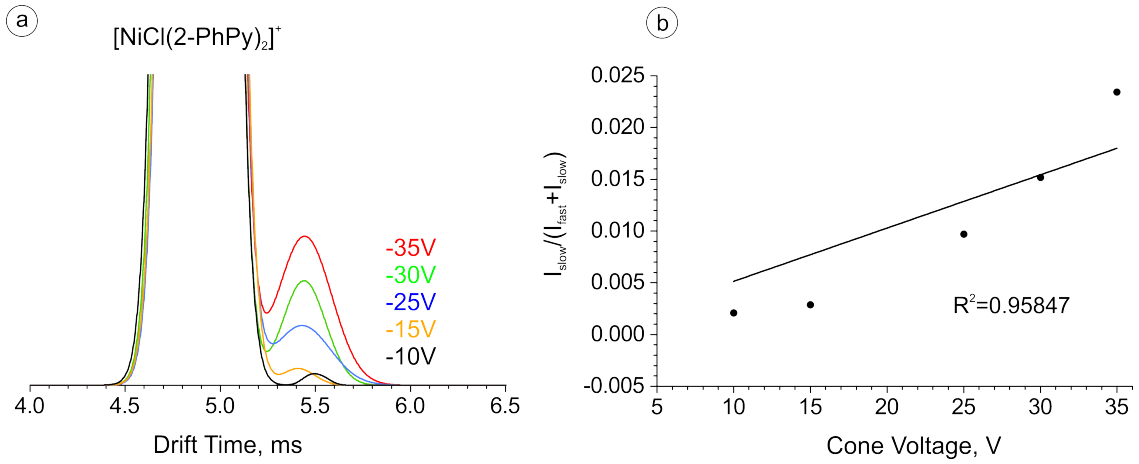

Figure 4.29: a) Arrival time distributions of the mass-selected complex $[NiCl(2\text{-}PhPy)_2]^+$ (m/z = 403) generated with cone voltages of U_C = 35 V, 30 V, 24 V, 15 V and 10 V, respectively. b) Dependence of the relative intensity of the slower component on the cone voltage.

Next, we have performed a series of quantum chemical calculations, in order to unravel the nature of the second feature.

4.3.3 Quantum chemical calculations

Density functional theory (DFT) was used for the theoretical calculations that were performed by Dr. Tibor András Rokob. A more detailed description of the methods and calculations can be found in the original paper[180]. Therefore, in this section only the most important results are summarized.

For $[NiCl(PhPy)_2]^+$ cation both the singlet and triplet state structures were calculated and optimized. Several isomeric structures of $[NiCl(PhPy)_2]^+$ were located, however their relative energy differences were rather small. It was shown that the interconversion within located structures proceeded with minor barriers and should be facile. The calculations also showed that the triplet state was slightly more stable than the singlet. Comparison of the geometries for these two states showed that they largely did not differ. Moreover the spin-state changes are faster with respect to the millisecond scale of the IM-MS module[181]. Taking into account the small barriers to interconversion and changes in spin-states, theoretical analysis did not provide a logical explanation for the existence of the second feature in the ion mobility trace of $[NiCl(2\text{-}PhPy)_2]^+$.

The possible structures of the ion $[NiCl(PhPy)]^+$ that could be formed after the loss of phenylpyridine ligand were also analyzed. The energies for the lowest-lying structures and the respective dissociation channels are summarized in Table 4.7. The data show that, as was found in the experiment, the energy required for ligand loss is significantly smaller in the case of 2-PhPy. When we take into account the error values for the experiment as well as for the DFT method, good agreement can be found between experimentally obtained appearance energies for the phenylpyridine loss and the corresponding calculated values (*e.g.* 198 kJ·mol^{-1} *vs.* 170 kJ·mol^{-1} for 2-PhPy, 222 kJ·mol^{-1} *vs.* 215 kJ·mol^{-1} for 3-PhPy, and 220 kJ·mol^{-1} *vs.* 230 kJ·mol^{-1} for 4-PhPy derivatives).

Table 4.7: 0 K relative energies (in kJ·mol^{-1}) of the various complexes (M06/def2-TZVPP// B3LYP-D3/def2-SVP).

	$[NiCl(PhPy)_2]^+$		$[NiCl(PhPy)]^+$ + PhPy		$[Ni(PhPy)_2\text{-}H]^+$ + HCl	
	singlet	triplet	singlet	triplet	singlet	triplet
2-PhPy	5.1	0	227.5	197.9	109.4 (128.7)[a]	163.3
3-PhPy	84.6	60.1	326.3	281.9	*b*	*b*
4-PhPy	70.8	46.1	310.5	265.2	*b*	*b*

[a]The energy necessary to initiate a reaction leading to this species exceeds the relative energy of the most stable product; this energy requirement is shown in parentheses. [b]Not calculated.

With respect to the experimental findings, the complete reaction pathway for the loss of HCl from $[NiCl(2\text{-}PhPy)_2]^+$ ion was also calculated. The theoretical results agree with experiment in finding that the elimination of HCl requires less energy than phenylpyridine loss (Table 4.7). For the triplet case 163.3 kJ·mol^{-1} is necessary for C-H activation which lies in a very good agreement with the experimentally obtained value of 160 kJ·mol^{-1}. The

reaction however may also proceed along the more favorable singlet pathway with an overall energy demand of only 128.7 kJ·mol^{-1}. In that case the experimental appearance energy might be overestimated due to the higher kinetic shift associated with the rearrangements happening along the singlet pathway, and the agreement between theory and experiment might be considered as reasonable.

In conclusion, theoretical investigations excluded several possibilities that might explain the existence of the second feature in the ion mobility trace of $[NiCl(2\text{-}PhPy)_2]^+$. The theory confirmed the existence of several possible structures with different cross sections, however all of them were predicted to interconvert under the conditions of IM-MS experiments.

As the computational data did not succeed in finding a suitable explanation for the observation of the second feature in the $[NiCl(2\text{-}PhPy)_2]^+$ mobilogram, we returned from theory back to experiment. Comparison of the arrival times of the various $[NiCl(PhPy)_2]^+$ ions with the computed cross sections (Figure 4.30) revealed a good linear correlation.

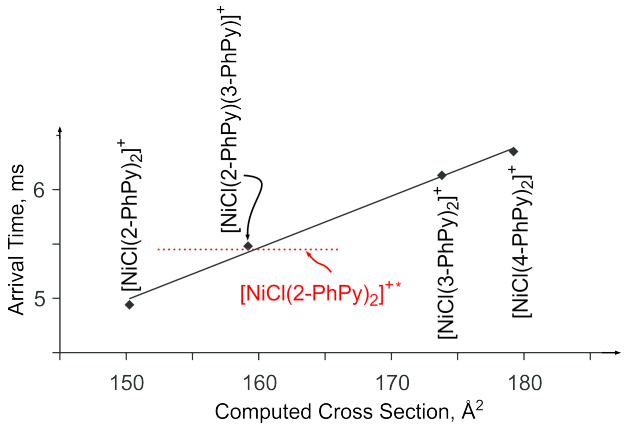

Figure 4.30: Measured arrival times in IM-MS versus computed cross sections of selected $[NiCl(PhPy)_2]^+$ complexes. The red horizontal line denotes the arrival time of the second feature from the $[NiCl(2\text{-}PhPy)_2]^+$ sample.

Moreover, the arrival time of the second feature of $[NiCl(2\text{-}PhPy)_2]^+$ agrees well with the computed cross section of the mixed complex $[NiCl(2\text{-}PhPy)(3\text{-}PhPy)]^+$. Therefore we have checked the commercial sample of 2-PhPy for possible impurities. Selected ion monitoring GC/MS has indeed confirmed a contamination of the commercial sample of 2-PhPy with about 0.2% of 3-PhPy. The presence of this impurity explains the appearance of the second component in Figure 4.28b.

4.4 Carboxylate assisted C-H activation of phenylpyridines with copper, palladium and ruthenium

It was shown that C-H activation reactions can proceed more efficiently *via* so-called ligand direction, especially with ligands acting as bases[168]. Recent mechanistic investigations have shown that ligand assisted C-H bond activation can proceed *via* a simultaneous metalation and intramolecular deprotonation: the so-called concerted metalation-deprotonation (CMD) mechanism[182–184].

In this study we have chosen to investigate the role of carboxylate, as a directing ligand for C-H activation, and compare the behavior of three metal catalysts: ruthenium, palladium and copper in the gas phase. It was shown that these types of reaction proceed smoothly with unsaturated heterocycles. For example, copper acetate is capable of activating a C-H bond in the C-2 position of 2-phenylpyridine, enabling subsequent nucleophilic substitution[171,185]. Therefore, for our mechanistic study, we have chosen 2-phenylpyridine as the main substrate for C-H activation (Scheme 4.9).

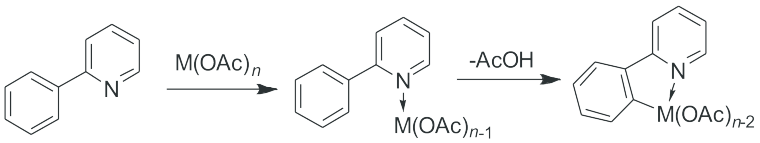

Scheme 4.9: The carboxylate assisted C-H activation investigated here; M corresponds to Ru, Cu and Pd.

4.4.1 ESI-MS studies

C-H activation catalyzed by ruthenium carboxylate

For ruthenium catalysis, we have generated the catalytic LRuOAc species *in situ* using the commercially available complex $[(C_6H_6)RuCl_2]_2$. This was possible upon addition of carboxylic acid and a base to a solution of ruthenium chloride dimer[168]. To this end, we have added 1 equivalent of the acetic acid and triethylamine to a 0.1 mM solution of the corresponding ruthenium dimer in acetonitrile. The use of triethylamine was motivated by the fact that it is soluble in acetonitrile and therefore suitable for ESI-MS experiments. The spectrum of the resulting mixture is shown in Figure 4.31a (mixture A). It indeed shows the formation of the desired catalytic ruthenium carboxylate species at m/z 400. After that, we added 1 equivalent of 2-PhPy to mixture A (mixture B) and observed the ion at m/z 394 that could correspond to the formation of the $[(C_6H_6)Ru((2\text{-}PhPy)OAc)]^+$ complex. When

subjected to CID, the ion at m/z 394 loses acetic acid, forming the ion at m/z 334 with the probable formula $[(C_6H_6)Ru((2\text{-}PhPy)\text{-}H)]^+$. Hence, fragmentation of the ion at m/z 394 could either correspond to C-H activation of the ion $[(C_6H_6)Ru((2\text{-}PhPy)OAc)]^+$, or to elimination of the loosely bound AcOH ligand from the already activated phenylpyridinium complex ($[(C_6H_6)Ru(2\text{-}PhPy\text{-}H)HOAc]^+$). The appearance energy for the acetic acid loss was determined as 113 ± 3 kJ·mol^{-1}(see Figure 4.32). We note in passing that analogues ruthenium carboxylate complexes were synthesized and isolated from reaction mixtures similar to those used in our experiments[169,186,187].

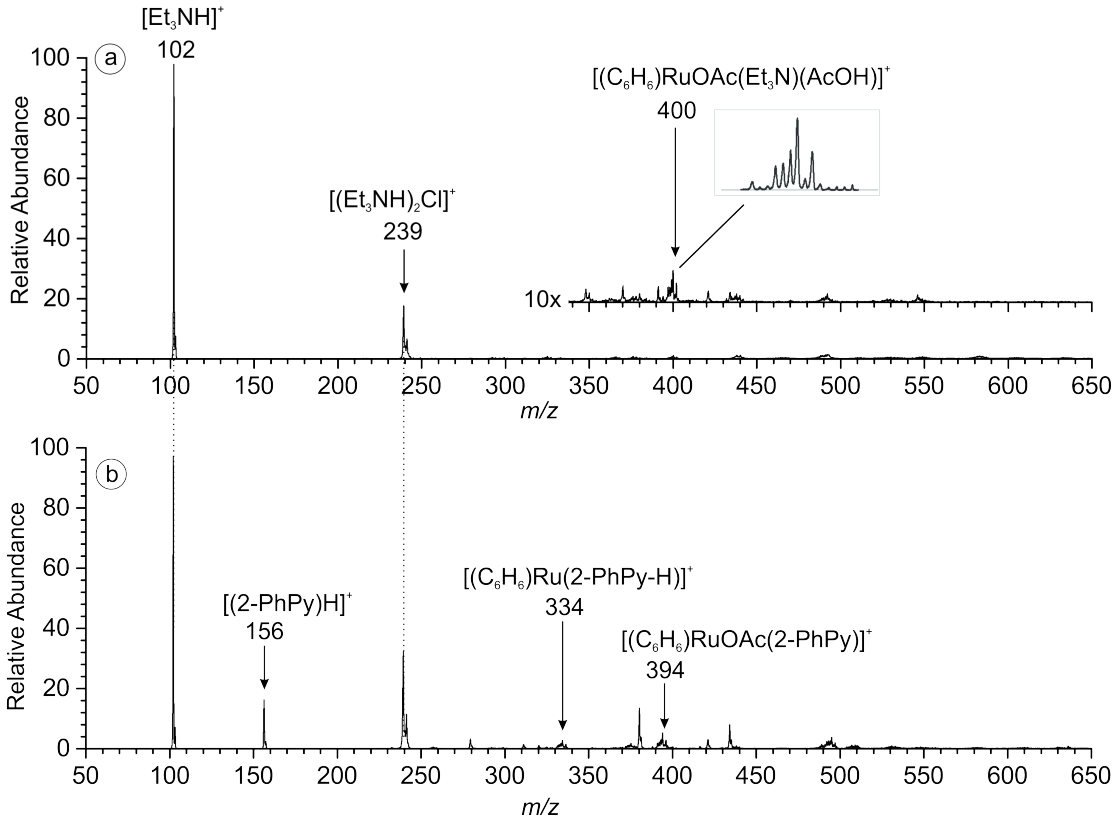

Figure 4.31: a) ESI-MS spectrum of Ru-dimer complex, acetic acid and triethylamine in acetonitrile (mixture A); b) ESI-MS spectrum of Ru-dimer complex, acetic acid, triethylamine and 2-phenylpyridine (mixture B) in acetonitrile.

If mixture B is allowed to stand for longer time, new peaks appear on the ESI mass spectrum. For example, Figure 4.33 shows the spectrum taken 5 hours after the preparation of reaction mixture B.

The peak appearing at m/z 469 is noteworthy. Closer analysis of its isotopic pattern reveals that this ion has one ruthenium atom and therefore might either represent a complex with two activated phenylpyridines and a formal Ru(IV) center or a complex with a Ru(II)

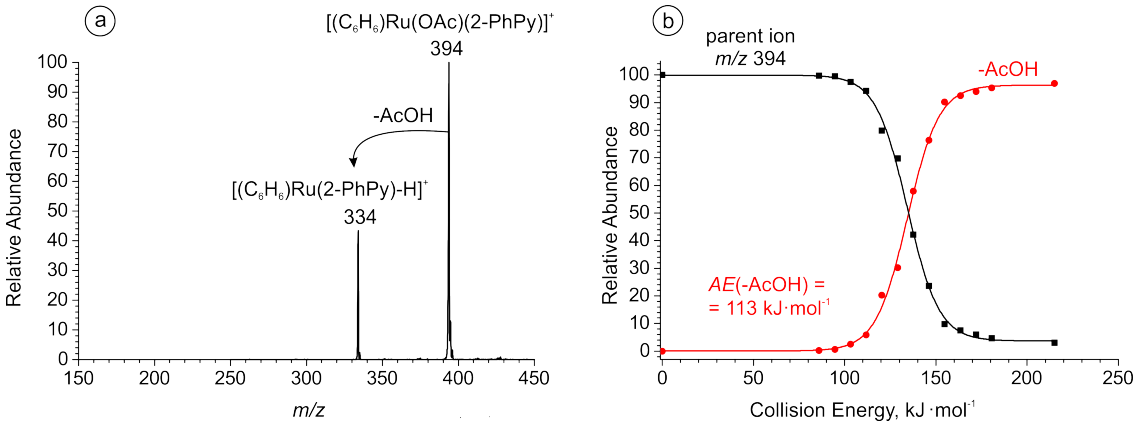

Figure 4.32: a) CID spectrum of the mass selected peak at m/z 394 (2-PhPy); b) the breakdown curve for m/z 394 (2-PhPy). The appearance energy for acetic acid loss was determined to be AE(-AcOH) = 113 ± 3 kJ·mol^{-1}.

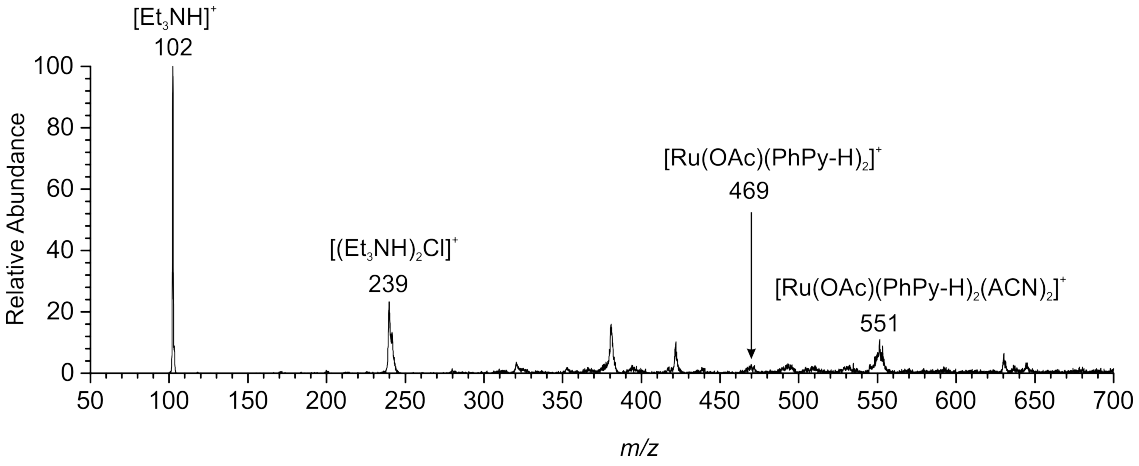

Figure 4.33: ESI-MS spectrum of the Ru-dimer complex, acetic acid, triethylamine and 2-phenylpyridine in acetonitrile taken 5 hours after mixing the components showing the appearance of m/z 469.

center (see Scheme 4.10).

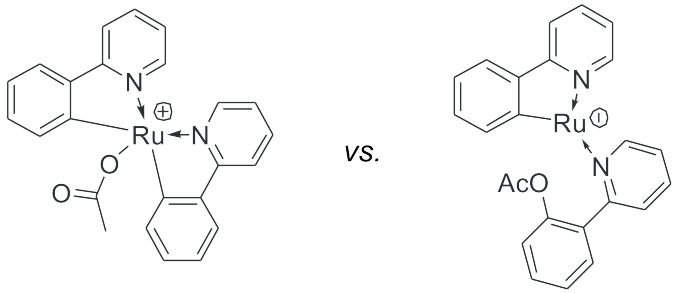

Scheme 4.10: Possible structures for the complex at m/z 469.

In order to study the ion at m/z 469 in greater detail we performed CID analysis. Figure 4.34 shows the CID spectrum and a breakdown curve for the complex at m/z

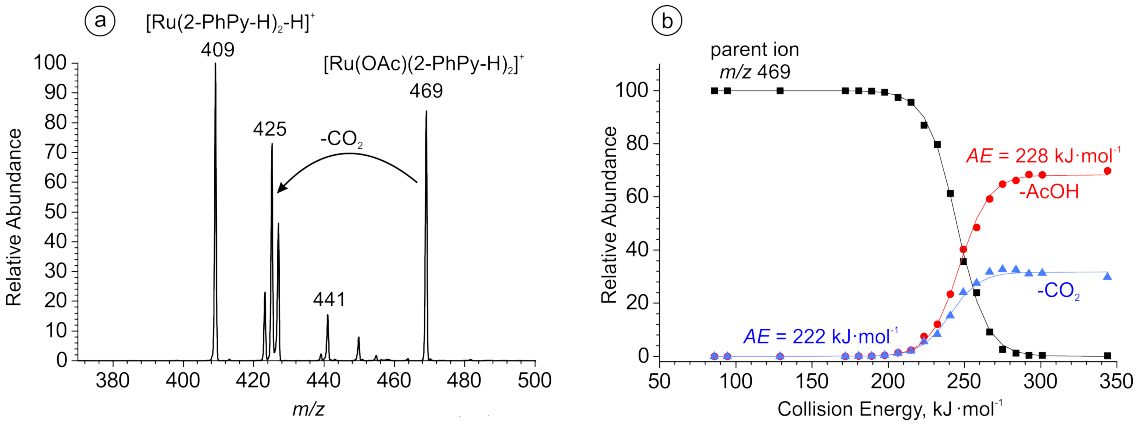

Figure 4.34: CID spectrum of the mass selected peak at m/z 469; b) the breakdown curve for m/z 469. The appearance energies for acetic acid and CO_2 losses were determined to be AE(-AcOH) = 228 ± 3 kJ·mol^{-1} and AE(-CO_2) = 222 ± 3 kJ·mol^{-1}, respectively.

469. The main fragmentation pathway being the loss of acetic acid occurs at a fairly high appearance energy (228 ± 3 kJ·mol^{-1}), which would be anticipated for secondary activation of 2-PhPy. The observation that the main fragmentation channel is acetic acid loss, and not elimination of 2-(pyridin-2-yl)phenyl acetate may demonstrate that the observed ion at m/z 469 corresponds to a species with a Ru(IV) center. On the other hand, the loss of an acetoxy radical would be expected for a Ru(IV) species, and this fragmentation channel was not experimentally observed. The second fragmentation pathway is decarboxylation, occurring with a slightly lower appearance energy (222 ± 3 kJ·mol^{-1}). This CO_2 loss appears to be unlikely for a Ru(IV) species and would rather appear for an ion with Ru(II) center bearing 2-(pyridin-2-yl)phenyl acetate. The presence of other minor peaks in the CID spectrum in Figure 4.34a is caused by the addition of solvent molecules (H_2O and acetonitrile) to the daughter ions in the ion trap. Unfortunately, our initial IRMPD studies for m/z 469 were inconclusive, and the obtained spectra did not help to reveal the structure of this ion. Nevertheless potential formation of the Ru(IV) species is very interesting, and more studies (IRMPD, DFT, *etc.*) are being carried out in order to investigate the ion at m/z 469 in greater detail.

In order to better understand the behavior of the reaction mixture for ruthenium catalysis and its speciation under ESI-MS conditions, we have studied the dependence of 2-phenylpyridine concentration on the formation of ions in the gas phase. Figure 4.35 shows an example of the spectrum obtained for such investigation. The experiment showed that increasing the concentration of 2-phenylpyridine increases the abundance of both non-activated and activated (m/z 394 and m/z 334) ruthenium complexes (Figure 4.36).

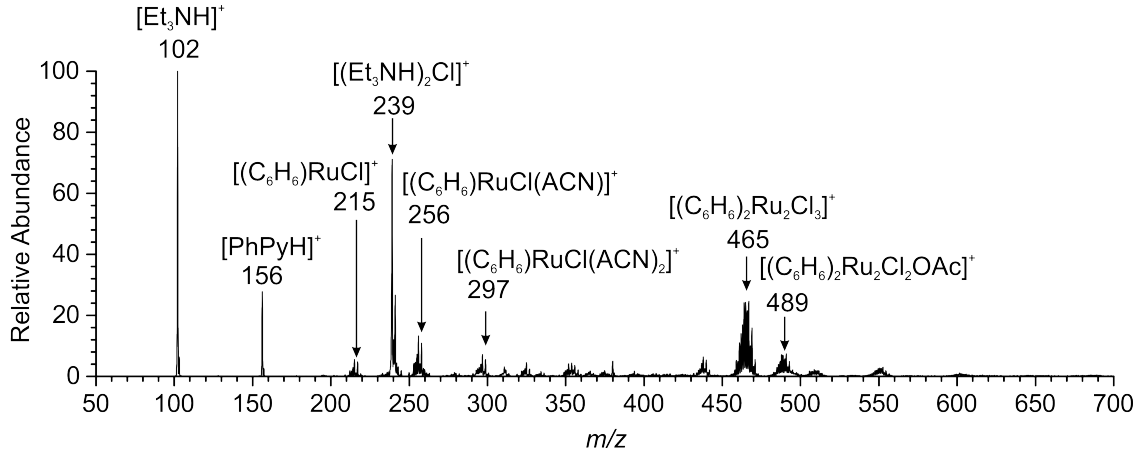

Figure 4.35: ESI-MS spectrum of Ru-dimer complex, acetic acid and triethylamine in acetonitrile (1:1:1 eq, 10^{-3} M) after addition of 0.25 eq. of 2-PhPy. Note that the m/z ratios for ions are shown for the ^{102}Ru isotope.

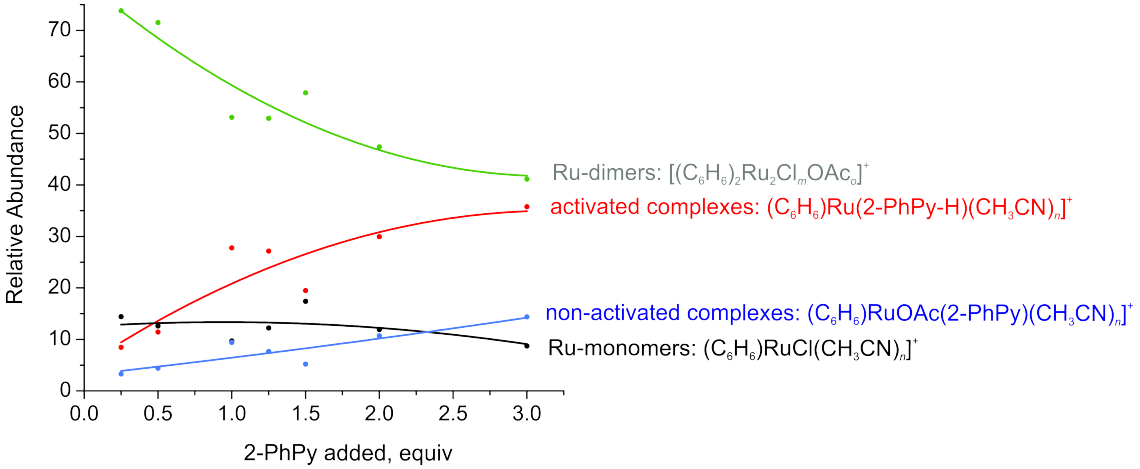

Figure 4.36: Dependence of the relative abundance of various Ru-clusters on the amount of 2-PhPy in the solution (where n, m and o are vibrate integers that specify the number of ligands).

We have also compared the ability of *L*RuOAc catalyst to activate 3-PhPy. To this end, we prepared solutions with 3-PhPy identically to those with 2-PhPy and subjected them to ESI-MS and CID analysis. Resulting spectrum is shown in Figure 4.37. CID of the ion at m/z 394 showed that although the C-H activation of 3-PhPy is still possible, the major fragmentation pathway is the loss of the neutral 3-PhPy ligand (Figure 4.38a, blue). The energy required for elimination of acetic acid was determined as 170 ± 3 kJ·mol^{-1}.

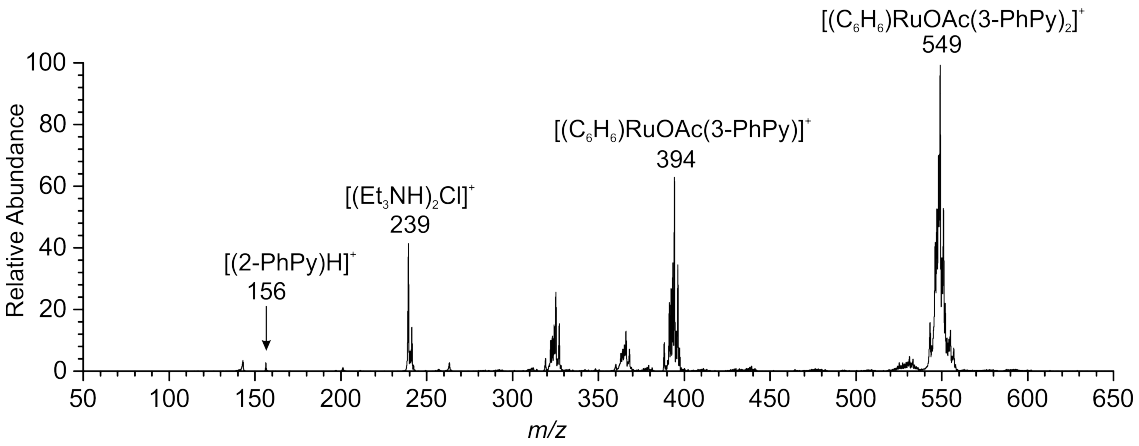

Figure 4.37: ESI-MS spectrum of Ru-dimer complex, acetic acid, triethylamine and 3-phenylpyridine in acetonitrile.

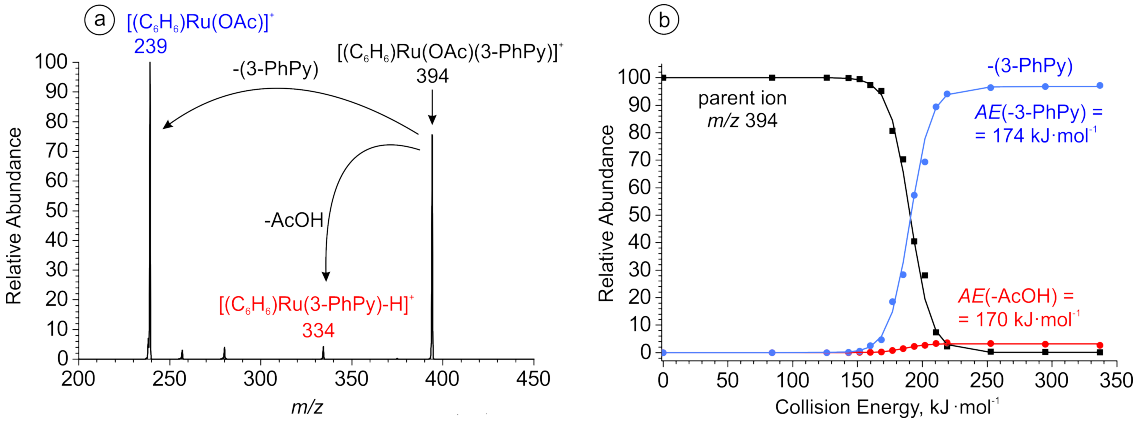

Figure 4.38: a) CID spectrum of the mass selected peak at m/z 394 for 3-PhPy; b) the breakdown curve for m/z 394 (3-PhPy). The appearance energy for acetic acid and 3-PhPy loss was determined to be AE(-AcOH) = 170 ± 3 kJ·mol^{-1}and AE(-3-PhPy) = 174 ± 3 kJ·mol^{-1}, respectively.

C-H activation catalyzed by copper acetate

ESI-MS of a copper acetate/2-PhPy solution (1:1) in acetonitrile is shown in Figure 4.39. We observed the formation of complex at m/z 432 that can be formally described as a $CuOAc^+$ core bearing two 2-PhPy moieties. CID of this complex showed the appearance of two elimination channels: acetic acid and 2-PhPy losses (Figure 4.40a). We determined the appearance energies for the losses as: 138 ± 5 kJ·mol^{-1} for acetic acid and 147 ± 5 kJ·mol^{-1} for 2-phenylpyridine. As is shown in Figure 4.40, the loss of 2-PhPy is more abundant although it has a higher appearance energy. Hence, elimination 2-PhPy is favored kinetically, whereas elimination of AcOH most likely corresponds to C-H activation *via* a tight transition state. Therefore, the structure of the ion at m/z 432 corresponds to the non-activated

$[Cu(OAc)(2\text{-}PhPy)_2]^+$ rather than activated $[Cu(2\text{-}PhPy)(2\text{-}PhPy\text{-}H)(AcOH)]^+$.

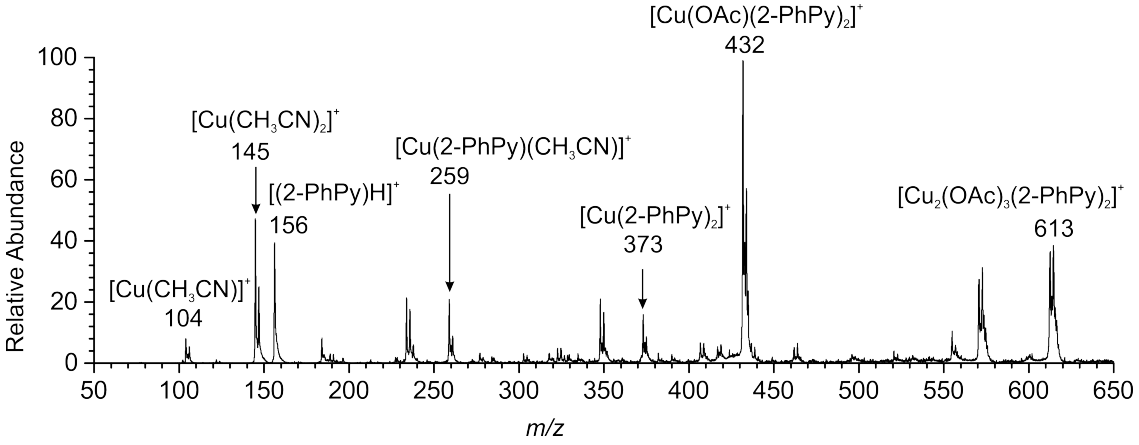

Figure 4.39: ESI-MS spectrum of the mixture of $Cu(OAc)_2$ and 2-PhPy in acetonitrile. Note that the m/z ratios for ions are shown for the ^{63}Cu isotope.

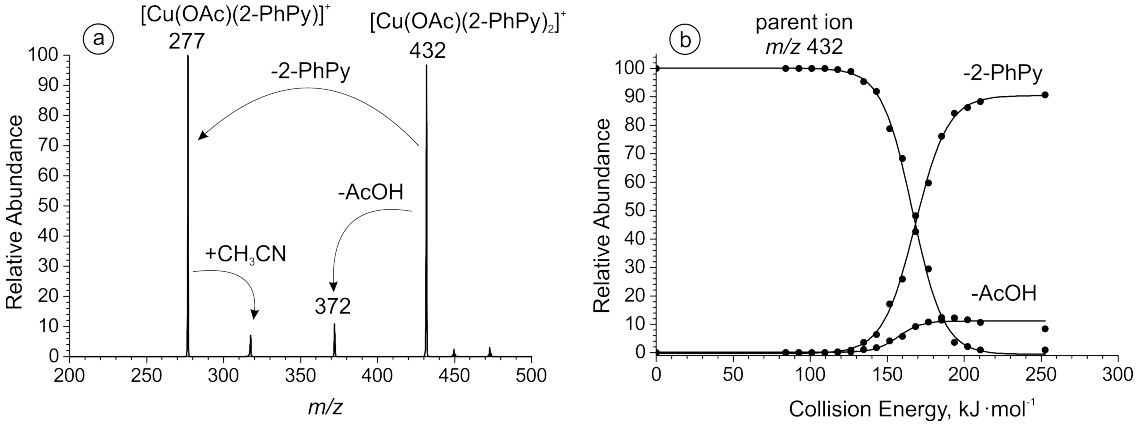

Figure 4.40: The CID spectrum and the breakdown curve for the mass selected peak at m/z 432. AE for the AcOH loss: 138 ± 5 kJ·mol^{-1}, AE for the 2-PhPy loss: 147 ± 5 kJ·mol^{-1}.

C-H activation catalyzed by palladium acetate

ESI-MS of a palladium acetate-2-PhPy solution (1:1) in acetonitrile is shown in Figure 4.41. The spectrum shows the appearance of ions with a Pd-C bond (*e.g.* m/z 415 and m/z 570) and possibly non-activated complexes containing an acetoxy ligand (m/z 475 and 630). The latter are present in small abundances which means that most of the 2-PhPy is already activated. Similar to the copper catalysis, the ion at m/z 475 may correspond to the non-activated Pd-complex: ($[Pd(OAc)(2\text{-}PhPy)_2]^+$).

CID activation of the complex at m/z 475 leads to the exclusive elimination of acetic acid (Figure 4.42), and the appearance energy for this loss is 65 ± 3 kJ·mol^{-1}. The AE

for acetic acid loss is much lower than for the previously investigated complexes, therefore the ion at m/z 475 may correspond to already activated complex [Pd(2-PhPy)(2-PhPy-H)(AcOH)]$^+$.

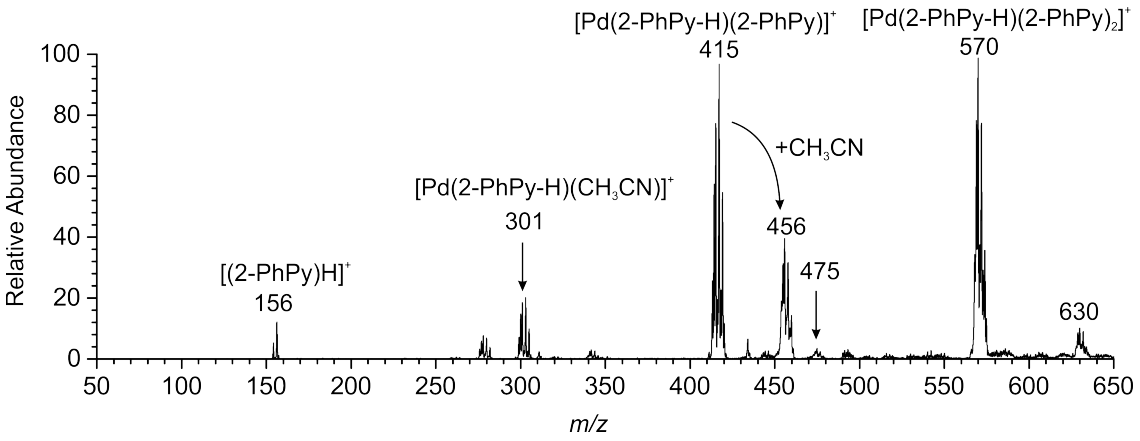

Figure 4.41: ESI-MS spectrum of $Pd(OAc)_2$ and 2-PhPy in acetonitrile. Note that the m/z ratios for ions are shown for the ^{106}Pd isotope.

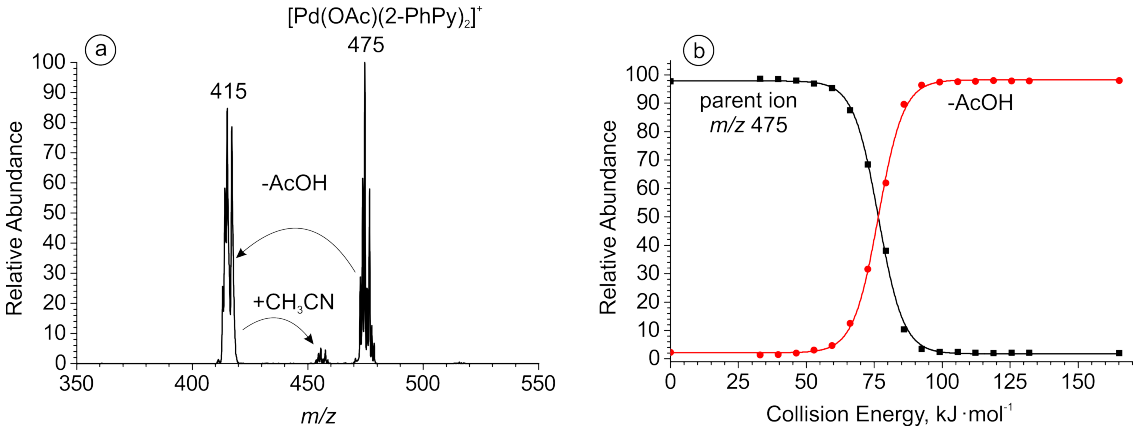

Figure 4.42: The CID spectrum of the mass selected peak at m/z 475 and its breakdown curve. AE for AcOH loss: 65 ± 3 kJ·mol^{-1}.

On the other hand, CID analysis of the complexes containing more 2-phenylpyridine ligands (*e.g.* the complex at m/z 630, which could correspond to [Pd(OAc)(2-PhPy)$_3$]$^+$) showed the elimination of neutral 2-phenylpyridine and subsequent C-H activation (see Figure 4.43). Observation of a "step" at around 180 kJ·mol^{-1} on the breakdown curve for the complex at m/z 630 could be explained by the fact that a mixture of two isomers is generated and the second isomer starts to fragment at a much higher energy[188]. We have not determined the structure of the second isomer, so more studies are being carried out in this direction.

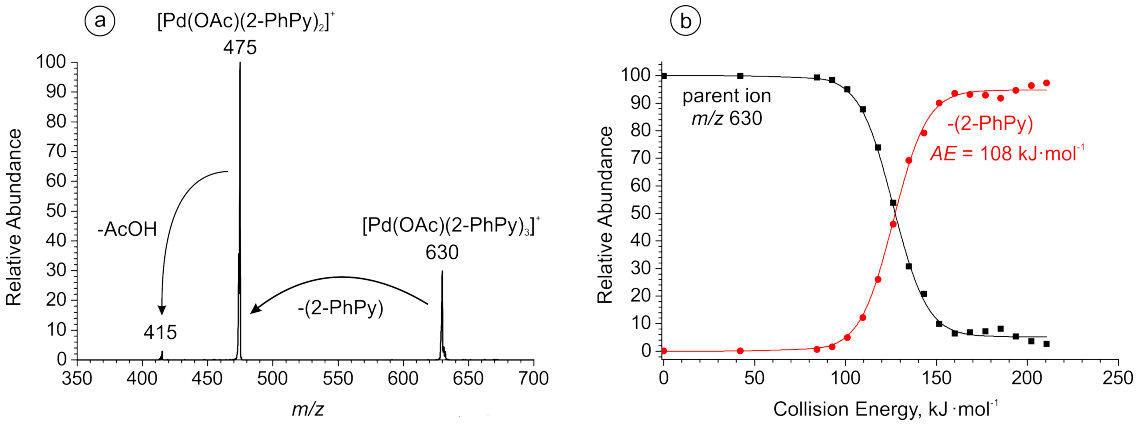

Figure 4.43: CID spectrum for the mass selected peak at m/z 630 and its breakdown curve. Appearance energy for 2-PhPy loss is 108 ± 3 kJ·mol^{-1}.

4.4.2 Theoretical investigations of reaction pathways

The quantum chemical calculations for this project were performed by Dr. Andrew Gray. Therefore, this section will only briefly summarize the most important results. More detailed discussion together with all of the calculated structures and potential energy surfaces can be found in the recently published paper[189].

To this end, three complexes (m/z 394, m/z 432 and m/z 475) investigated with ESI-MS were subjected to DFT calculations to study the mechanism of acetate assisted C-H activation. The mechanisms have common steps and therefore similar labeling is used to enable their comparison. The progression of the investigated reactions is described in Scheme 4.11.

The individual potential energy surfaces shown below are labeled in accordance with Scheme 4.11. For Ru catalysis L represents the π-bonded benzene ligand, while in the Cu or Pd complexes L stands for 2-PhPy. Labeling is consistent for all metal complexes; the metal is indicated in the text using superscript prefixes.

The calculated reaction pathway for $[(C_6H_6)Ru(OAc)(2\text{-PhPy})]^+$ is shown in Figure 4.44a. The lowest energy intermediate $^{Ru}1_a$ (with acetate bound to Ru as a bidentate ligand) interconverts to $^{Ru}2_a$ (where Ru is bearing acetate monodentally) with an energy barrier of 60 kJ·mol^{-1}. The hydrogen transfer from this complex requires only 4 kJ·mol^{-1} forming the transition state $^{Ru}TS_{2a\text{-}3a}$. The transition state leads to the activated intermediate $^{Ru}3_a$ with acetic acid bound to Ru, which is 14 kJ·mol^{-1} less stable than the non-activated initial structure. In intermediate $^{Ru}3_a$ a weak interaction between the OH group and 2-PhPy is present that can be removed with an energy cost of 16 kJ·mol^{-1}. From

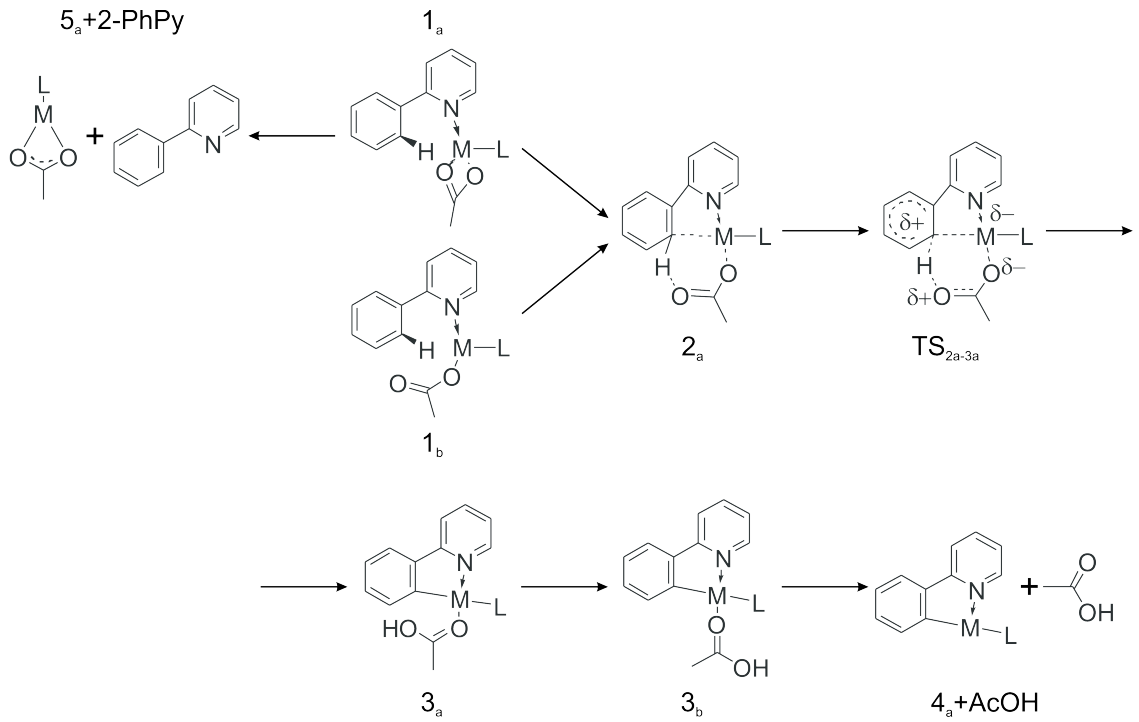

Scheme 4.11: Structural representations of the different calculated species involved in the C-H activation reactions; *M* corresponds to Ru, Cu and Pd.

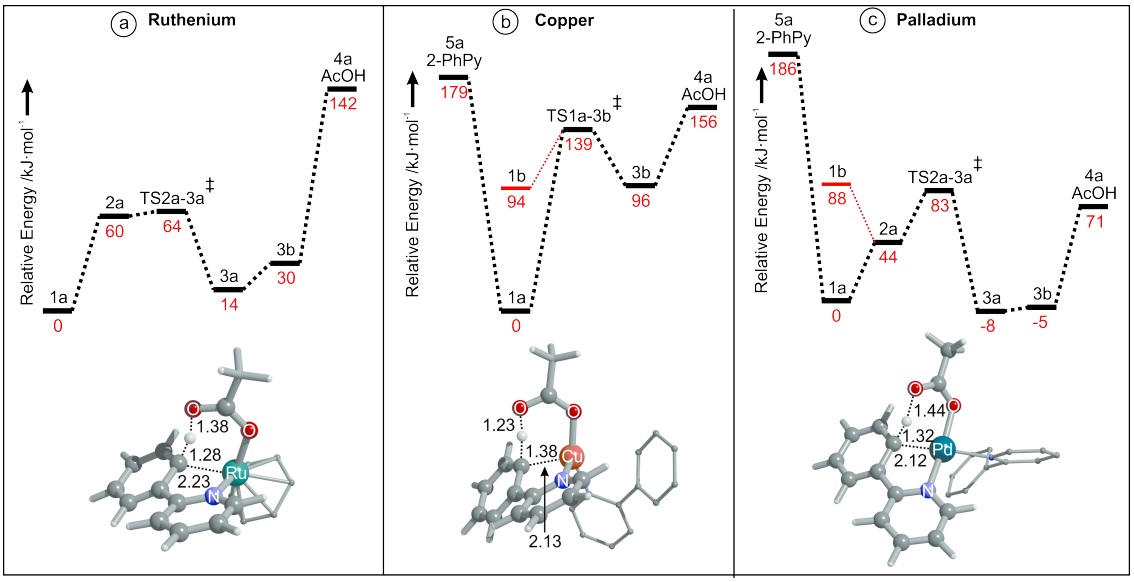

Figure 4.44: Potential energy surfaces for the a) Ru-, b) Cu- and c) Pd-assisted C-H activation of 2-PhPy. All energies are at 0 K and the depicted structures represent the transition structures; distances are in Å. B3LYP/cc-pVTZ:cc-pVTZ-pp(*M*).

this point, dissociation of the acetic acid ligand can take place with an energy cost of 112 kJ·mol^{-1} giving an overall energy increase for this transformation of 142 kJ·mol^{-1}.

The calculated potential energy surface for Cu-catalyzed C-H activation is shown in Figure 4.44b. In the $^{Cu}1_b$ structure the metal bears a monodentate acetate ligand. This

structure lies 94 kJ·mol^{-1} higher in energy and is strongly disfavored. Hydrogen transfer from 2-PhPy to acetate now requires 139 kJ·mol^{-1} and the energy gap between the activated and non-activated complexes (*i.e.* 3_b and 1_a) is 96 kJ·mol^{-1}. Next, the energy requirement for the elimination of AcOH from $^{Cu}3_b$ is 60 kJ·mol^{-1} and the overall energy demand is 156 kJ·mol^{-1}. The large initial activation barrier suggests that we observe and excite the initial $^{Cu}1_a$ isomer in the mass spectrometry experiments. The 2-PhPy dissociation pathway proceeded theoretically at 179 kJ·mol^{-1} which is 23 kJ·mol^{-1} higher than AcOH elimination. Collision-induced dissociation of 2-PhPy should proceed *via* a loose transition state (for more details see Section 2.2.1), and it was not possible to locate a transition state for 2-PhPy dissociation.

The calculated reaction pathway for Pd-catalyzed C-H activation is shown in Figure 4.44c. The monodentate version of the starting conformation is 88 kJ·mol^{-1} less stable than the bidentate isomer. Next, interconversion to a distorted bidentate isomer $^{Pd}2_a$ requires 44 kJ·mol^{-1}. The TS has an activation energy of 83 kJ·mol^{-1}. The difference in the relative energy of structures $^{Pd}3_{a/b}$ is probably the most significant. These structures, still bearing AcOH ligand, actually appeared to be more stable than the non-activated $^{Pd}1_a$ structure. The energy of acetic acid dissociation from $^{Pd}3_b$ was found to be 76 kJ·mol^{-1}. Elimination of 2-PhPy from $^{Pd}1_a$ was shown to take place with an energy considerably higher than for AcOH (186 kJ·mol^{-1}). Therefore this fragmentation channel is not observed experimentally.

4.4.3 Infrared multiphoton dissociation studies

The ions $[(C_6H_6)Ru(OAc)(2\text{-}PhPy)]^+$, $[Cu(OAc)(2\text{-}PhPy)_2]^+$ and $[Pd(OAc)(2\text{-}PhPy)_2]^+$ were further subjected to IRMPD experiments. The band positions on the obtained spectra were then compared with theoretically calculated spectra. It should be noted that due to the multiphotonic character of IRMPD spectra, the intensities of individual bands can be very different in comparison to those obtained for single-photon theoretical spectra[190].

The experimental IRMPD spectrum for the complex $[(C_6H_6)Ru(OAc)(2\text{-}PhPy)]^+$ is shown in Figure 4.45. It compares well with the theoretical spectrum for the non-activated isomer ($^{Ru}1_a$) which was found to have the lowest energy and is therefore the most stable in comparison to the other calculated isomers. In structure $^{Ru}1_a$ acetate is bound as a bidentate ligand to the ruthenium atom, which is coordinated to the nitrogen of 2-PhPy and π-bonded to the aromatic system of benzene. The vibration bands of $^{Ru}1_a$ show a strong match to the experimentally observed spectrum: the bands at 1480 cm^{-1} represent

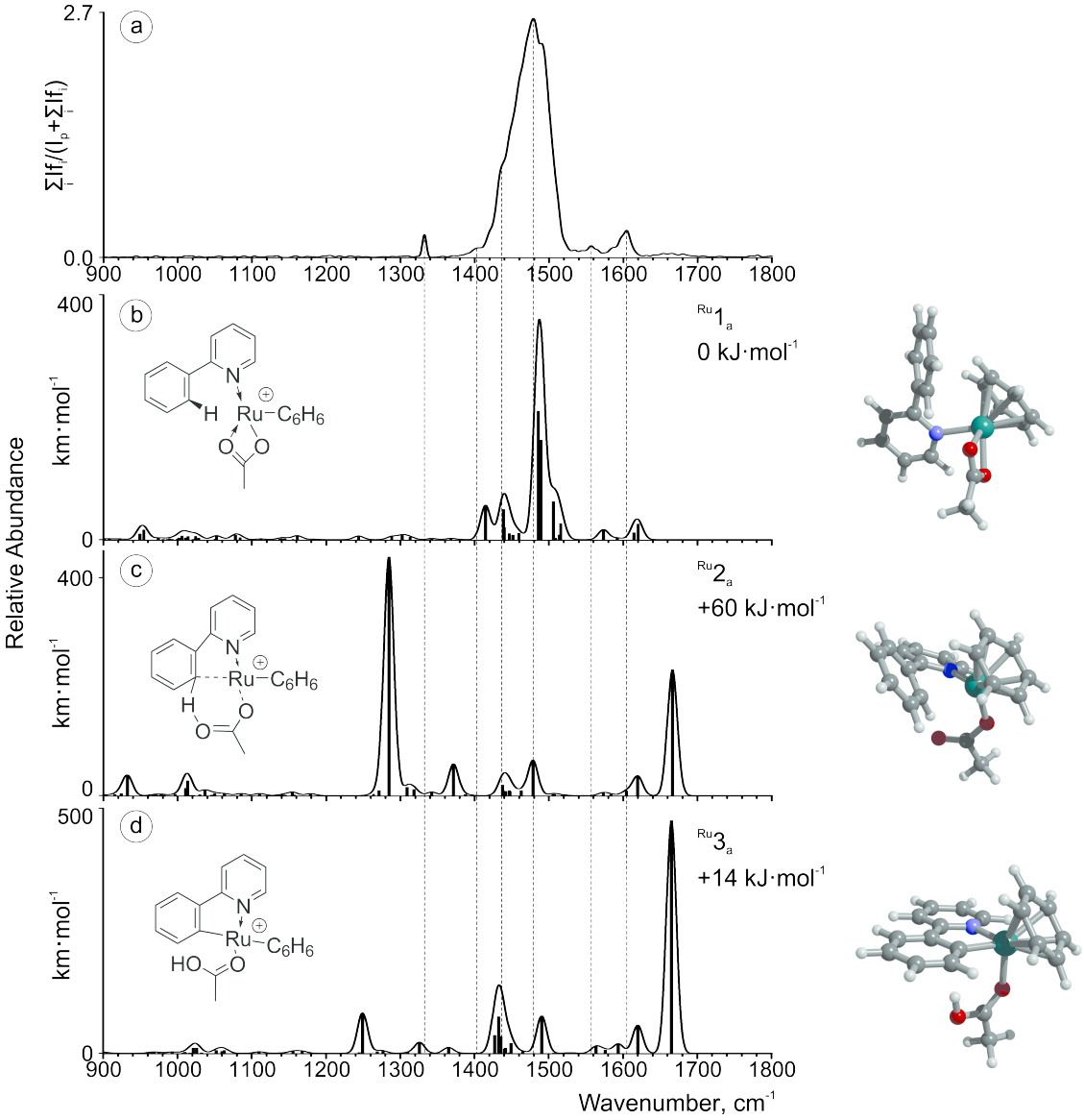

Figure 4.45: a) IRMPD spectrum of the mass-selected $[(C_6H_6)Ru(OAc)(2\text{-PhPy})]^+$ complex and theoretical IR spectra of b) $^{Ru}1_a$, c) $^{Ru}2_a$ and d) $^{Ru}3_a$. The line spectra are presented along with a Gaussian function with fwhm = 16 cm^{-1}.

symmetric and asymmetric C-O acetate stretching modes, and C-C double bond stretches of the 2-PhPy ligand (1557 and 1605 cm^{-1}). The experimental spectrum also shows bands at 1403 and 1435 cm^{-1} that correspond to C-H bends within the acetate ligand.

Figures 4.45c and 4.45d representing complexes $^{Ru}2_a$ and $^{Ru}3_a$, respectively, show poor match with experiment especially for the key experimental C-O and C-C stretches with weak bands present in the key experimental range.

An experimental IRMPD spectrum for $[Cu(OAc)(2\text{-PhPy})_2]^+$ is shown in Figure 4.46a. Again, excellent agreement was found between the theoretical spectrum for the stable

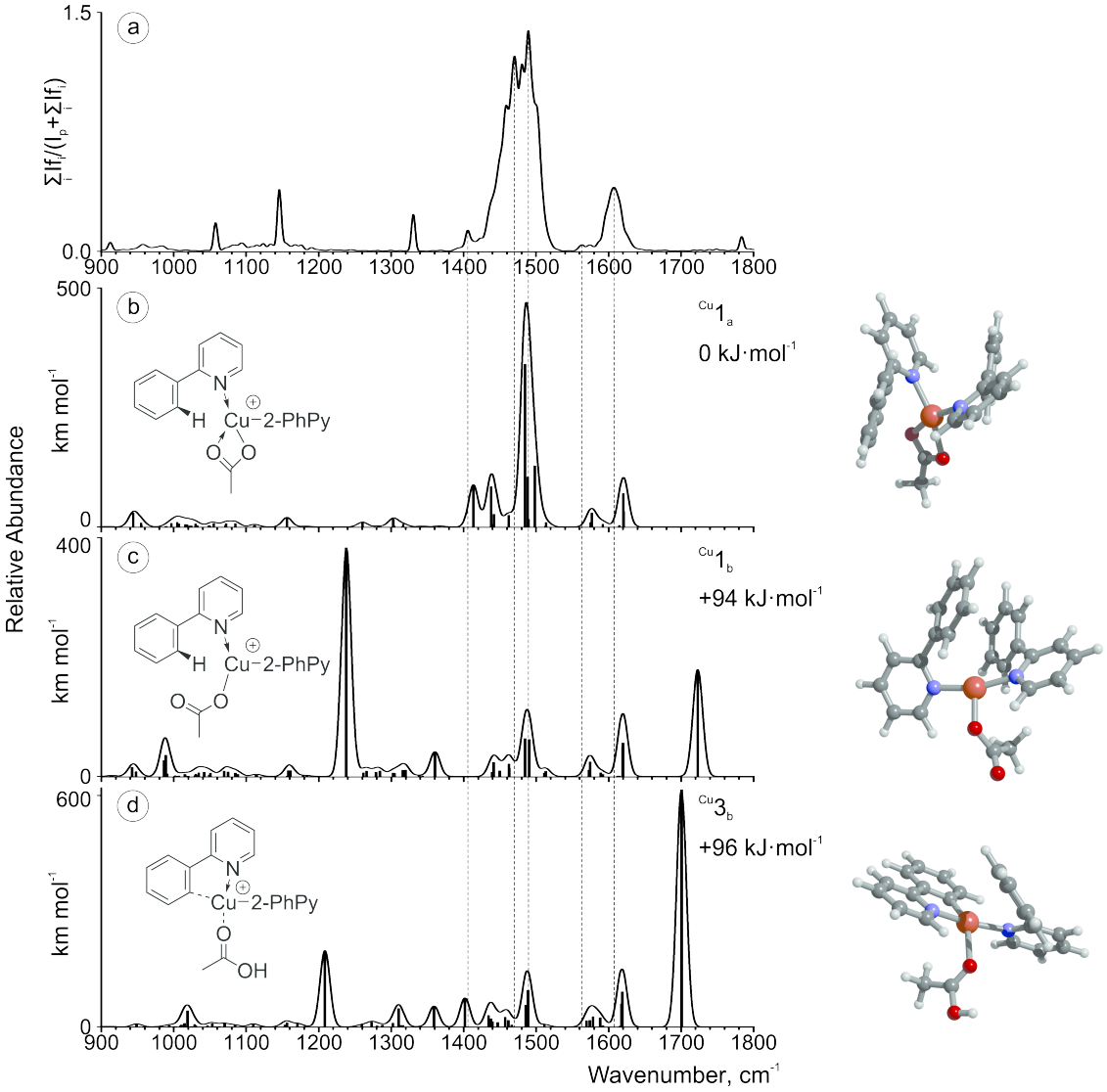

Figure 4.46: a) IRMPD spectrum of the mass-selected $[Cu(OAc)(2\text{-}PhPy)_2]^+$ complex and theoretical IR spectra of b) $^{Cu}1_a$, c) $^{Cu}1_b$ and d) $^{Cu}3_b$. The line spectra are presented along with a Gaussian function with fwhm = 16 cm^{-1}.

non-activated intermediate ($^{Cu}1_a$) and the experimental spectrum. In particular, a strong correlation was found for the dominant peaks centered around 1490 cm^{-1}. In the theoretical spectrum these signals are largely the result of symmetric and asymmetric C-O stretches.

For both $^{Cu}1_b$ (Figure 4.46c) and $^{Cu}3_b$ (Figure 4.46d) structures the key peaks resulting from oxygen involvement are not represented experimentally. The clear experimental observation of $^{Cu}1_a$ is in line with the theoretically predicted potential energy surface where this isomer was by far the most stable. This observation strongly indicates the presence of collisionally induced C-H activation of 2-PhPy for the $[Cu(OAc)(2\text{-}PhPy)_2]^+$ complex.

The experimental IRMPD spectrum for $[Pd(OAc)(2\text{-}PhPy)_2]^+$ is shown in Figure 4.47a

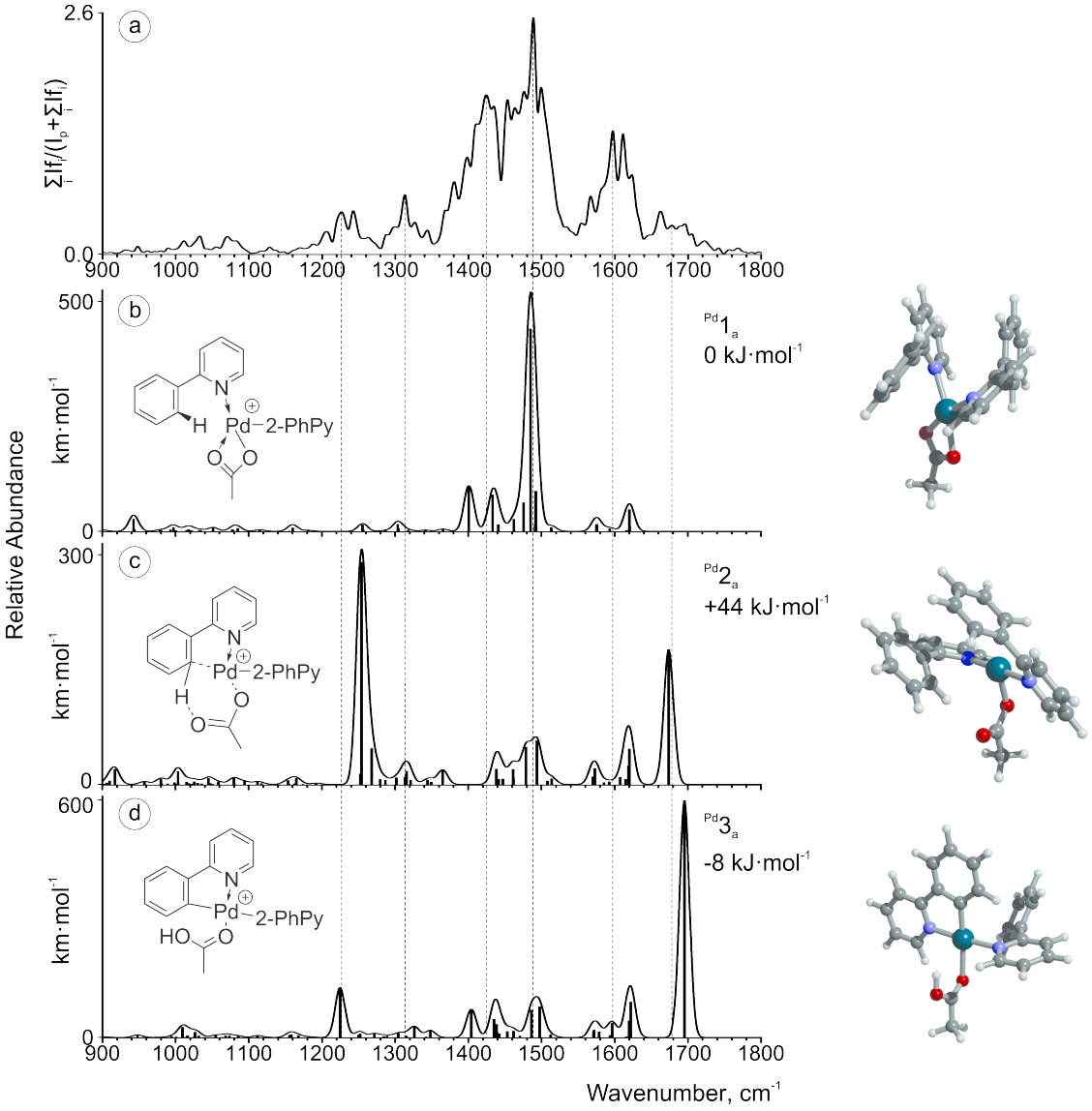

Figure 4.47: a) IRMPD spectrum of the mass-selected $[Pd(OAc)(2\text{-}PhPy)_2]^+$ complex and theoretical IR spectra of b) $^{Pd}1_a$, c) $^{Pd}2_a$ and d) $^{Pd}3_a$. The line spectra are presented along with a Gaussian function with fwhm = 16 cm^{-1}.

and is considerably more complicated than the spectra shown for the earlier examples. Its comparison with the calculated individual theoretical spectra does not provide an ideal match. Therefore it is possible that the experimental spectrum represents a contribution from two or more isomers. Analysis of the corresponding potential energy surface (Figure 4.44c) reveals that a mixed contribution is possible due to the small energy differences between structures $^{Pd}1_a$ and $^{Pd}3_a$. It seems that the experimental spectrum is dominated by the $^{Pd}1_a$ isomer with the large C-O stretching peak at 1485 cm^{-1}. The peaks at 1401 and 1433 cm^{-1} also match well and correspond to the C-H bending of acetic acid, while the peaks at 1575 and 1621 cm^{-1} correspond to C-C stretching modes of the 2-PhPy ligands.

The experimental bands that do not match with $^{Pd}1_a$ structure could result from the presence of the $^{Pd}3_a$ isomer. This isomer shows particularly good matches with the bands at 1225 and 1695 cm^{-1}, where the former results from a combination of a O-C-C asymmetric stretch and an O-H bend, while the latter corresponds to a C-O stretch involving the metal coordinated oxygen.

4.4.4 Comparison of the experimental and theoretical results

During our theoretical studies we have applied a number of methods and basis sets in order to better understand and theoretically describe the gas-phase behavior of the investigated ions. Table 4.8 summarizes some of the most important results. For clarity, the discussion below will be focused only on data obtained with the B3LYP-D2 method.

Table 4.8: Calculated and experimental activation energies for AcOH loss.

Method	Metal					
	Ru		Cu		Pd	
Experimental (CID), kJ·mol^{-1}	113 ± 3		138 ± 5		65 ± 3	
	E_{diss}	E_{TS}	E_{diss}	E_{TS}	E_{diss}	E_{TS}
B3LYP-D2, kJ·mol^{-1}	142	64	156	139	71	83
B3LYP-D3, kJ·mol^{-1}	-	-	152	143	64	82
B3LYP, kJ·mol^{-1}	103	67	111	140	29	74

For the ruthenium case a relatively small activation barrier was observed (64 kJ·mol^{-1}) and subsequent AcOH elimination required additional 78 kJ·mol^{-1}. Therefore we suggest that the measured *AE* for the AcOH loss (113 ± 3 kJ·mol^{-1}) reflects its dissociation from the ruthenium complex and not the C-H activation itself.

For the copper complex, the activation barrier (139 kJ·mol^{-1}) matches well with the experimentally obtained value (138 ± 5 kJ·mol^{-1}) and is on the order of the energy demand for the subsequent acetic acid loss (E_{rel}($^{Cu}4_a$ + AcOH) = 156 kJ·mol^{-1}). Experiments showed that the elimination of AcOH is less abundant than that of 2-PhPy, and also less energy demanding. This indicates that the C-H activation step is rate limiting and most likely reflects the *AE* that we observe experimentally.

Interpretation of results for the Pd complex is complicated by the fact that we observe a mixture of isomers. The experimentally observed *AE* value however is rather small, thus we believe that it is largely dominated by elimination of AcOH from the activated complex $^{Pd}3_a$.

It can be seen that the dispersion corrections have a large influence on the elimination channel of AcOH. On the other hand, the activation barriers change only slightly, regardless of the chosen method. According to Grimme's recent reports[191,192], dispersion coefficients for cations are overestimated which may increase the final dissociation energy value. However the combination of the B3LYP method and D2 dispersion corrections most closely resembles our experimental results, and the inclusion of dispersion corrections is strongly recommended[192] wherever non-covalent interactions are present.

4.4.5 Hammett studies

It has been shown that linear free energy correlations can be studied using mass spectrometry[193]. One of the most commonly used ways to study organic reaction mechanisms, also in the gas phase, is the Hammett equation and subsequent interpretation of the associated Hammett plots. Therefore we decided to study the ions of form $[M(2\text{-PhPy})(\text{acid-H})(L)]^+$ where acid corresponds to the *m*- and *p*- substituted benzoic acids. We generated the ions in the gas phase, mass-selected them, and studied their C-H activation upon CID. In order to obtain a reliable Hammett correlation, five or more benzoic acid derivatives should be studied (*e.g.* *m*-NO_2, *p*-NO_2, *m*-Cl, H, *p*-CH_3, *p*-CH_3O, where *p*-NO_2 and *p*-CH_3O derivatives are included in order to decide what type of σ constants should be used (σ, σ^+ or σ^-)).

First, we have investigated a large series of LCu(OAc)/2-PhPy/acid mixtures in acetonitrile to generate the above-mentioned intermediates. As an example, Figure 4.48 shows the spectrum obtained for the equimolar mixture of $Cu(OAc)_2$, 2-PhPy and 3-methoxybenzoic acid in acetonitrile. As can be seen from the spectrum, the ion at *m/z* 524 is formed, which could correspond to a $[Cu(3\text{-}OCH_3C_6H_4COO)(2\text{-PhPy})_2]^+$ cation. The CID of this ion leads to either elimination of 2-PhPy or 3-methoxybenzoic acid (Figure 4.49).

We have repeated the same procedure for generation of the peaks $[Cu(2\text{-PhPy})_2(\text{acid-H})]^+$, performed energy-resolved CID analysis and estimated AEs for the elimination of corresponding acid, for a chosen series of *p*- and *m*- substituted benzoic acids and the results of CID experiments are summarized in Table 4.9. The simulated breakdown curves for all of the benzoic acid derivatives can be found in Appendix A, Section 6.3.

As the table shows, the correlation between the obtained AE's and Hammett σ constants is rather poor. This is due to the fact that AEs are similar and differ in the range

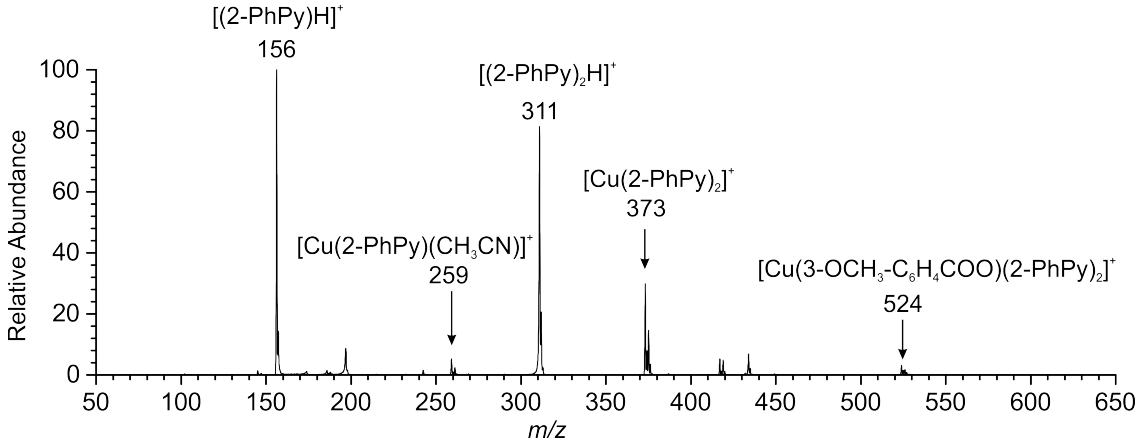

Figure 4.48: ESI-MS spectrum of the mixture of $Cu(OAc)_2$, 2-PhPy and 3-methoxybenzoic acid in acetonitrile.

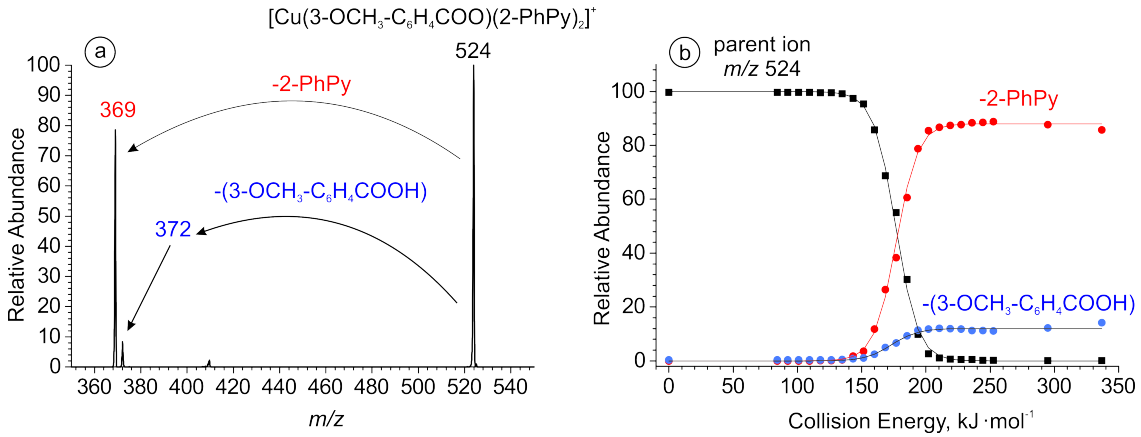

Figure 4.49: The CID spectrum of the mass selected peak at m/z 524 and its breakdown curve. AE for 3-methoxybenzoic acid loss: 152 ± 3 kJ·mol^{-1}; AE for 2-PhPy loss: 159 ± 3 kJ·mol^{-1}.

of experimental error which is 3-5 kJ·mol^{-1}. Therefore we decided to investigate the relationships between σ constants and relative cross-sections for each derivative that can be determined with a greater precision[40,194]. To this end, we determined the relative abundances of the fragment ions $[Cu(2\text{-}PhPy)(acid\text{-}H)]^+$ and $[Cu(2\text{-}PhPy)((2\text{-}PhPy)\text{-}H)]^+$ at a collision energy where the branching ratio has reached the plateau of the energy resolved CID curve (for example, at around 250 kJ·mol^{-1} for the breakdown curves shown in Figure 4.49). Then the logarithms of the extracted abundances were plotted against the corresponding σ constant.

Figure 4.50 shows the obtained Hammett plot for 2-PhPy loss. The Hammett ρ constant is -0.07 which points to a negligible effect that a substituent on the benzoate counter ion has on the binding energy between copper and 2-PhPy. Therefore we used the 2-PhPy

Table 4.9: Measured activation energies in $[Cu(acid\text{-}H)(2\text{-}PhPy)_2]^+$ for two losses and the corresponding Hammett constants.

Substituent	$AE_{\text{-acid}}$, kJ·mol^{-1}	$AE_{\text{-2-PhPy}}$, kJ·mol^{-1}	$\sigma_{m,p}$	$\sigma^+_{m,p}$
-H	149	157	0	0
p-NH_2	148	153	-0.66	-1.3
p-NO_2	152	163	0.78	0.78
p-OCH_3	155	157	-0.27	0.778
p-OH	148	156	-0.37	-0.92
p-$N(CH_3)_2$	148	151	-0.83	-1.7
m-OCH_3	152	159	0.12	0.12
m-OH	148	157	0.12	0.12
m-NO_2	157	162	0.71	0.71
m-Br	148	154	0.39	0.39

elimination to anchor the substituent effect for the C-H activation step: the logarithms of the branching ratios between the acid and 2-PhPy losses were plotted against the corresponding Hammett σ parameter (Figure 4.51).

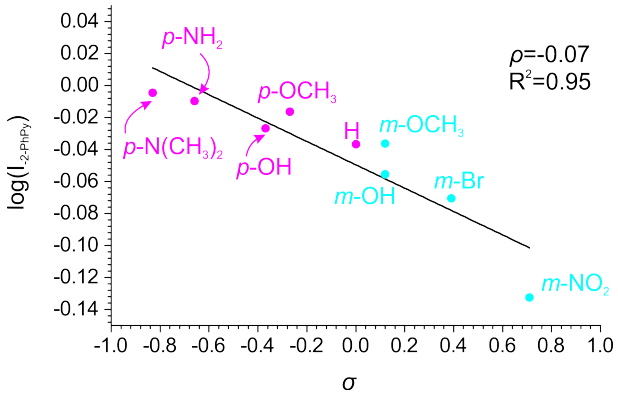

Figure 4.50: Hammett plot for Cu-catalyzed C-H activation of 2-phenylpyridine showing the dependence of the logarithm of the relative intensity of 2-PhPy loss at plateau *vs.* σ constant.

Figure 4.51a shows the Hammett plot created for the logarithm of branching ratio between the two elimination channels and the σ constant. The resulting ρ constant obtained form the plot is 0.93. As the ρ constant for C-H activation lies in the region $0<\rho<1$, the reaction is only weakly dependent on the electronic effects of the substituents. The small absolute value of ρ also indicates the low ionic character of the transition state which proves the cyclic character of our reaction. The plot shows that the ρ constant for C-H activation is positive, which implies that electron-withdrawing substituents (stronger acids) can accelerate the reaction. The use of σ^+ constants did not provide a better correlation

(Figure 4.51b) which shows that the resonance effect from the substituent to the reaction center does not play a pronounced role in this reaction.

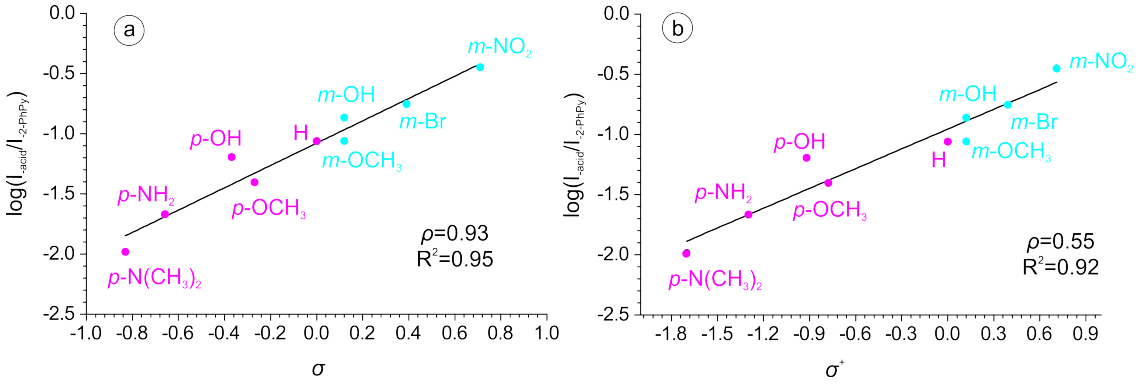

Figure 4.51: Hammett plots for the Cu-catalyzed C-H activation of 2-phenylpyridine showing the dependence of the logarithm of the branching ratio between acid and 2-phenylpyridine losses *vs.* a) the σ constant; b) the σ^+ constant.

Next, similarly to Cu-case, we decided perform Hammett studies on Ru and Pd-catalyzed C-H activation. To this end, we generated the ions of the form [Ru(2-PhPy)(acid-H)(C_6H_6)]$^+$ and subjected them to CID analysis. However, the behavior of the breakdown curves was not possible to model with the sigmoid functions. This might be due to the peak overlaps, caused by rather large isolation width (10 m/z) that had to be used in order to obtain ion intensity sufficient for MS^2 experiments. The same situation was true for the palladium case (*e.g.* ions of the form [Pd(2-PhPy)$_2$(acid-H)]$^+$) , moreover some of the [Pd(2-PhPy)$_2$(acid-H)]$^+$ ions showed no acid elimination, and underwent CO_2 loss instead. Therefore we proceeded with the Cu-catalyzed C-H activation of 2-PhPy, as the measured AEs agree well with theory and also reflect a C-H activation step.

In order to investigate the role of the metal-carbon bond formation in greater detail, we have reoptimized the structures for C-H activation using benzoate and 4-nitrobenzoate counter ions. We have found that in the 6-membered transition states, with all three of the metals, the presence of the NO_2 substituent decreased the metal-carbon distance while the metal-oxygen and carbon-hydrogen distances both increased. These observations are in line with the theorized increasingly electrophilic metal center. The presence of NO_2 also reduced the energy required for 4-nitrobenzoic acid loss in comparison with benzoic acid in the case of each investigated metal. This further supports the experimental observation of an increasingly electrophilic metal center (see Scheme 4.12).

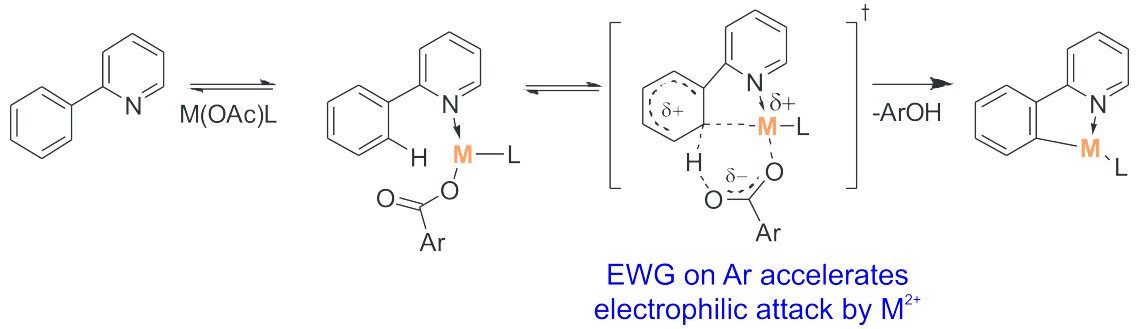

Scheme 4.12: Schematic representation of the carboxylate assisted C-H activation investigated here.

Chapter 5

Conclusion

The studies described in this dissertation represent some of the fundamental findings for organometallic chemistry research. The employment of ESI-MS, IRMPD and quantum chemical calculations can be very helpful for the investigation of reaction mechanisms. Our results show that one also needs to be careful while interpreting and applying them to the specific cases.

The studies of $Cu(OAc)_2$ behavior in dry organic solvents (methanol and acetonitrile) revealed a high degree of clusterization, and that the clusters with three to six copper atoms dominate the spectra. The abundance of these clusters however is strongly dependent on the presence of water in the solution: even small water contents significantly suppress the amount of clusters. Monomeric copper complexes become dominant with the water contents of 5 vol%. This finding could be important for further investigations of reaction mechanisms catalyzed by copper acetate and help in distinguishing between single-atom and cluster chemistry for what is driving the catalytic cycle.

In the second study - investigation of copper catalyzed cross coupling between thiol esters and boronic acids - we were able to follow the kinetics of the reaction and determine the concentration changes of reactants and products. The investigation of reaction intermediates was not very successful, probably as the result of either a high abundance of sodiated ions in the spectra, or because of the high reactivity of copper-boronate complexes. Although the copper complexes were little abundant, we profited from the large intensities of reagent and product complexes with sodium. This fact allowed us to monitor the reaction kinetics with ESI-MS and obtain the rate constants at different temperatures. The determined activation energy for the reaction according to the Arrhenius equation was found to be 81 $\pm$ 5 kJ$\cdot$mol^{-1}. The Gibbs energy at 298K was determined as 103 $\pm$ 5

$kJ \cdot mol^{-1}$, activation enthalpy as 76 ± 5 $kJ \cdot mol^{-1}$ and the activation entropy yielded -100 ± 5 $J \cdot mol^{-1} \cdot K^{-1}$.

In the third project, an investigation of complexes with three isomeric phenylpyridines and Ni^{2+} cations was carried out. The study revealed that 3- and 4-PhPy behave similarly to each other, however 2-PhPy differs in two ways. First, the steric hindrance of 2-PhPy prevents the formation of the three- and higher ligated species. Second, in the nickel-2-PhPy complexes one of the *o*-C-H bonds of the phenyl ring comes in close proximity to the metal center which enables activation of the C-H bond and formation of a metallocycle. IM-MS was found to be a useful method for the investigation of the coordination and steric effects for the isomeric organometallic complexes, such as $[NiCl(PhPy)_2]^+$.

The last study was into the gas-phase mechanism of carboxylate assisted C-H activation. We have shown that the carboxylate assisted C-H activation of 2-phenylpyridine can be studied in the gas phase with ruthenium, copper, and palladium catalysts. IRMPD spectroscopy confirmed that isolation of ruthenium acetate and copper acetate complexes with non-activated 2-phenylpyridine is possible. It was also possible to induce the C-H activation of these complexes in the collision cell and study it in greater detail. We have determined the energies required for C-H activation and subsequent acetic acid elimination. In the case of palladium, we have observed a mixture of activated and non-activated complexes with 2-PhPy. Further careful analysis revealed that the experimentally observed appearance energy for AcOH loss in the cases of Ru and Pd reflects the binding energy of acetic acid to the metal center after the C-H activation step. On the other hand the energy determined for copper complexes reflects the energy needed for C-H activation. Potential energy surfaces for each of the C-H activation cases were constructed using DFT calculations. Similar structures were found for all three metals along the reaction coordinate, however their relative energies are very different.

The C-H activation step was also studied using Hammett plots for copper complexes with a series of substituted benzoates. The results show that electron-withdrawing substituents at the benzoate counter ion accelerate the C-H activation step. The explanation can be found in the cyclic nature of the transition structure, where C-H bond dissociation is assisted by the formation of a metal-carbon bond. Carboxylates derived from stronger acids further support the formation of the metal-carbon bond.

Chapter 6

Appendix A. Supplementary experimental data

6.1 Investigation of copper catalyzed aerobic cross coupling of thiol esters and arylboronic acids

Breakdown curves obtained for calibration

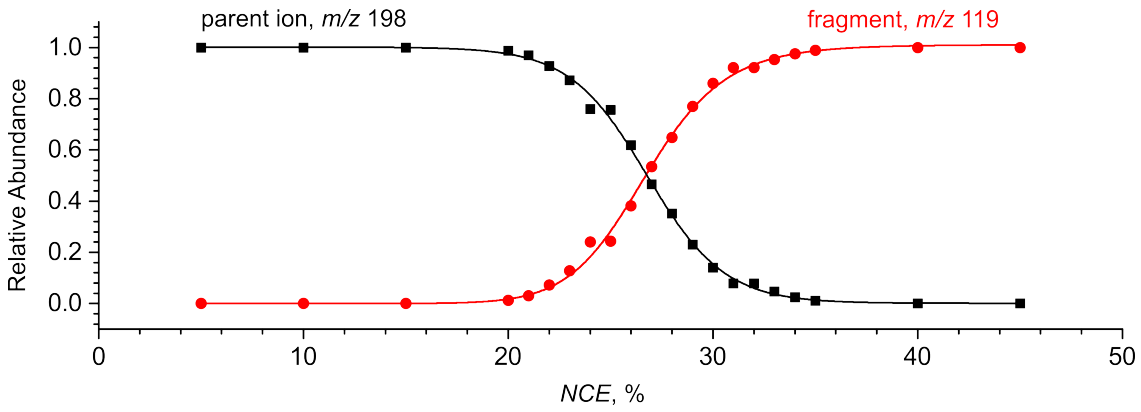

Figure 6.1: Breakdown diagram obtained for mass-selected [2,5-dimethylC_6H_3-CH_2-NC_5H_5]$^+$ as a function of the *NCE*. The dots represent the experimental data; the solid lines - the sigmoid functions used for analysis.

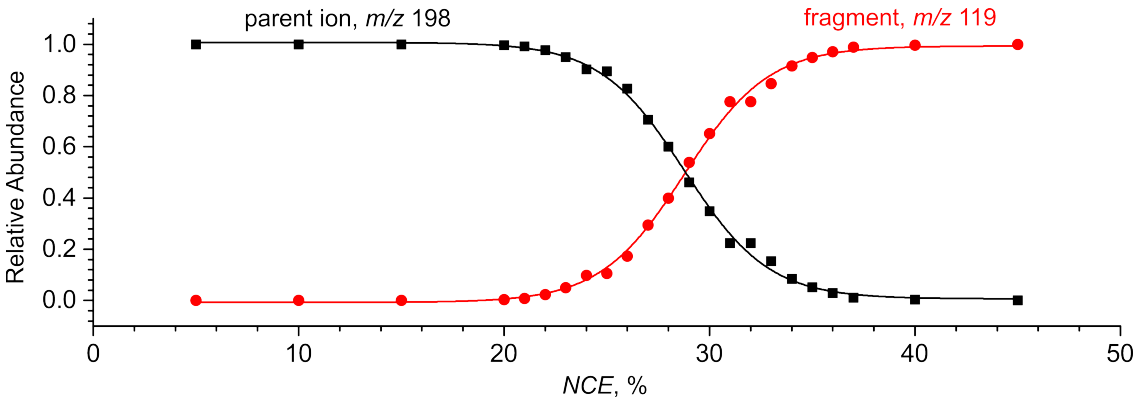

Figure 6.2: Breakdown diagram obtained for mass-selected [3,5-dimethylC_6H_3-CH_2-NC_5H_5]$^+$ as a function of the *NCE*. The dots represent the experimental data; the solid lines - the sigmoid functions used for analysis.

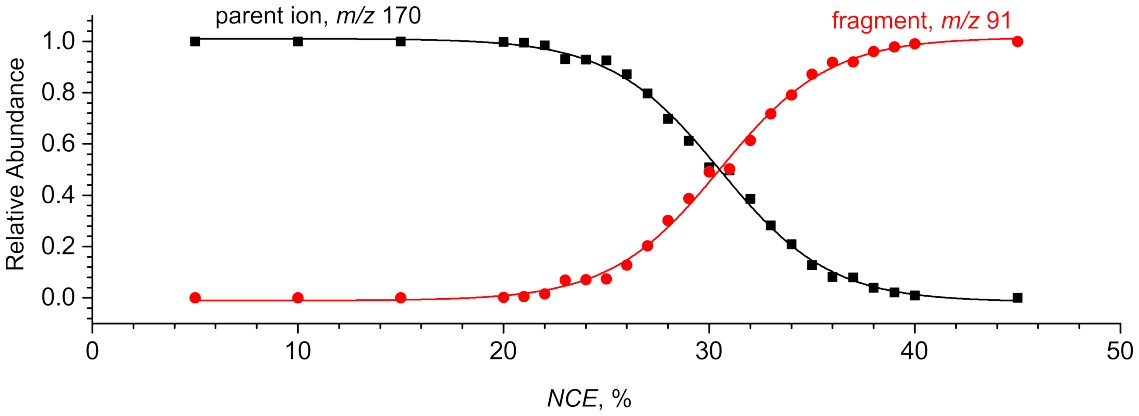

Figure 6.3: Breakdown diagram obtained for mass-selected [C_6H_5-CH_2-NC_5H_5]$^+$ as a function of the *NCE*. The dots represent the experimental data; the solid lines - the sigmoid functions used for analysis.

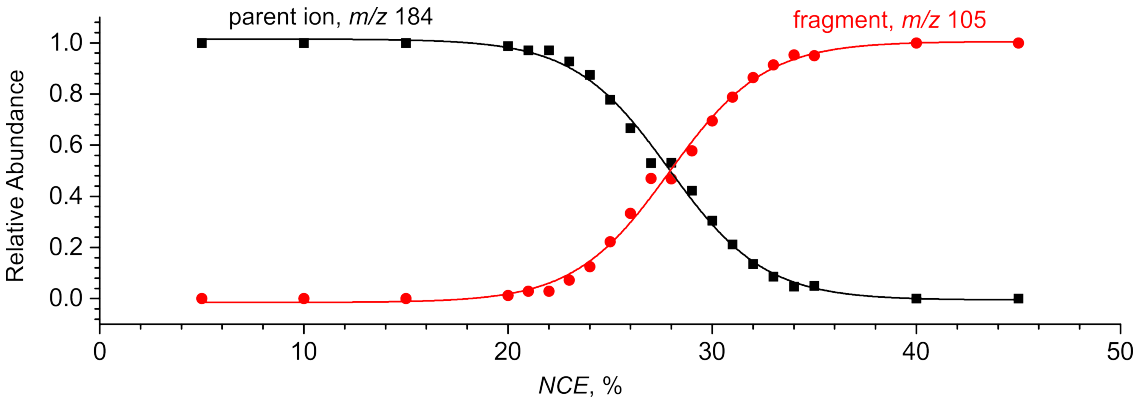

Figure 6.4: Breakdown diagram obtained for mass-selected [*o*-CH_3-C_6H_4-CH_2-NC_5H_5]$^+$ as a function of the *NCE*. The dots represent the experimental data; the solid lines - the sigmoid functions used for analysis.

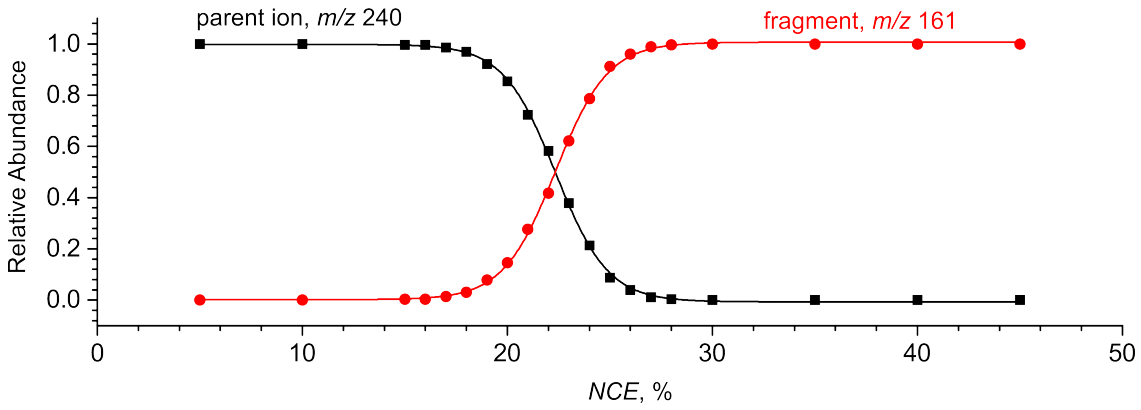

Figure 6.5: Breakdown diagram obtained for mass-selected $[C_6(CH_3)_5\text{-}CH_2\text{-}NC_5H_5]^+$ as a function of the *NCE*. The dots represent the experimental data; the solid lines - the sigmoid functions used for analysis.

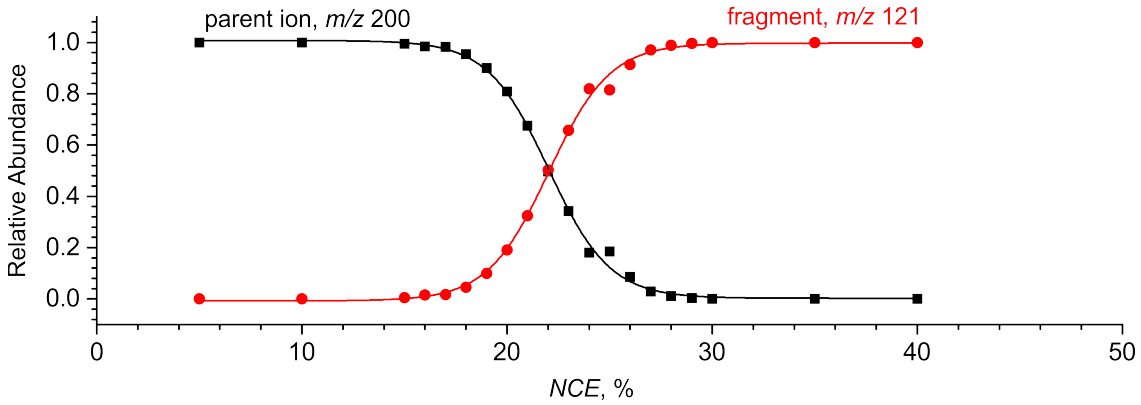

Figure 6.6: Breakdown diagram obtained for mass-selected $[p\text{-}OCH_3\text{-}C_6H_4\text{-}CH_2\text{-}NC_5H_5]^+$ as a function of *NCE*. The dots represent the experimental data; the solid lines - the sigmoid functions used for analysis.

6.2 Coordination and bond activation in complexes of regioisomeric phenylpyridines with nickel(II)

Breakdown curves obtained for calibration

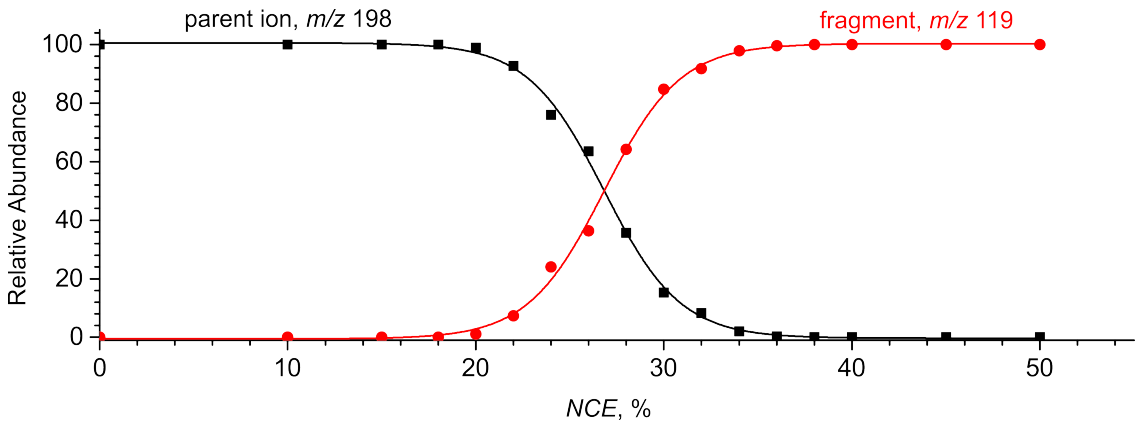

Figure 6.7: Breakdown diagram obtained for mass-selected [2,5-dimethylC_6H_3-CH_2-NC_5H_5]$^+$ as a function of the *NCE*. The dots represent the experimental data; the solid lines - the sigmoid functions used for analysis.

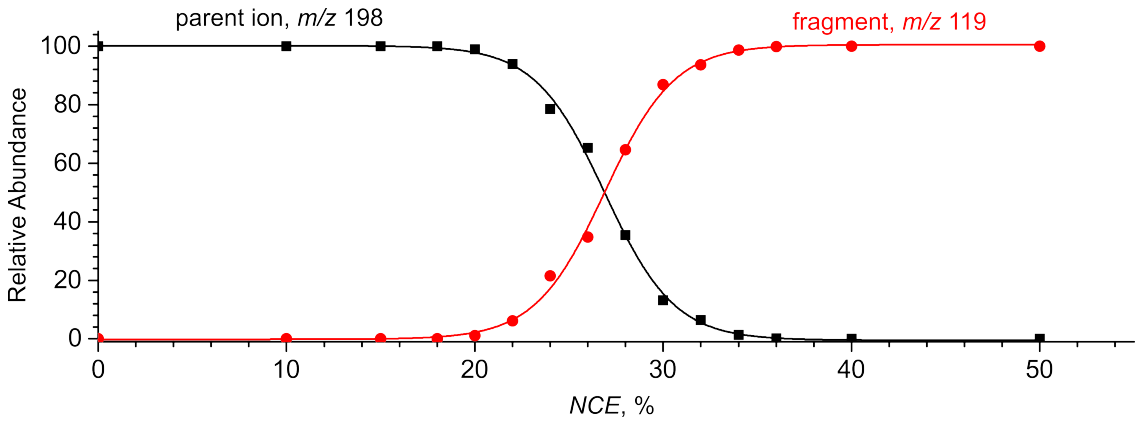

Figure 6.8: Breakdown diagram obtained for mass-selected [3,5-dimethylC_6H_3-CH_2-NC_5H_5]$^+$ as a function of the *NCE*. The dots represent the experimental data; the solid lines - the sigmoid functions used for analysis.

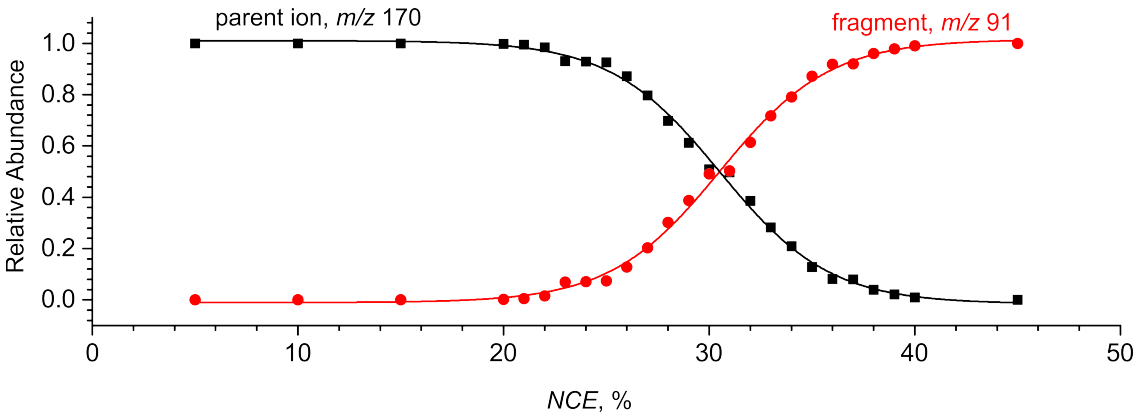

Figure 6.9: Breakdown diagram obtained for mass-selected $[C_6H_5\text{-}CH_2\text{-}NC_5H_5]^+$ as a function of the *NCE*. The dots represent the experimental data; the solid lines - the sigmoid functions used for analysis.

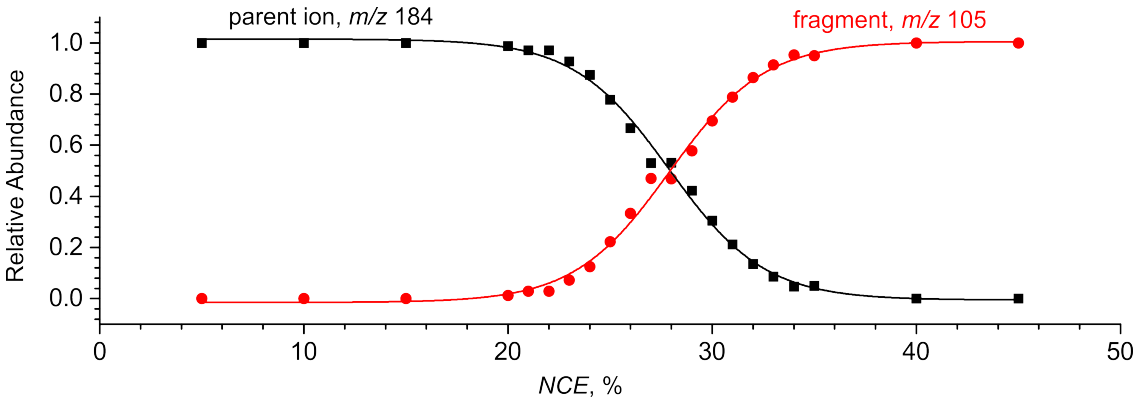

Figure 6.10: Breakdown diagram obtained for mass-selected $[o\text{-}CH_3\text{-}C_6H_4\text{-}CH_2\text{-}NC_5H_5]^+$ as a function of the *NCE*. The dots represent the experimental data; the solid lines - the sigmoid functions used for analysis.

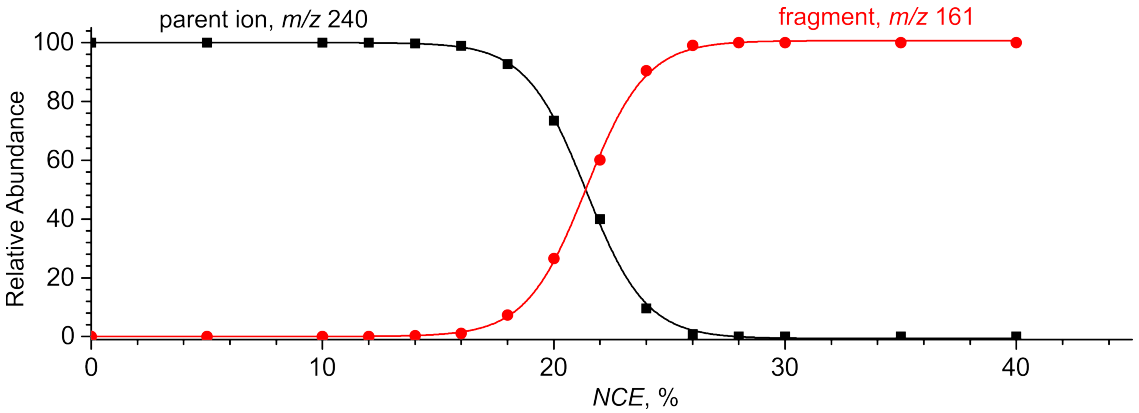

Figure 6.11: Breakdown diagram obtained for mass-selected $[C_6(CH_3)_5\text{-}CH_2\text{-}NC_5H_5]^+$ as a function of the *NCE*. The dots represent the experimental data; the solid lines - the sigmoid functions used for analysis.

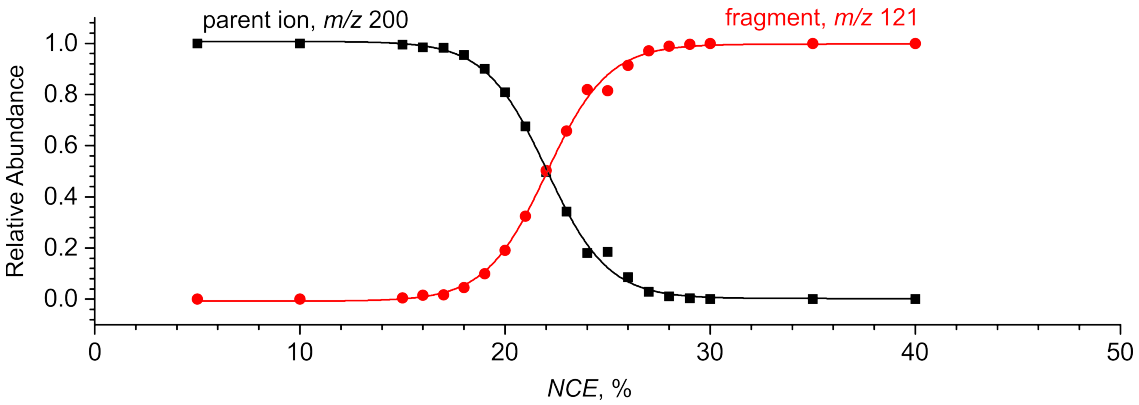

Figure 6.12: Breakdown diagram obtained for mass-selected $[p\text{-}OCH_3\text{-}C_6H_4\text{-}CH_2\text{-}NC_5H_5]^+$ as a function of the *NCE*. The dots represent the experimental data; the solid lines - the sigmoid functions used for analysis.

Representative simulated breakdown diagrams for Ni(II) complexes

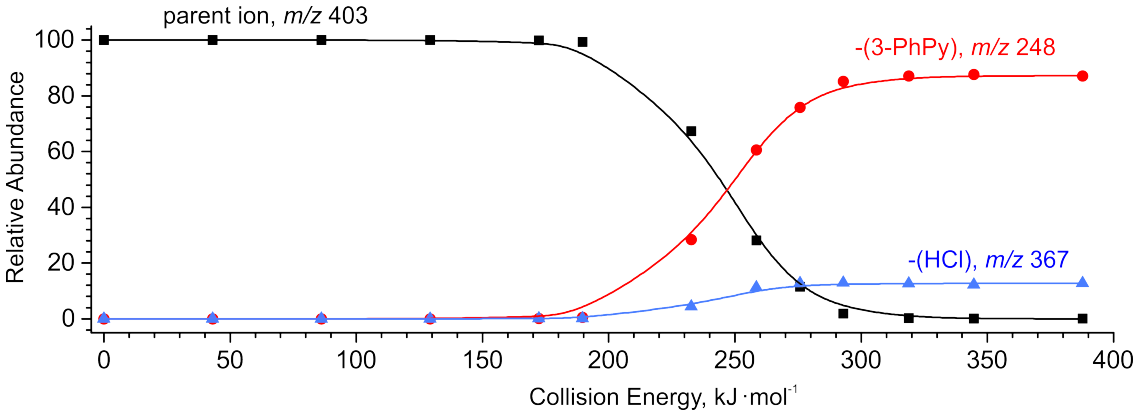

Figure 6.13: Simulated breakdown curves of the mass-selected $[NiCl(3\text{-}PhPy)_2]^+$ (m/z = 403) with two fragmentation channels: the loss of HCl (product ion with m/z = 367) and 3-PhPy (product ion with m/z = 248).

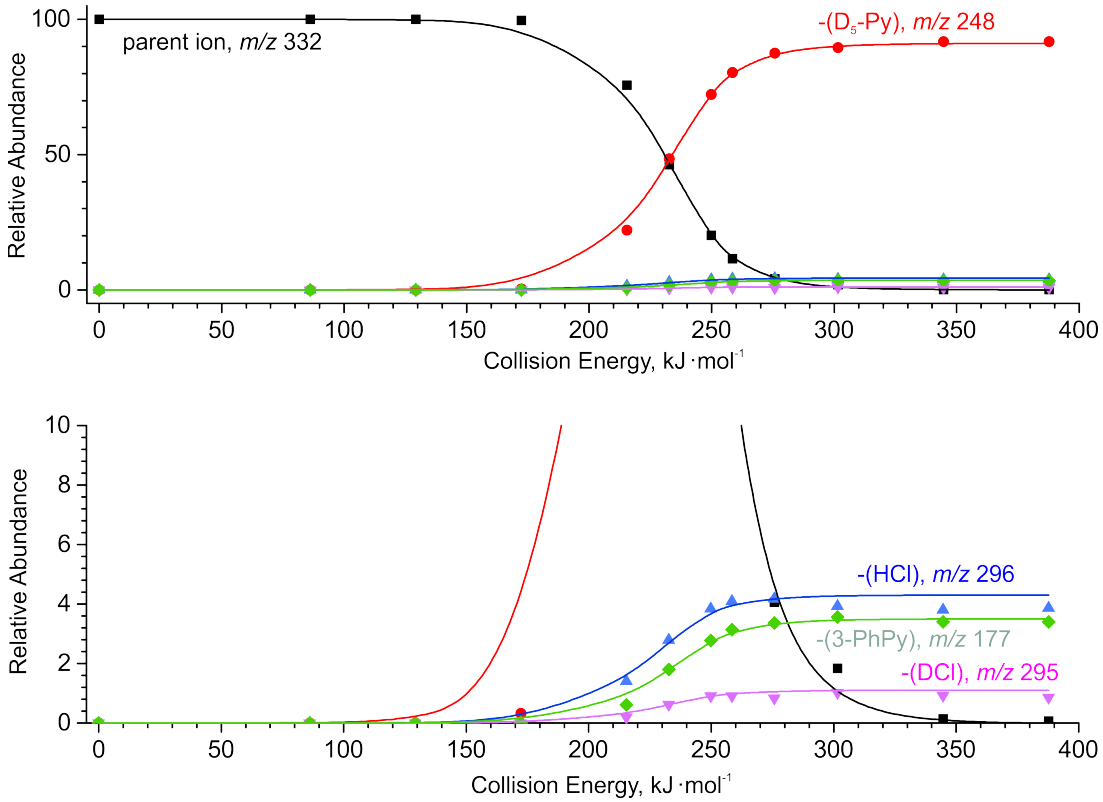

Figure 6.14: Simulated breakdown curves of the mass-selected $[NiCl(3\text{-}PhPy)(D_5\text{-}Py)]^+$ (m/z = 332) with four fragmentation channels: the loss of HCl (product ion with m/z = 296), D_5-Py (product ion with m/z = 248), 3-PhPy (product ion with m/z = 177) and DCl (product ion with m/z = 295).

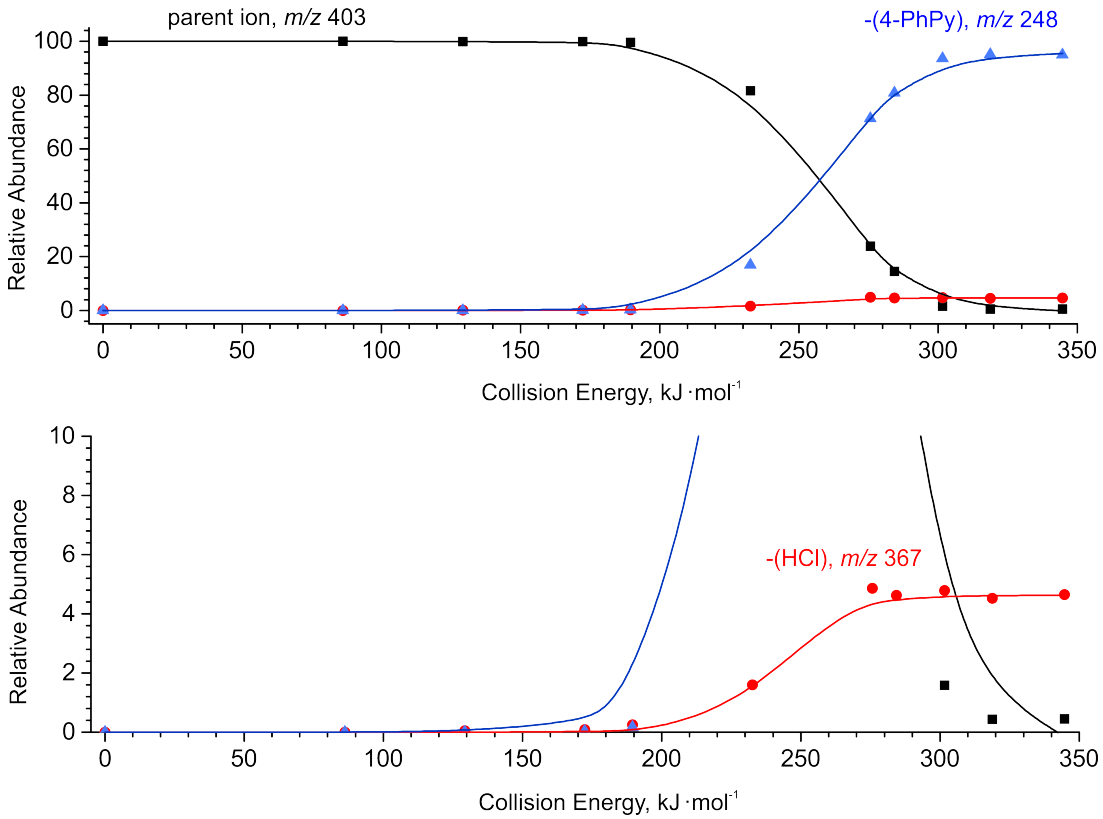

Figure 6.15: Simulated breakdown curves of the mass-selected $[NiCl(4\text{-}PhPy)_2]^+$ (m/z = 403) with two fragmentation channels: the loss of HCl (product ion with m/z = 367) and 3-PhPy (product ion with m/z = 248).

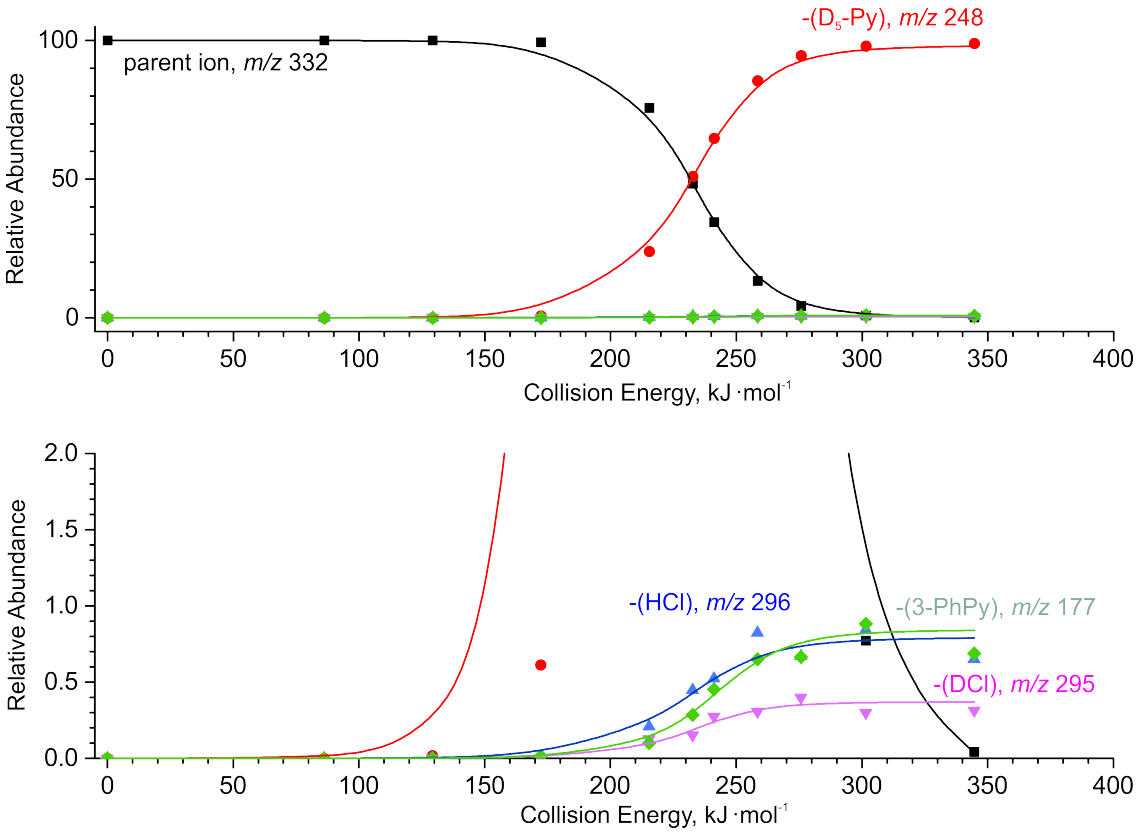

Figure 6.16: Simulated breakdown curves of the mass-selected $[NiCl(4\text{-}PhPy)(D_5\text{-}Py)]^+$ (m/z = 332) with four fragmentation channels: the loss of HCl (product ion with m/z = 296), D_5-Py (product ion with m/z = 248), 4-PhPy (product ion with m/z = 177) and DCl (product ion with m/z = 295).

6.3 Carboxylate assisted C-H activation of phenylpyridines with copper, palladium and ruthenium

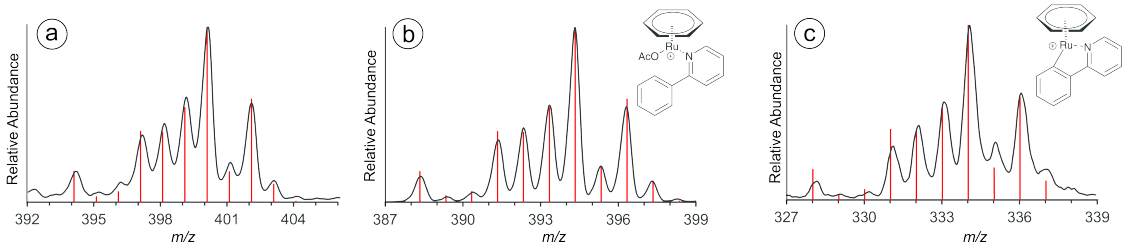

Figure 6.17: Isotope patterns of the investigated Ru-ions presented in Section4.4 (the red bars show the theoretical isotope patterns corresponding to the suggested ionic structures). a) $[(C_6H_6)RuOAc(Et_3N)(AcOH)]^+$; b) $[(C_6H_6)RuOAc(2\text{-}PhPy)]^+$; c) $[(C_6H_6)Ru((2\text{-}PhPy)\text{-}H)]^+$.

Breakdown curves obtained for calibration with the isolation width 1 m/z

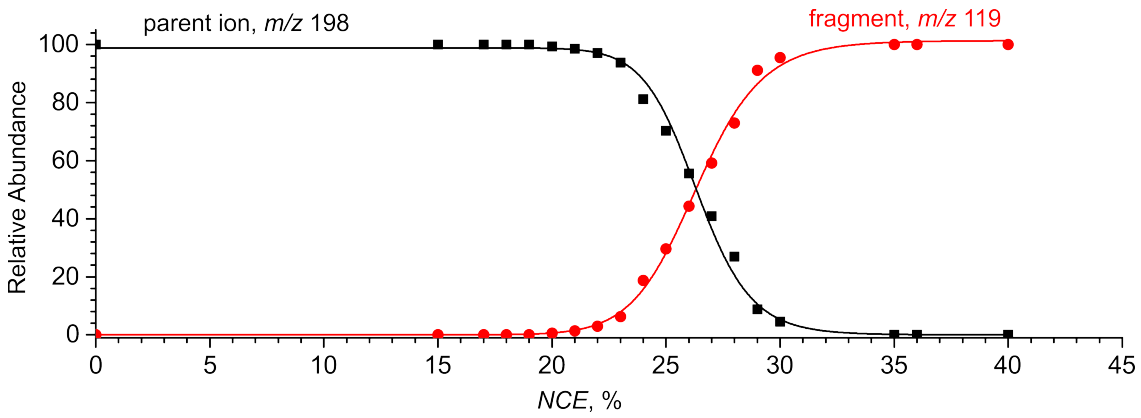

Figure 6.18: Breakdown diagram obtained for mass-selected [2,5-dimethylC_6H_3-CH_2-NC_5H_5]$^+$ as a function of the *NCE*. The dots represent the experimental data; the solid lines - the sigmoid functions used for analysis.

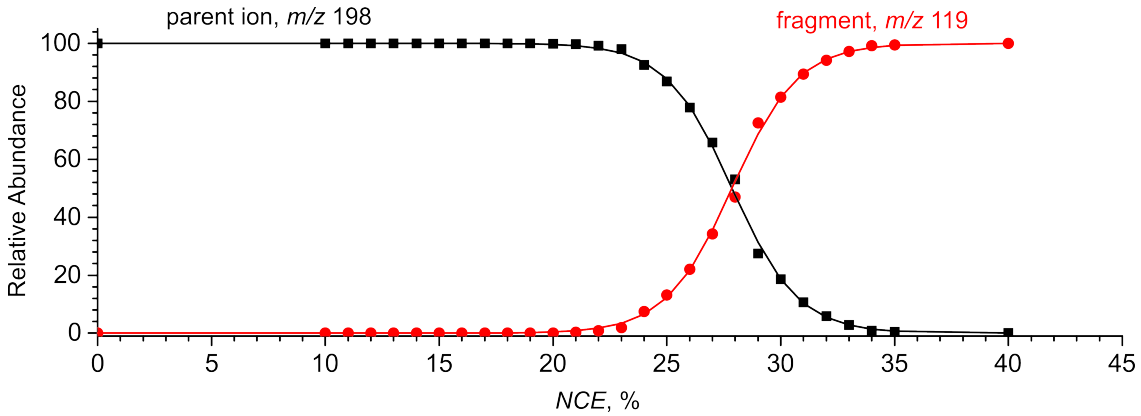

Figure 6.19: Breakdown diagram obtained for mass-selected [3,5-dimethylC_6H_3-CH_2-NC_5H_5]$^+$ as a function of the *NCE*. The dots represent the experimental data; the solid lines - the sigmoid functions used for analysis.

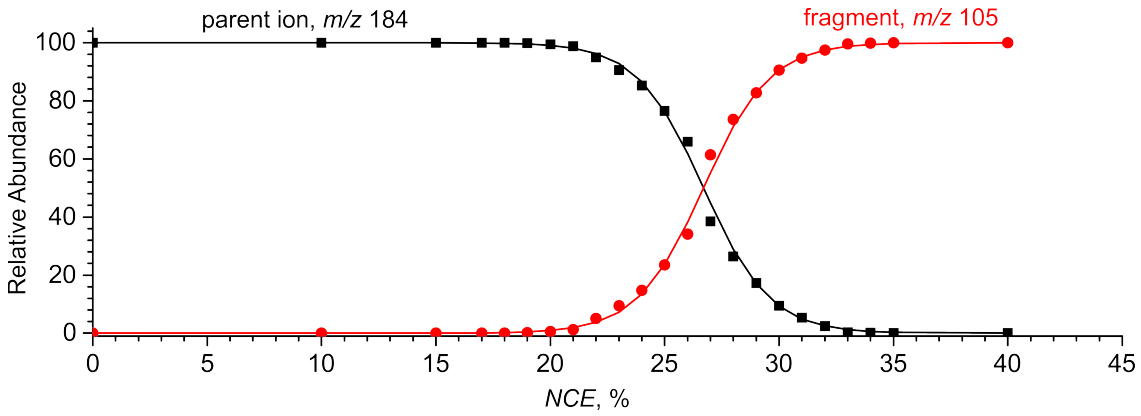

Figure 6.20: Breakdown diagram obtained for mass-selected $[o\text{-}CH_3\text{-}C_6H_4\text{-}CH_2\text{-}NC_5H_5]^+$ as a function of the *NCE*. The dots represent the experimental data; the solid lines - the sigmoid functions used for analysis.

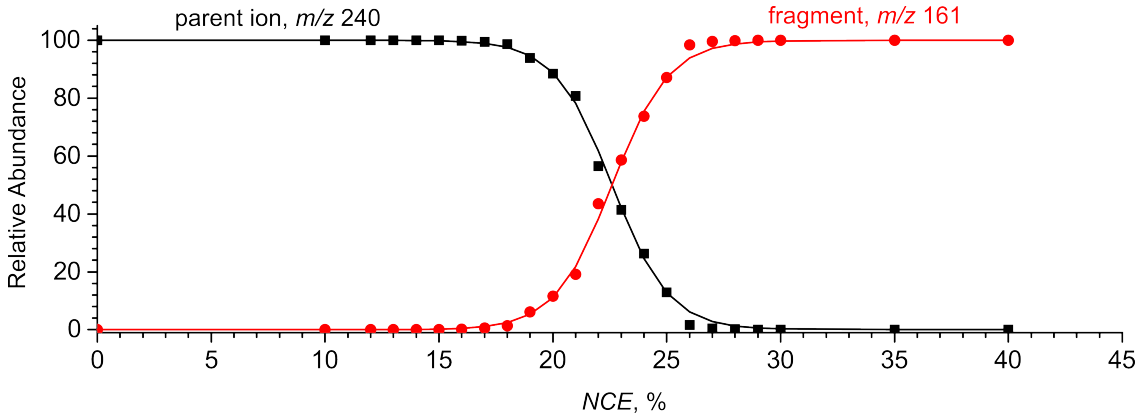

Figure 6.21: Breakdown diagram obtained for mass-selected $[C_6(CH_3)_5\text{-}CH_2\text{-}NC_5H_5]^+$ as a function of the *NCE*. The dots represent the experimental data; the solid lines - the sigmoid functions used for analysis.

Breakdown curves obtained for calibration with the isolation width 10 *m/z*

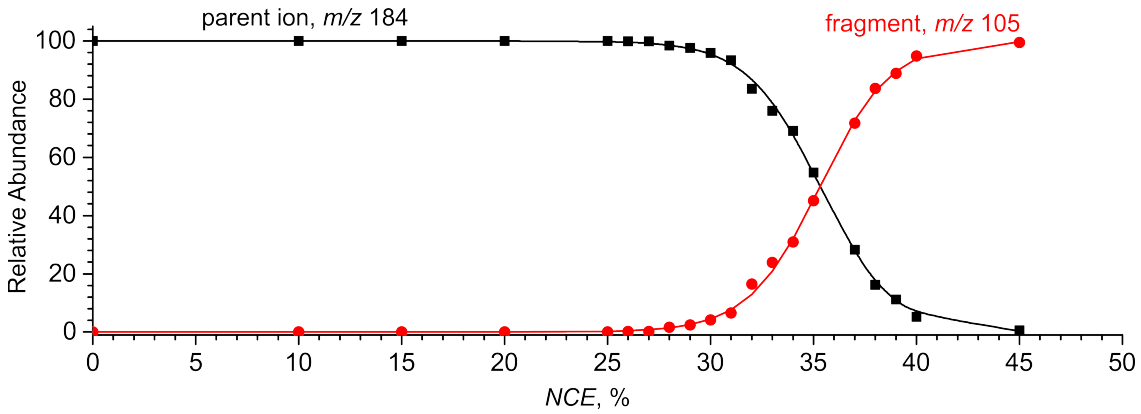

Figure 6.22: Breakdown diagram obtained for mass-selected $[o\text{-}CH_3\text{-}C_6H_4\text{-}CH_2\text{-}NC_5H_5]^+$ as a function of the *NCE*. The dots represent the experimental data; the solid lines - the sigmoid functions used for analysis.

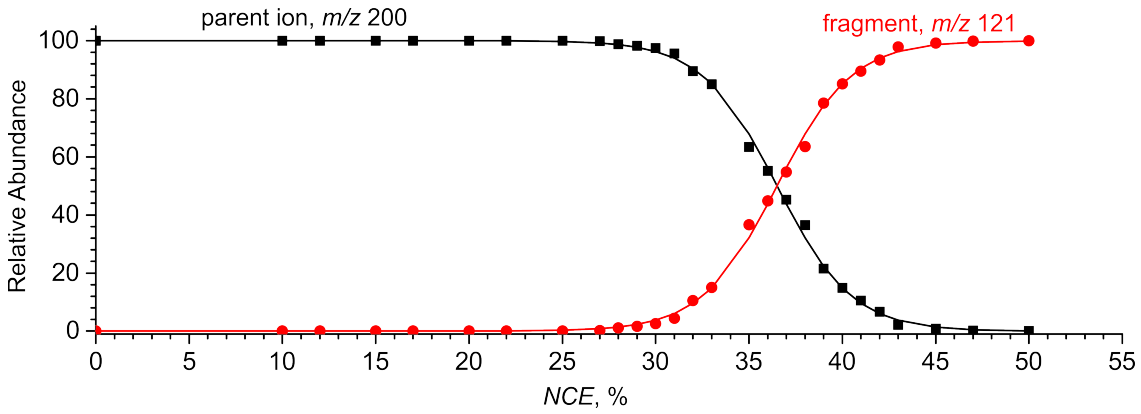

Figure 6.23: Breakdown diagram obtained for mass-selected $[m\text{-}OCH_3\text{-}C_6H_4\text{-}CH_2\text{-}NC_5H_5]^+$ as a function of the *NCE*. The dots represent the experimental data; the solid lines - the sigmoid functions used for analysis.

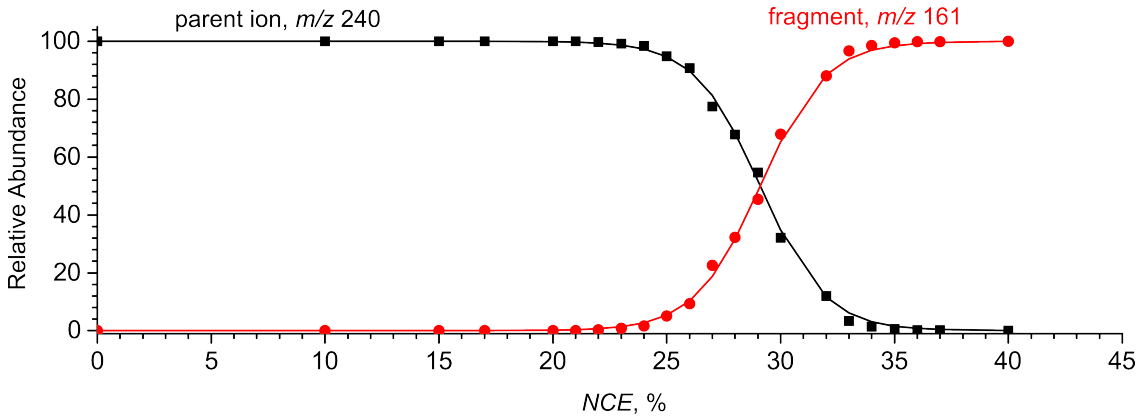

Figure 6.24: Breakdown diagram obtained for mass-selected $[C_6(CH_3)_5\text{-}CH_2\text{-}NC_5H_5]^+$ as a function of the *NCE*. The dots represent the experimental data; the solid lines - the sigmoid functions used for analysis.

Representative simulated breakdown diagrams obtained for Hammett study

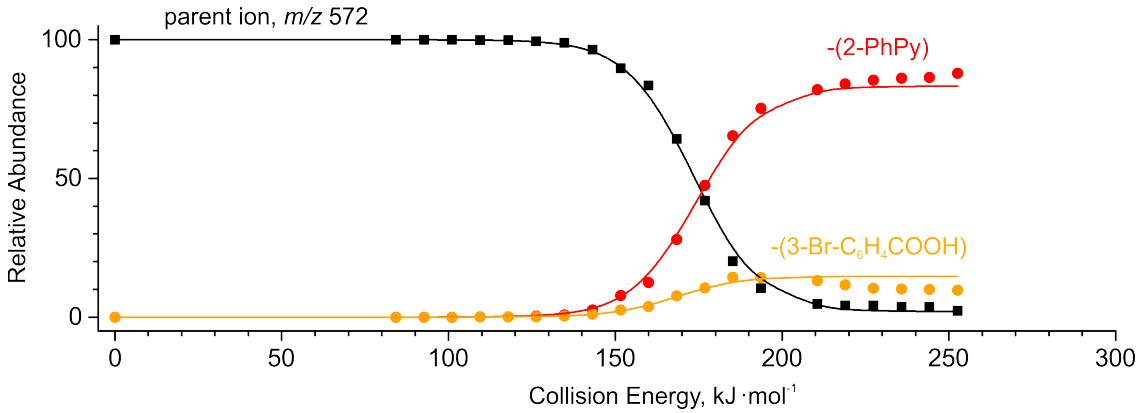

Figure 6.25: The breakdown curve for the mass selected peak at m/z 572 (3-bromobenzoic acid derivative).

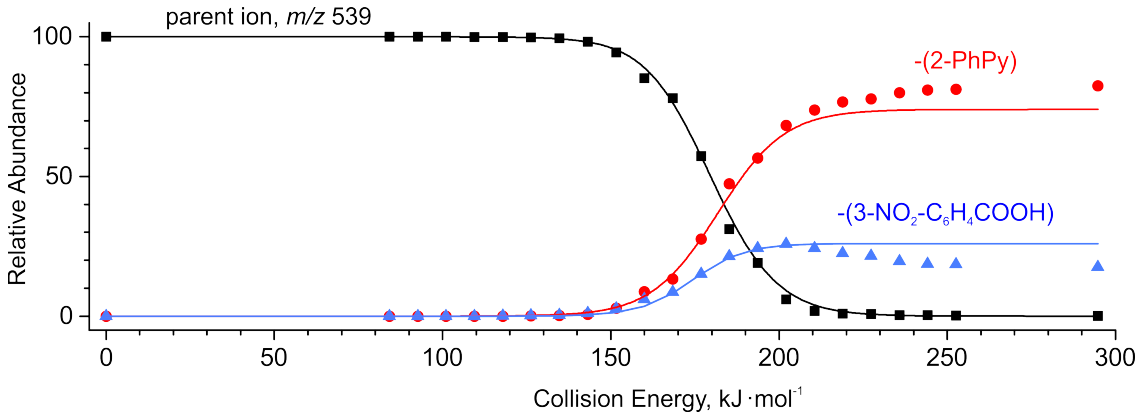

Figure 6.26: The breakdown curve for the mass selected peak at m/z 539 (3-nitrobenzoic acid derivative).

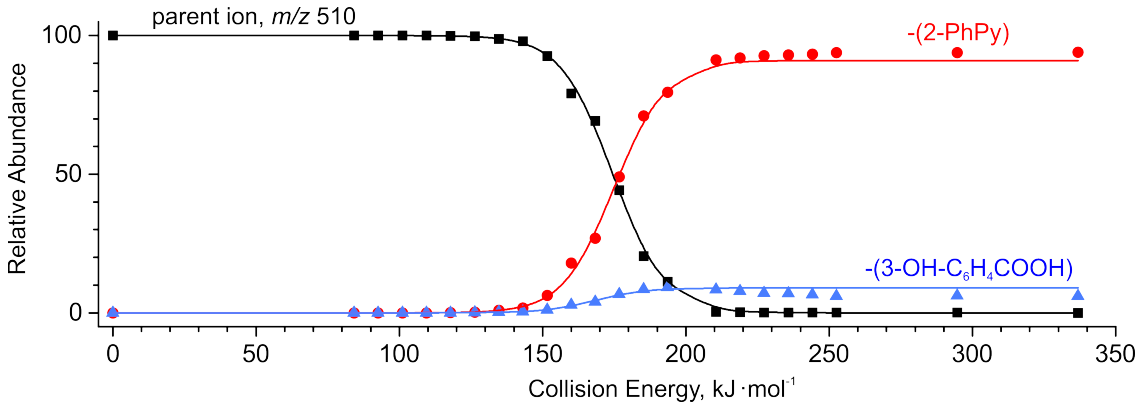

Figure 6.27: The breakdown curve for the mass selected peak at m/z 510 (3-hydroxybenzoic acid derivative).

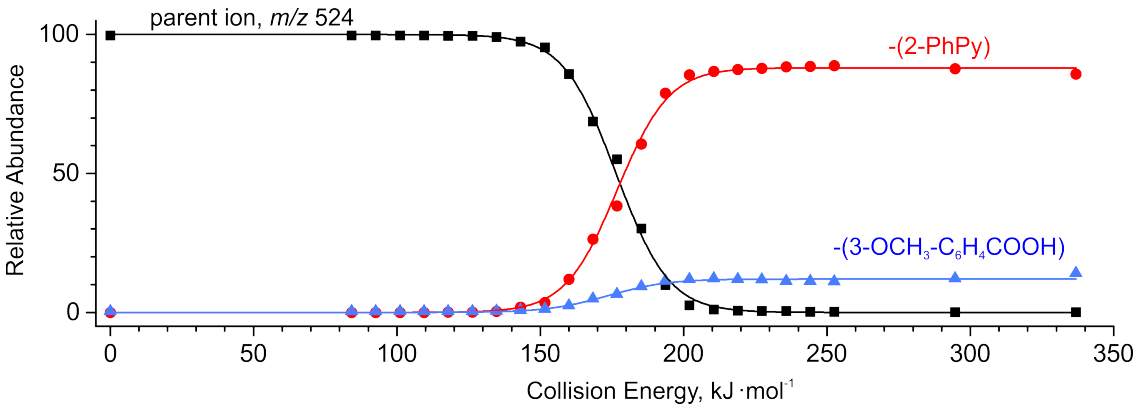

Figure 6.28: The breakdown curve for the mass selected peak at m/z 524 (3-methoxybenzoic acid derivative).

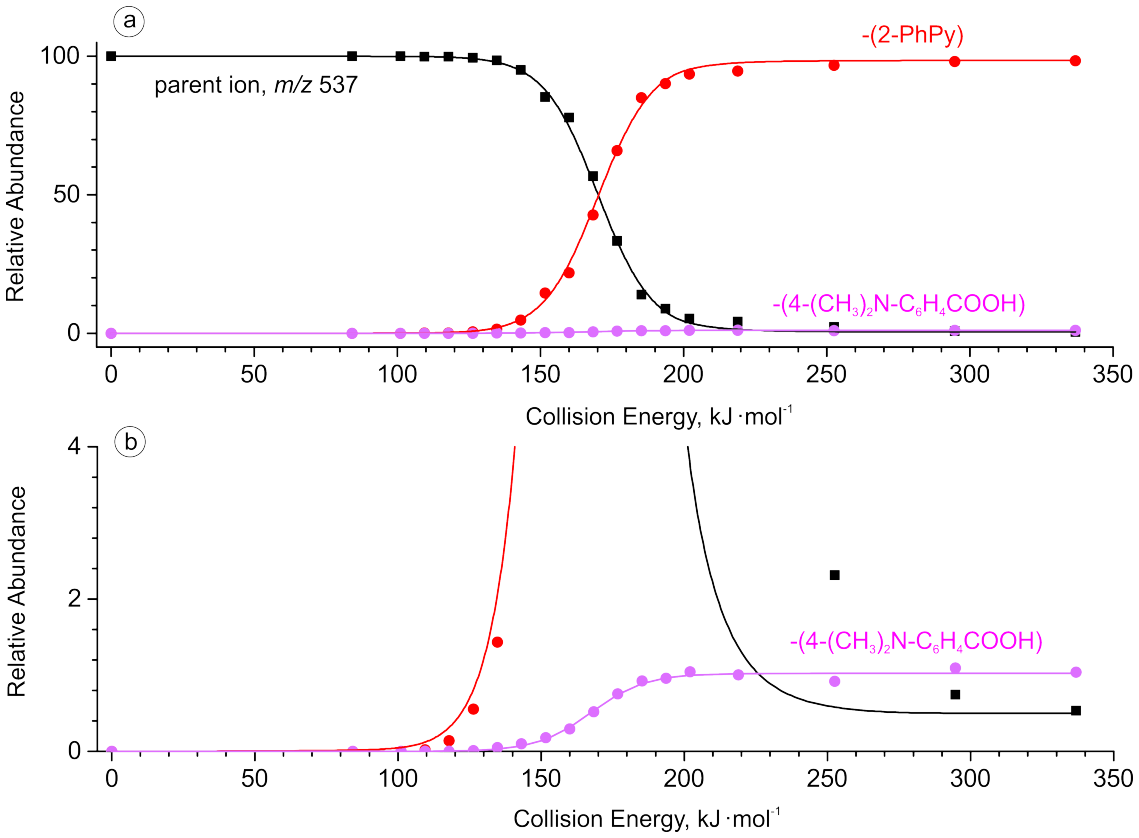

Figure 6.29: The breakdown curve for the mass selected peak at m/z 537 (4-dimethylaminobenzoic acid derivative); a) full scale; b) enlarged.

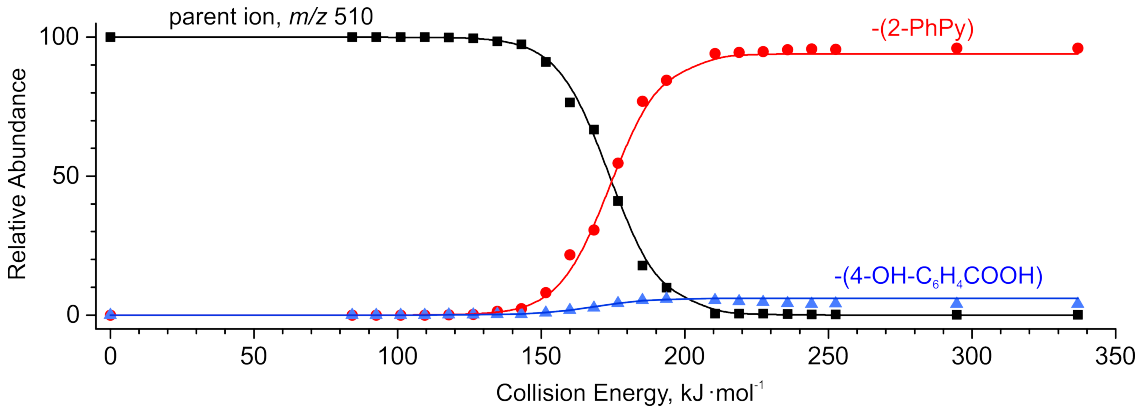

Figure 6.30: The breakdown curve for the mass selected peak at m/z 510 (4-hydroxybenzoic acid derivative).

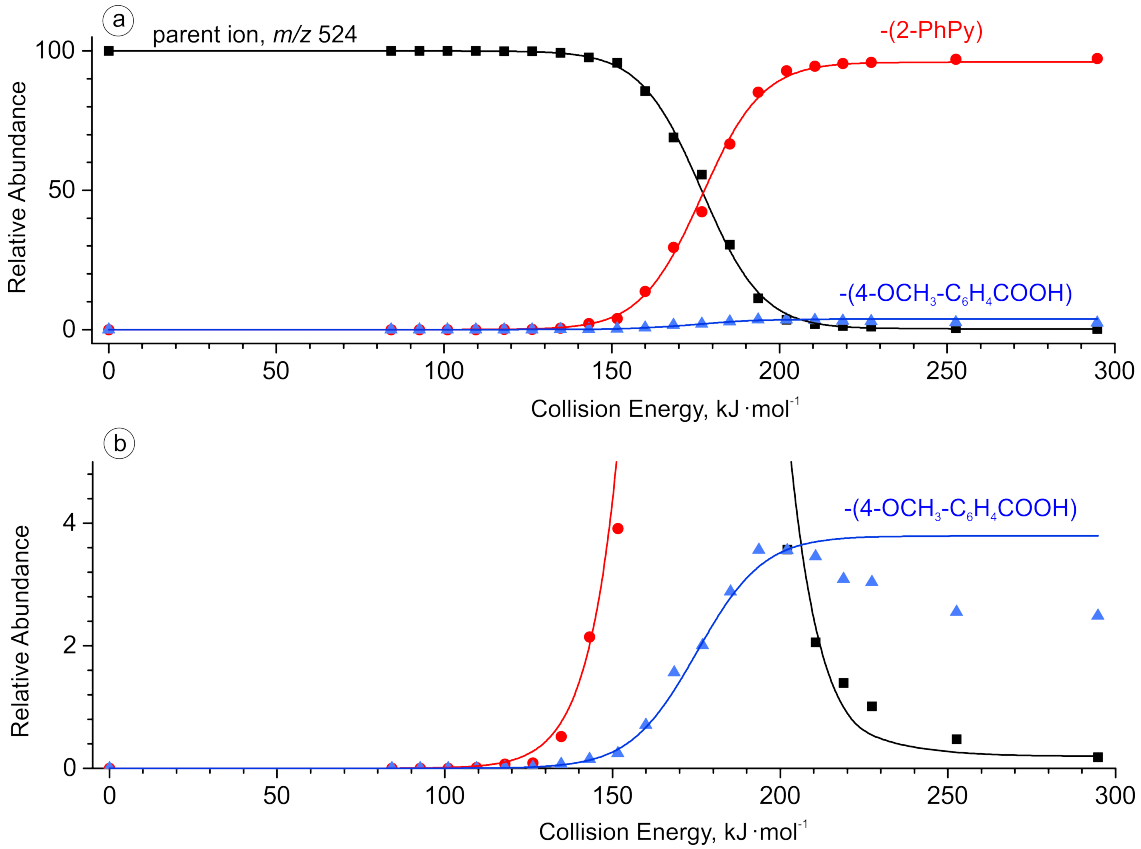

Figure 6.31: The breakdown curve for the mass selected peak at m/z 524 (4-methoxybenzoic acid derivative); a) full scale; b) enlarged.

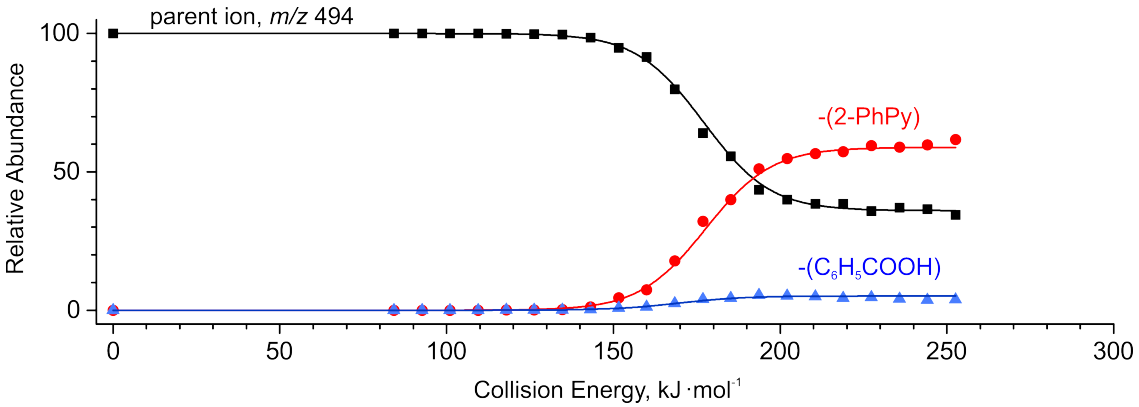

Figure 6.32: The breakdown curve for the mass selected peak at m/z 494 (benzoic acid derivative).

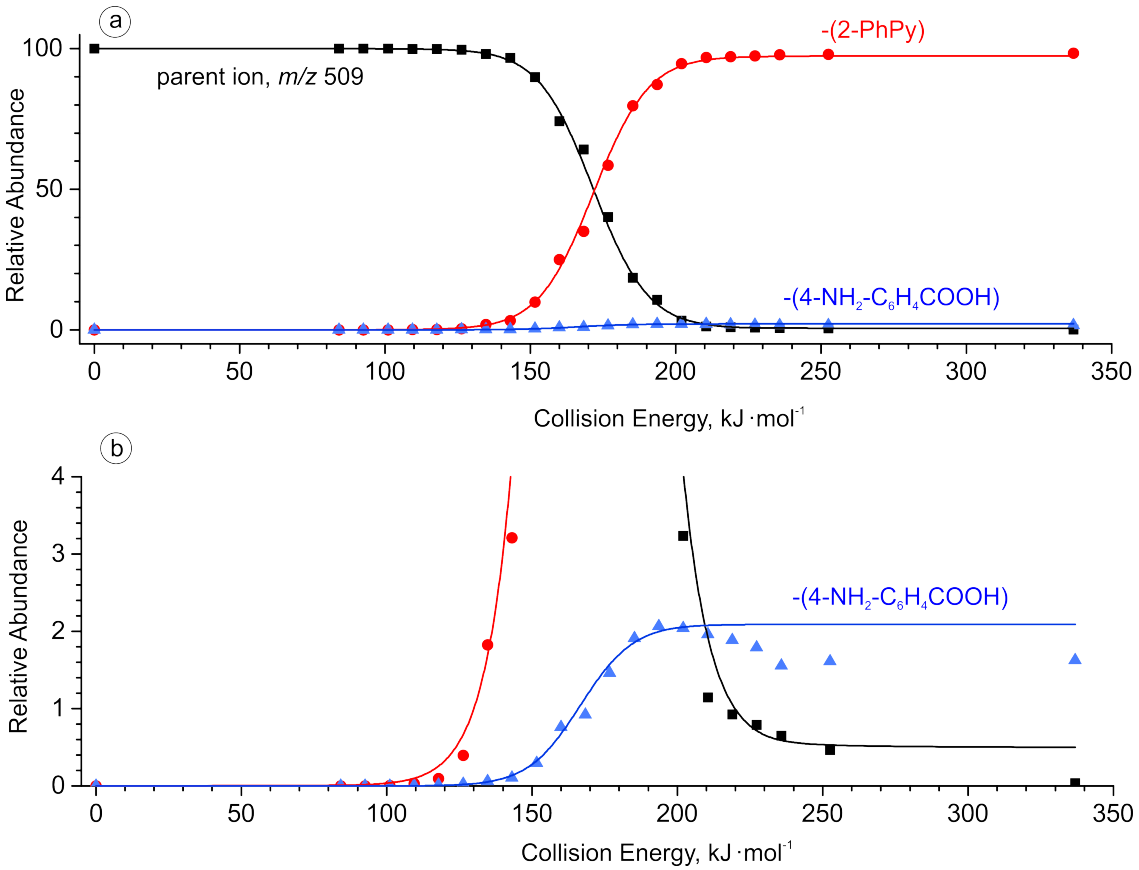

Figure 6.33: The breakdown curve for the mass selected peak at m/z 509 (4-aminobenzoic acid derivative); a) full scale; b) enlarged.

List of abbreviations and acronyms

AC	alternating current
AE	activation energy
Ad_E	electrophilic addition
ACN	acetonitrile
AcOH	acetic acid
BDE	bond dissociation energy
CID	collisional induced dissociation
CLIO	Centre Laser Infrarouge Orsay (France)
CRM	charge residue model
Cy	cyclohexyl
DFT	density functional theory
DMF	dimethylformamide
dppe	1,2-bis(diphenylphosphino)ethane
EPR	electron paramagnetic resonance
ESI-MS	electrospray ionization mass spectrometry
FEL	free electron laser
FWHM	full width at half-maximum
GC	gas-chromatography
HPLC	high-performance liquid chromatography
IEM	ion evaporation model
IM	ion mobility
IMS	ion mobility mass spectrometry
IR	infrared
IRMPD	infrared multiphoton dissociation

IT-MS	ion trap mass spectrometer
MeOH	methanol
MS	mass spectrometry
NCE	normalized collision energy
NMR	nuclear magnetic resonance
PEEK	polyether ether ketone
PES	potential energy surface
PhPy	phenylpyridine
QIT	quadrupole ion trap
RF	radio frequency
ROMP	ring-opening metathesis polymerization
RRKM	Rice-Ramsperger-Kassel-Marcus (theory)
S_N2	nucleophilic substitution (bi-molecular)
TMEDA	tetramethylethylenediamine
TS	transition state
ZPVE	zero-point vibrational energy

List of Figures

List of Schemes

List of Tables

Bibliography

[1] X.-F. Wu, P. Anbarasan, H. Neumann, M. Beller; *Ang. Chem. Int. Ed.* 49, 9047–9050 (2010).

[2] E.-i. Negishi; *Ang. Chem. Int. Ed.* 50, 6738–6764 (2011).

[3] A. Suzuki, Y. Yamamoto; *Chem. Lett.* 40, 894–901 (2011).

[4] A. Suzuki; *Ang. Chem. Int. Ed.* 50, 6722–6737 (2011).

[5] F. D. Armin de Meijere (editor) *Metal-Catalyzed Cross-Coupling Reactions, Second Edition*; WILEY-VCH Verlag GmbH & Co. KGaA, Weinheim (2004).

[6] D. H. Ringger, P. Chen; *Ang. Chem. Int. Ed.* 52, 4686–4689 (2013).

[7] M. Yamashita, J. B. Fenn; *J. Phys. Chem.* 88, 4451–4459 (1984).

[8] J. B. Fenn, M. Mann, C. K. Meng, S. F. Wong, C. M. Whitehouse; *Science* 246, 64–71 (1989).

[9] J. B. Fenn; *Ang. Chem. Int. Ed.* 42, 3871–3894 (2003).

[10] M. N. Eberlin; *Eur. J. Mass Spectrom.* 13, 19–28 (2007).

[11] L. S. Santos; *Eur. J. Org. Chem.* 235–253 (2008).

[12] L. Santos (editor) *Reactive Intermediates*; Wiley-VCH Verlag GmbH & Co. KGaA (2010).

[13] J. M. Riveros, M. Sena, G. H. Guedes, L. A. Xavier, R. Slepetys; *Pure and Applied Chemistry* 70, 1969–1976 (1998).

[14] C. Aubry, J. L. Holmes; *Int. J. Mass Spectrom.* 200, 277–284 (2000).

[15] K. L. Vikse, M. P. Woods, J. S. McIndoe; *Organometallics* 29, 6615–6618 (2010).

[16] K. L. Vikse, Z. Ahmadi, J. Luo, N. van der Wal, K. Daze, N. Taylor, J. S. McIndoe; *Int. J. Mass Spectrom.* 323, 8–13 (2012).

[17] A. T. Lubben, J. S. McIndoe, A. S. Weller; *Organometallics* 27, 3303–3306 (2008).

[18] D. Agrawal, D. Schroeder, C. M. Frech; *Organometallics* 30, 3579–3587 (2011).

[19] H. Wang, J. Liu, R. G. Cooks, Z. Ouyang; *Ang. Chem. Int. Ed.* 49, 877–880 (2010).

[20] X. Yan, R. Augusti, X. Li, R. G. Cooks; *ChemPlusChem* 78, 1142–1148 (2013).

[21] L. P. E. Yunker, R. L. Stoddard, J. S. McIndoe; *J. Mass Spectrom.* 49, 1–8 (2014).

[22] J. Halpern; *Science* 217, 401–407 (1982).

[23] C. Adlhart, P. Chen; *Helv. Chim. Acta* 83, 2192–2196 (2000).

[24] K. L. Busch, S. E. Unger, A. Vincze, R. G. Cooks, T. Keough; *J. Am. Chem. Soc.* 104, 1507–1511 (1982).

[25] R. L. Smith, H. I. Kenttaemaa; *J. Am. Chem. Soc.* 117, 1393–1396 (1995).

[26] K. K. Thoen, R. L. Smith, J. J. Nousiainen, E. D. Nelson, H. I. Kenttamaa; *J. Am. Chem. Soc.* 118, 8669–8676 (1996).

[27] Y. E. Corilo, F. M. Nachtigall, P. V. Abdelnur, G. Ebeling, J. Dupont, M. N. Eberlin; *Rsc Advances* 1, 73–78 (2011).

[28] F. F. D. Oliveira, M. R. dos Santos, P. M. Lalli, E. M. Schmidt, P. Bakuzis, A. A. M. Lapis, A. L. Monteiro, M. N. Eberlin, B. A. D. Neto; *J. Org. Chem.* 76, 10140–10147 (2011).

[29] J. Luo, A. G. Oliver, J. Scott McIndoe; *Dalton Trans.* 42, 11312–11318 (2013).

[30] V. G. Santos, M. N. Godoi, T. Regiani, F. H. S. Gama, M. B. Coelho, R. O. M. A. de Souza, M. N. Eberlin, S. J. Garden; *Chem. Eur. J.* 20, 12808–12816 (2014).

[31] M. R. dos Santos, R. Coriolano, M. N. Godoi, A. L. Monteiro, H. C. B. de Oliveira, M. N. Eberlin, B. A. D. Neto; *New J. Chem.* 38, 2958–2963 (2014).

[32] G. A. Medeiros, W. A. da Silva, G. A. Bataglion, D. A. C. Ferreira, H. C. B. de Oliveira, M. N. Eberlin, B. A. D. Neto; *Chem. Commun.* 50, 338–340 (2014).

[33] J. A. Willms, R. Beel, M. L. Schmidt, C. Mundt, M. Engeser; *Beilstein J. Org. Chem.* 10, 2027–2037 (2014).

[34] T. S. Rodrigues, V. H. C. Silva, P. M. Lalli, H. C. B. de Oliveira, W. A. da Silva, F. Coelho, M. N. Eberlin, B. A. D. Neto; *J. Org. Chem.* 79, 5239–5248 (2014).

[35] O. Bortolini, C. Chiappe, M. Fogagnolo, P. P. Giovannini, A. Massi, C. S. Pomelli, D. Ragno; *Chem. Commun.* 50, 2008–2011 (2014).

[36] J. Luo, R. Theron, L. J. Sewell, T. N. Hooper, A. S. Weller, A. G. Oliver, J. S. McIndoe; *Organometallics* 34, 3021–3028 (2015).

[37] J. Limberger, B. C. Leal, A. L. Monteiro, J. Dupont; *Chem. Sci.* 6, 77–94 (2015).

[38] H. Zeng, K. Wang, Y. Tian, Y. Niu, L. Greene, Z. Hu, J. K. Lee; *Int. J. Mass Spectrom.* 378, 169–174 (2015).

[39] M. A. Schade, J. E. Feckenstem, P. Knochel, K. Koszinowski; *J. Org. Chem.* 75, 6848–6857 (2010).

[40] K. L. Vikse, M. A. Henderson, A. G. Oliver, J. S. McIndoe; *Chem. Commun.* 46, 7412–7414 (2010).

[41] H.-Y. Wang, W.-L. Yim, T. Kluner, J. O. Metzger; *Chem. Eur. J.* 15, 10948–10959 (2009).

[42] A. Putau, K. Koszinowski; *Organometallics* 29, 3593–3601 (2010).

[43] S. Gronert; *Chem. Rev.* 101, 329–360 (2001).

[44] S. Gronert; *Mass Spectrom. Rev.* 24, 100–120 (2005).

[45] L. Fiebig, J. Kuttner, G. Hilt, M. C. Schwarzer, G. Frenking, H.-G. Schmalz, M. Schaefer; *J. Org. Chem.* 78, 10485–10493 (2013).

[46] O. Dopfer; *J. Phys. Org. Chem.* 19, 540–551 (2006).

[47] K. R. Asmis, J. Sauer; *Mass Spectrom. Rev.* 26, 542–562 (2007).

[48] L. MacAleese, P. Maitre; *Mass Spectrom. Rev.* 26, 583–605 (2007).

[49] N. C. Polfer, J. Oomens; *Phys. Chem. Chem. Phys.* 9, 3804–3817 (2007).

[50] N. C. Polfer; *Chem. Soc. Rev.* 40, 2211–2221 (2011).

[51] J. Roithova; *Chem. Soc. Rev.* 41, 547–559 (2012).

[52] J. Roithova, D. Schroder; *Chem. Eur. J.* 14, 2180–2188 (2008).

[53] J. Roithova, P. Milko; *J. Am. Chem. Soc.* 132, 281–288 (2010).

[54] N. R. Novotny, E. N. Capley, A. C. Stenson; *J. Mass Spectrom.* 49, 316–326 (2014).

[55] J. Roithova, S. Jankova, L. Jasikova, J. Vana, S. Hybelbauerova; *Ang. Chem. Int. Ed.* 51, 8378–8382 (2012).

[56] D. Agrawal, D. Schroeder; *Organometallics* 30, 32–35 (2011).

[57] F. Coelho, M. N. Eberlin; *Ang. Chem. Int. Ed.* 50, 5261–5263 (2011).

[58] G. Gerdes, P. Chen; *Organometallics* 22, 2217–2225 (2003).

[59] J. A. Labinger, J. E. Bercaw, M. Tilset; *Organometallics* 25, 805–808 (2006).

[60] G. Gerdes, P. Chen; *Organometallics* 25, 809–811 (2006).

[61] D. Schroder; *Acc. Chem. Res.* 45, 1521–1532 (2012).

[62] D. Schroder; *Phys. Chem. Chem. Phys.* 14, 6382–6390 (2012).

[63] H. Wang, G. R. Agnes; *Anal. Chem.* 71, 4166–4172 (1999).

[64] P. Kebarle, U. H. Verkerk; *Mass Spectrom. Rev.* 28, 898–917 (2009).

[65] J. Sunner, G. Nicol, P. Kebarle; *Anal. Chem.* 60, 1300–1307 (1988).

[66] J. F. d. l. Mora, G. J. Van Berkel, C. G. Enke, R. B. Cole, M. Martinez-Sanchez, J. B. Fenn; *J. Mass Spectrom.* 35, 939–952 (2000).

[67] D. Schroder, H. Schwarz; *Can. J. Chem.* 83, 1936–1940 (2005).

[68] C. Trage, M. Diefenbach, D. Schroder, H. Schwarz; *Chem. Eur. J.* 12, 2454–2464 (2006).

[69] D. Schroder, H. Schwarz, S. Schenk, E. Anders; *Ang. Chem. Int. Ed.* 42, 5087–5090 (2003).

[70] N. Ottosson, L. Cwiklik, J. Soderstrom, O. Borneholm, G. Ohrwall, P. Jungwirth; *J. Phys. Chem. Lett.* 2, 972–976 (2011).

[71] M. Girod, E. Moyano, D. I. Campbell, R. G. Cooks; *Chem. Sci.* 2, 501–510 (2011).

[72] Z. Tian, S. R. Kass; *J. Am. Chem. Soc.* 130, 10842–10843 (2008).

[73] J. D. Steill, J. Oomens; *J. Am. Chem. Soc.* 131, 13570–13571 (2009).

[74] J. Schmidt, M. M. Meyer, I. Spector, S. R. Kass; *J. Phys. Chem. A* 115, 7625–7632 (2011).

[75] D. Schroder, B. Milos, J. Roithova; *J. Am. Chem. Soc.* 134, 15897–15905 (2012).

[76] T. B. McMahon, P. Kebarle; *J. Am. Chem. Soc.* 99, 2222–2230 (1977).

[77] R. E. March; *J. Mass Spectrom.* 32, 351–369 (1997).

[78] C. Cramer; *Essentials of Computational Chemistry: Theories and Models*; Wiley, New York (2004).

[79] R. March (editor) *Quadrupole ion trap mass spectrometry*; Wiley & Sons, Inc., Hoboken, New Jersey (2005).

[80] V. S. Edmond de Hoffmann (editor) *Mass Spectrometry: Principles and Applications*; John Wiley & Sons (2009).

[81] S. T. Charles L. Wilkins (editor) *Ion Mobility Spectrometry - Mass Spectrometry: Theory and Applications*; CRC Press (2010).

[82] J. Gross (editor) *Mass spectrometry: a textbook*; Heidelberg, Germany: Springer (2011).

[83] R. B. Cole (editor) *Electrospray and MALDI Mass Spectrometry: Fundamentals, Instrumentation, Practicalities, and Biological Applications, Second Edition*; Wiley (2012).

[84] S. Banerjee, S. Mazumdar; *Int. J. Anal. Chem.* 282574 (2012).

[85] J. V. Iribarne, B. A. Thomson; *J. Chem. Phys.* 64, 2287–2294 (1976).

[86] S. Nguyen, J. B. Fenn; *P. Nat. Acad. Sci. USA* 104, 1111–1117 (2007).

[87] M. Gamero-Castano, J. F. de la Mora; *J. Chem. Phys.* 113, 815–832 (2000).

[88] J. F. de la Mora; *Anal. Chim. Acta* 406, 93–104 (2000).

[89] D. Schroder, T. Weiske, H. Schwarz; *Int. J. Mass Spectrom.* 219, 729–738 (2002).

[90] F. A. Lindemann, S. Arrhenius, I. Langmuir, N. R. Dhar, J. Perrin, W. C. McC. Lewis; *Trans. Faraday Soc.* 17, 598–606 (1922).

[91] F. Di Giacomo; *J. Chem. Educ.* 92, 476–481 (2015).

[92] M. T. Rodgers, P. B. Armentrout; *Mass Spectrom. Rev.* 19, 215–247 (2000).

[93] C. Hinderling, D. Feichtinger, D. A. Plattner, P. Chen; *J. Am. Chem. Soc.* 119, 10793–10804 (1997).

[94] X. Zhang, S. Narancic, P. Chen; *Organometallics* 24, 3040–3042 (2005).

[95] L. A. Hammad, G. Gerdes, P. Chen; *Organometallics* 24, 1907–1913 (2005).

[96] E. Zocher, R. Dietiker, P. Chen; *J. Am. Chem. Soc.* 129, 2476–2481 (2007).

[97] M.-E. Moret, P. Chen; *Organometallics* 26, 1523–1530 (2007).

[98] M. T. Rodgers, K. M. Ervin, P. B. Armentrout; *J. Chem. Phys.* 106, 4499–4508 (1997).

[99] S. Narancic, A. Bach, P. Chen; *J. Phys. Chem. A* 111, 7006–7013 (2007).

[100] P. Armentrout; *J. Am. Soc. Mass Spec.* 13, 419–434 (2002).

[101] E.-L. Zins, C. Pepe, D. Schroder; *J. Mass Spectrom.* 45, 1253–1260 (2010).

[102] P. Armentrout; *Int. J. Mass Spectrom.* 200, 219–241 (2000).

[103] K. M. Ervin; *Chem. Rev.* 101, 391–444 (2001).

[104] J. H. Futrell; *Gaseous ion chemistry and mass spectrometry*; John Wiley & Sons (1986).

[105] P. Armentrout; C. Schalley (editor) *Topics in Current Chemistry*; volume 225; 233–262–; Springer Berlin Heidelberg (2003).

[106] A. G. Brenton, R. P. Morgan, J. H. Beynon; *Annu. Rev. Phys. Chem.* 30, 51–78 (1979).

[107] N. Nibbering (editor) *The encyclopedia of mass spectrometry, vol. 4: fundamentals of and applications to organic (and organometallic) compounds*; Elsevier, Oxford (2005).

[108] G. J. Vanberkel, G. L. Glish, S. A. McLuckey; *Anal. Chem.* 62, 1284–1295 (1990).

[109] W. Paul; *Ang. Chem. Int. Ed.* 29, 739–748 (1990).

[110] N. B. Cech, C. G. Enke; *Mass Spectrom. Rev.* 20, 362–387 (2001).

[111] W. Paul; *Rev. Mod. Phys.* 62, 531–540 (1990).

[112] R. A. J. O'Hair; *Chem. Commun.* 1469–1481 (2006).

[113] G. Wu, R. G. Cooks, Z. Ouyang, M. Yu, W. J. Chappell, W. R. Plass; *J. Am. Soc. Mass Spectrom.* 17, 1216–1228 (2006).

[114] W. Xu, W. J. Chappell, Z. Ouyang; *Int. J. Mass Spectrom.* 308, 49–55 (2011).

[115] http://www.thermoscientific.de/content/dam/tfs/ATG/CMD/CMDNormalized-Collision-Energy-Technology-EN.pdf (Accessed: 29 September 2015) .

[116] E.-L. Zins, D. Rondeau, P. Karoyan, C. Fosse, S. Rochut, C. Pepe; *J. Mass Spectrom.* 44, 1668–1675 (2009).

[117] E.-L. Zins, C. Pepe, D. Rondeau, S. Rochut, N. Galland, J.-C. Tabet; *J. Mass Spectrom.* 44, 12–17 (2009).

[118] F. Derwa, E. Depauw, P. Natalis; *J. Am. Soc. Mass Spec.* 26, 117–118 (1991).

[119] C. Collette, E. De Pauw; *Rapid Commun. Mass Spectrom.* 12, 165–170.

[120] G. H. Luo, I. Marginean, A. Vertes; *Anal. Chem.* 74, 6185–6190 (2002).

[121] J. F. Greisch, V. Gabelica, F. Remacle, E. De Pauw; *Rapid Commun. Mass Spectrom.* 17, 1847–1854 (2003).

[122] G. Bouchoux, J. Y. Salpin, D. Leblanc; *Int. J. Mass Spectrom.* 153, 37–48 (1996).

[123] E. W. Mcdaniel, W. S. Barnes, D. W. Martin; *Rev. Sci. Instrum.* 33, 2–7 (1962).

[124] D. E. Clemmer, R. R. Hudgins, M. F. Jarrold; *J. Am. Chem. Soc.* 117, 10141–10142 (1995).

[125] A. B. Kanu, P. Dwivedi, M. Tam, L. Matz, J. Hill, Herbert H.; *J. Mass Spectrom.* 43, 1–22 (2008).

[126] F. Lanucara, S. W. Holman, C. J. Gray, C. E. Eyers; *Nature Chem.* 6, 281–294 (2014).

[127] C. Lapthorn, F. Pullen, B. Z. Chowdhry; *Mass Spectrom. Rev.* 32, 43–71 (2013).

[128] S. D. Pringle, K. Giles, J. L. Wildgoose, J. P. Williams, S. E. Slade, K. Thalassinos, R. H. Bateman, M. T. Bowers, J. H. Scrivens; *Int. J. Mass Spectrom.* 261, 1–12 (2007).

[129] A. Revesz, D. Schroder, T. A. Rokob, M. Havlik, B. Dolensky; *Phys. Chem. Chem. Phys.* 14, 6987–6995 (2012).

[130] https://depts.washington.edu/bushlab/instruments/(Accessed: 29 September 2015) .

[131] D. Schroder, H. Schwarz, P. Milko, J. Roithova; *J. Phys. Chem. A* 110, 8346–8353 (2006).

[132] A. Simon, C. Joblin, N. Polfer, J. Oomens; *J. Phys. Chem. A* 112, 8551–8560 (2008).

[133] J. Hyvl, D. Agrawal, R. Pohl, M. Suri, F. Glorius, D. Schroder; *Organometallics* 32, 807–816 (2013).

[134] J. M. Villalobos, J. Srogl, L. S. Liebeskind; *J. Am. Chem. Soc.* 129, 15734–15735 (2007).

[135] M. J. Frisch, G. W. Trucks, H. B. Schlegel, G. E. Scuseria, M. A. Robb, J. R. Cheeseman, G. Scalmani, V. Barone, B. Mennucci, G. A. Petersson, H. Nakatsuji, M. Caricato, X. Li, H. P. Hratchian, A. F. Izmaylov, J. Bloino, G. Zheng, J. L. Sonnenberg, M. Hada, M. Ehara, K. Toyota, R. Fukuda, J. Hasegawa, M. Ishida, T. Nakajima, Y. Honda, O. Kitao, H. Nakai, T. Vreven, J. A. Montgomery, Jr., J. E. Peralta, F. Ogliaro, M. Bearpark, J. J. Heyd, E. Brothers, K. N. Kudin, V. N. Staroverov, R. Kobayashi, J. Normand, K. Raghavachari, A. Rendell, J. C. Burant, S. S. Iyengar, J. Tomasi, M. Cossi, N. Rega, J. M. Millam, M. Klene, J. E. Knox, J. B. Cross,

V. Bakken, C. Adamo, J. Jaramillo, R. Gomperts, R. E. Stratmann, O. Yazyev, A. J. Austin, R. Cammi, C. Pomelli, J. W. Ochterski, R. L. Martin, K. Morokuma, V. G. Zakrzewski, G. A. Voth, P. Salvador, J. J. Dannenberg, S. Dapprich, A. D. Daniels, . Farkas, J. B. Foresman, J. V. Ortiz, J. Cioslowski, D. J. Fox; *Gaussian-09 Revision D.01*; gaussian Inc. Wallingford CT 2009.

[136] *TURBOMOLE V6.2 2010, a development of University of Karlsruhe and Forschungszentrum Karlsruhe GmbH, 1989-2007, TURBOMOLE GmbH, since 2007; available from http://www.turbomole.com.*

[137] C. Lee, W. Yang, R. G. Parr; *Phys. Rev. B* 37, 785–789 (1988).

[138] A. D. Becke; *Phys. Rev. A* 38, 3098–3100 (1988).

[139] A. D. Becke; *J. Chem. Phys.* 98, 5648–5652 (1993).

[140] P. J. Stephens, F. J. Devlin, C. F. Chabalowski, M. J. Frisch; *J. Phys. Chem.* 98, 11623–11627 (1994).

[141] F. Weigend, R. Ahlrichs; *Phys. Chem. Chem. Phys.* 7, 3297–3305 (2005).

[142] S. Grimme, J. Antony, S. Ehrlich, H. Krieg; *J. Chem. Phys.* 132, 154104 (2010).

[143] Y. Zhao, D. Truhlar 120, 215–241 (2008).

[144] L. Noodleman; *J. Chem. Phys.* 74, 5737–5743 (1981).

[145] S. Grimme; *J. Comput. Chem.* 27, 1787–1799 (2006).

[146] P. Milko, J. Roithova, N. Tsierkezos, D. Schroeder; *J. Am. Chem. Soc.* 130, 7186–7187 (2008).

[147] T. A. Rokob, L. Rulisek, J. Srogl, A. Revesz, E. L. Zins, D. Schroeder; *Inorg. Chem.* 50, 9968–9979 (2011).

[148] L. Jasikova, E. Hanikyrova, D. Schroeder, J. Roithova; *J. Mass Spectrom.* 47, 460–465 (2012).

[149] J. N. Vanniekerk, F. R. L. Schoening; *Nature* 171, 36–37 (1953).

[150] S. Sattar, D. Eden; *J. Phys. Chem.* 86, 140–144 (1982).

[151] G. C. Didonato, B. K. L.; *Int. J. Mass Spectrom.* 69, 67–83 (1986).

[152] A. Tsybizova, J. Tarabek, M. Buchta, P. Holy, D. Schroeder; *Rapid Commun. Mass Spectrom.* 26, 2287–2294 (2012).

[153] A. Tsybizova, J. Roithova; *Mass Spectrom. Rev.* DOI: 10.1002/mas.21464 (2015).

[154] L. S. Liebeskind, J. Srogl; *Org. Lett.* 4, 979–981 (2002).

[155] Z. Zhang, L. S. Liebeskind; *Org. Lett.* 8, 4331–4333 (2006).

[156] H. Yang, H. Li, R. Wittenberg, M. Egi, W. Huang, L. S. Liebeskind; *J. Am. Chem. Soc.* 129, 1132–1140 (2007).

[157] H. Prokopcova, L. Pisani, C. O. Kappe; *Synlett* 43–46 (2007).

[158] A. Morita, S. Kuwahara; *Org. Lett.* 8, 1613–1616 (2006).

[159] S. Oumouch, M. Bourotte, M. Schmitt, J. J. Bourguignon; *Synthesis* 25–27 (2005).

[160] A. Lengar, C. O. Kappe; *Org. Lett.* 6, 771–774 (2004).

[161] F. A. Alphonse, F. Suzenet, A. Keromnes, B. Lebret, G. Guillaumet; *Org. Lett.* 5, 803–805 (2003).

[162] A. Varela-Alvarez, L. S. Liebeskind, D. G. Musaev; *Organometallics* 31, 7958–7968 (2012).

[163] L. Wang, C. Dai, S. K. Burroughs, S. L. Wang, B. Wang; *Chem. Eur. J.* 19, 7587–7594 (2013).

[164] A. E. King, T. C. Brunold, S. S. Stahl; *J. Am. Chem. Soc.* 131, 5044–5045 (2009).

[165] S. R. Whitfield, M. S. Sanford; *J. Am. Chem. Soc.* 129, 15142–15143 (2007).

[166] N. R. Deprez, M. S. Sanford; *J. Am. Chem. Soc.* 131, 11234–11241 (2009).

[167] X. Chen, G. Dobereiner, X.-S. Hao, R. Giri, N. Maugel, J.-Q. Yu; *Tetrahedron* 65, 3085–3089 (2009).

[168] L. Ackermann; *Chem. Rev.* 111, 1315–1345 (2011).

[169] E. Ferrer Flegeau, C. Bruneau, P. H. Dixneuf, A. Jutand; *J. Am. Chem. Soc.* 133, 10161–10170 (2011).

[170] D. Kalyani, K. B. McMurtrey, S. R. Neufeldt, M. S. Sanford; *J. Am. Chem. Soc.* 133, 18566–18569 (2011).

[171] A. John, K. M. Nicholas; *J. Org. Chem.* 76, 4158–4162 (2011).

[172] L. Ackermann, S. I. Kozhushkov, D. S. Yufit; *Chem. Eur. J.* 18, 12068–12077 (2012).

[173] B. Butschke, H. Schwarz; *Chem. Eur. J.* 18, 14055–14062 (2012).

[174] I. Fabre, N. von Wolff, G. Le Duc, E. F. Flegeau, C. Bruneau, P. H. Dixneuf, A. Jutand; *Chem. Eur. J.* 19, 7595–7604 (2013).

[175] A. R. Dick, M. S. Sanford; *Tetrahedron* 62, 2439–2463 (2006).

[176] J. Dupont, C. S. Consorti, J. Spencer; *Chem. Rev.* 105, 2527–2572 (2005).

[177] A. D. Ryabov; *Chem. Rev.* 90, 403–424 (1990).

[178] I. Omae; *Cyclometalation Reactions: Five-Membered Ring Products as Universal Reagents*; Springer Japan (2014).

[179] D. Schroder, M. Engeser, M. Bronstrup, C. Daniel, J. Spandl, H. Hartl; *Int. J. Mass Spectrom.* 228, 743–757 (2003).

[180] A. Tsybizova, L. Rulsek, D. Schroder, T. A. Rokob; *J. Phys. Chem. A* 117, 1171–1180 (2013).

[181] M. Besora, J.-L. Carreon-Macedo, A. Cimas, J. N. Harvey; *Adv. Inorg. Chem., Vol 61: Metal Ion Controlled Reactivity* 61, 573–623 (2009).

[182] D. H. Ess, S. M. Bischof, J. Oxgaard, R. A. Periana, W. A. Goddard; *Organometallics* 27, 6440–6445 (2008).

[183] D. Lapointe, K. Fagnou; *Chem. Lett.* 39, 1118–1126 (2010).

[184] R. Jazzar, J. Hitce, A. Renaudat, J. Sofack-Kreutzer, O. Baudoin; *Chem. Eur. J.* 16, 2654–2672 (2010).

[185] X. Chen, X.-S. Hao, C. E. Goodhue, J.-Q. Yu; *J. Am. Chem. Soc.* 128, 6790–6791 (2006).

[186] D. H. Gibson, Y. Ding, R. L. Miller, B. A. Sleadd, M. S. Mashuta, J. F. Richardson; *Polyhedron* 18, 1189–1200 (1999).

[187] F. Pozgan, P. H. Dixneuf; *Adv. Synth. Catal.* 351, 1737–1743 (2009).

[188] A. Skriba, J. Schulz, J. Roithova; *Organometallics* 33, 6868–6878 (2014).

[189] A. Gray, A. Tsybizova, J. Roithova; *Chem. Sci.* 6, 5544–5553 (2015).

[190] C. J. Shaffer, A. Revesz, D. Schroder, L. Severa, F. Teply, E.-L. Zins, L. Jasikova, J. Roithova; *Ang. Chem. Int. Ed.* 51, 10050–10053 (2012).

[191] S. Ehrlich, J. Moellmann, W. Reckien, T. Bredow, S. Grimme; *ChemPhysChem* 12, 3414–3420 (2011).

[192] S. Grimme, W. Hujo, B. Kirchner; *Phys. Chem. Chem. Phys.* 14, 4875–4883 (2012).

[193] A. G. Harrison; *J. Mass Spectrom.* 34, 577–589.

[194] H. Lioe, R. A. J. O'Hair; *Org. Biomol. Chem.* 3, 3618–3628 (2005).